Dynamics of a dipolar Bose-Einstein condensate interacting with a superconducting surface

Dissertation
zur Erlangung des akademischen Grades eines
Dr. rer. nat.
an der Fakultät für Physik
der Universität Bielefeld

vorgelegt von

Igor Sapina

im

Januar 2015

Erstgutachter: Prof. Dr. Thomas Dahm
Zweitgutachter: Prof. Dr. Jürgen Schnack

Für meine Eltern

Abstract

The subject of the present thesis is the study of the interaction between a Bose-Einstein condensate (BEC) and a superconductor. The BEC performs center-of-mass oscillations perpendicular to the superconducting surface. Each atom in the BEC carries a magnetic dipole moment, which induces eddy currents in the surface. These eddy currents are a source of a magnetic field which modifies the potential in which the BEC is trapped. This leads to a change of the dynamical behavior of the BEC. In particular the BEC center-of-mass oscillation frequency is shifted compared to the case without the surface interaction. Additionally, the potential generated by the superconductor excites shape oscillations of the BEC.

To investigate these effects, the Gross-Pitaevskii equation for a dipolar BEC close to a superconducting surface is solved numerically. Also analytical approximations are presented and compared to the numerically obtained results. It is shown that the interaction with the superconducting surface generates a frequency shift, that is large enough to be detected in an experiment. Furthermore, different methods to identify the eddy current effect are presented.

It is also discussed how the effects on the BEC can be enhanced by choosing the proper dipole orientation and by adjusting the geometry of the setup. The BEC shape oscillations can be additionally enhanced by making use of a resonance phenomenon.

Contents

Introduction

In 1924 Satyendra Bose presented his theoretical work on the statistics of photons [1]. In the same year Albert Einstein expanded this theory to massive, non-interacting particles [2] and thus predicted the phenomenon which is today called Bose-Einstein condensation (BEC). It describes the macroscopic occupation of the ground state which occurs in a system of Bose particles below a certain critical temperature T_c. From the theoretical prediction to the first experimental realization of a BEC consisting of atoms passed over seventy years. In 1995 Wolfgang Ketterle [3] as well as Carl Wieman and Eric Cornell [4] were successful in the creation of a BEC consisting of alkali atoms. For this accomplishment they received the Noble Prize in 2001. Such a BEC is formed by a dilute gas ($\sim 10^{13} - 10^{14}\,\mathrm{cm}^{-3}$) of Bose atoms. These atoms are trapped in a potential which is created by magnetic or optical fields. The gas is cooled below the transition temperature T_c at which condensation occurs. Due to the low density of the atoms and their high mass, the critical temperature T_c is rather low. It ranges from a few ten nK to a few µK. A BEC consists typically of 10^4 to some few 10^5 atoms. In the case of alkali atoms, like for example ^{87}Rb, the interaction between the atoms at such low temperatures is described using an isotropic contact interaction. The strength of this interaction is expressed in a single parameter, the so-called s-wave scattering length. For ^{87}Rb atoms the scattering length is $a_s = 5.7\,\mathrm{nm}$. While this is larger than the actual size of a single atom, it is a lot smaller than the mean distance between two atoms in such dilute gases. In this sense one speaks of a weakly interacting gas. Depending on the number of atoms in the trap, many properties of the gas are not too far off from the ideal case of a non-interacting gas. A weakly interacting, dilute gas of bosons at a temperature far below T_c is very accurately described using a mean field approach. This leads to the so-called Gross-Pitaevskii equation (GPE). It is a non-linear Schrödinger equation and describes the static and dynamical properties of the BEC wave function. The solution of this equation, in particular the numerical solution, is one of the main tasks of the present thesis.

Alkali atoms are not the only atoms that are used to create dilute gases of bosons. Atoms with large magnetic dipole moment present another interesting option to create a BEC. The first BEC of this kind was realized with ^{52}Cr atoms [5]. While rubidium atoms carry a magnetic dipole moment of $1\mu_B$, chromium atoms have a magnetic dipole moment of $6\mu_B$. For alkali atoms the magnetic dipole-dipole interaction plays only a very minor role and can be neglected. For chromium this is not the case, the dipole-dipole interaction has a significant effect on the BEC. Such a BEC is usually referred to as a dipolar BEC [6]. Besides chromium, dipolar BECs have so far been created with erbium atoms [7] and also with dysprosium atoms [8]. Both have an even larger magnetic dipole moment than chromium. In order to study the magnetic interaction with a superconductor, a large magnetic dipole moment is of course advantageous. For the theoretical description the dipole-dipole interaction has to be incorporated into the GPE.

Another important experimental accomplishment was the creation of micro fabricated atom traps. For the present thesis, magnetic microtraps [9] are of particular interest. The electronic structures necessary to generate the magnetic field which traps the atoms is accommodated on a single chip. The scaling down of the whole apparatus means that also the minimum of the potential moves closer to the surface. If one is interested in the interaction between a BEC and the surface, it is of course beneficial to bring the BEC very close to the surface. However, there is also a downside in bringing the BEC very close to the surface. The lifetime of a BEC is drastically reduced if it is brought close to the surface of the conductor. Responsible for the reduced lifetime is the so-called Johnson noise [10, 11]. A solution to this problem presents itself in the use of superconducting microtraps.

The discovery of superconductivity goes back to the year 1911, when H. Kamerlingh Onnes realized that below a certain temperature the electrical resistance of some materials vanishes entirely [12]. In the subsequent years more properties of superconducting materials were discovered. Besides the fact that a superconductor is a perfect conductor, it turns out that it is also a perfect diamagnet. It means that a magnetic field is completely expelled from a superconductor, whether the magnetic field is applied while the material is in the superconducting state or in the normal state. Once it is in the superconducting state, the magnetic field gets expelled. This is called the Meissner-Ochsenfeld effect [13]. A number of theories have been developed which explain the occurrence of superconductivity. The most prominent theory is the Bardeen-Cooper-Schrieffer (BCS) theory [14]. It explains superconductivity on a microscopic level. The electrons in a

superconductor feel an attractive interaction which causes them to form so-called Cooper pairs. The two electrons that constitute a Cooper pair have opposite momentum and spin. Just like the alkali atoms in a dilute gas BEC can be described with a single macroscopic wave function, the Cooper pairs can also be described using a macroscopic wave function. Both are macroscopic quantum phenomena, which makes it interesting to investigate the interaction between those two systems. The critical temperature at which superconductivity occurs in elementary superconductors is typically of the order of a few Kelvin. For example, aluminum has a T_c of 1.2 K. The elementary superconductor with the highest T_c is niobium with $T_c = 9.2\,\mathrm{K}$ [15]. Some materials have been discovered which have a critical temperature of up to 135 K and under high pressure even more [16–24]. The reason why these materials have such a high T_c is still under investigation.

In recent years, superconductors have been successfully used to build magnetic microtraps [25–30]. An interesting aspect here is the possibility to create a BEC close to a superconducting surface. This makes it possible to investigate the interaction between BEC and superconductor.

The successful coupling of a BEC and a superconductor is also an interesting endeavor in regard to quantum information processing. The core of a quantum computer is the quantum bit, commonly known as qubit. A classical bit is a system which has two distinct states. The system is either in the one state or in the other state. A qubit is a quantum system which also has two states, but in contrast to the classical system, the quantum system can exist in superposition of those two states. So far a variety of different sorts of qubits have been realized, some are based on solid state devices [31,32], others are atomic systems [33] or trapped ions [34,35]. Every system has its advantages and disadvantages. Good control of the system is important in order to prepare and to measure the state of the system. This requires a controlled coupling of the qubit to the environment. This is a strength of devices based on solids. On the other hand, once the state is prepared, it is desirable that the coherence of the state is preserved for a long time. For this, the system should be very well isolated from the environment. This is the case in atomic systems like for example BECs. Hybrid quantum systems, consisting of atomic systems coupled to solid state devices, are able to combine the strengths of both [36–45]. The idea is, that once a certain state has been prepared, it is transferred to the other system with the longer coherence time where it can be stored. Later it is transferred back in order to be read out.

Such a hybrid system could for example consist of a BEC coupled to a superconductor [46–51]. For a controlled coupling it is necessary to under-

stand the interaction between the BEC and the superconductor.

The setup discussed in the present work consists of a dipolar BEC and a superconducting surface. The BEC is placed close to the surface and is excited in such a way that it starts to oscillate perpendicular to the surface. The magnetic dipole moments of the atoms induce eddy currents in the superconducting surface. Since this is a superconductor and not a normal conductor, the induced currents are not damped. This means the oscillation energy of the BEC is not transformed into thermal energy, thus the motion of the BEC is not damped. However, the eddy currents do have an effect on the oscillation of the BEC. The eddy currents generate a magnetic field which alters the curvature of the trapping potential. This has an effect on the oscillation frequency of the BEC. A central question is: Does the eddy current effect generate a frequency shift that is large enough to be detected in an experiment? If that is the case, then still the question remains: How can the eddy current effect be identified and distinguished from other effects that may have an impact on the oscillation frequency? Close to the surface there can be a number of other effects which have an impact on the BEC motion. A prominent example is the Casimir-Polder force. The effect of the Casimir-Polder force on the oscillation frequency of a BEC has been studied theoretically [52] and it has also been measured in an experiment [53]. They were able to measure the frequency with a precision of 10^{-5}. For the following discussion in this work, this value represents the threshold for what is considered detectable and what in considered undetectable. In Refs. [54, 55] it was shown that a frequency shift of this order is possible. However, if one is restricted to ^{87}Rb BECs, 10^{-5} is more or less the frequency shift that can be reached under optimal conditions. A larger shift can be expected if the ^{87}Rb BEC is replaced by a dipolar BEC. In the case of a ^{52}Cr BEC the frequency shift can be of order 10^{-3}, which is within experimental means to be detected. Furthermore, it was proposed to use the distinct dependence of the frequency shift on the number of atoms in the BEC as a fingerprint in order to distinguish the eddy current effect from other surface effects. The results presented in Refs. [54,55] were based on a rather simple model. However, the model is useful since it allows to determine analytical approximations for the frequency shift. Furthermore it reproduces the qualitative behavior and also the correct order of magnitude.

In the present work, in addition to the simple model from Refs. [54, 55], also more accurate methods are used. The effect of the superconducting surface is included directly in the GPE for dipolar BECs. The resulting equation for the BEC wave function is not analytically solvable. Thus it

needs to be solved numerically. The numerical methods needed for this task are presented and the numerically obtained results are used to study the effect on the dynamics of the BEC. Particularly the center-of-mass motion is analyzed and the results are compared to analytical approximations. The analytical model is then also used to discuss the impact of different dipole orientations on the frequency shift. Finally, shape oscillations of the BEC, caused by the interaction with the surface, are investigated.

The eddy current effect does not only influence the dynamical properties of the BEC but also the static properties. For example, the minimum of the trapping potential gets shifted and thereby also the position of the BEC is shifted. In principle, this shift might also be interesting to investigated more closely. However, the shift is on a length scale of $\sim$ nm [54], which makes the experimental detection impossible. Since frequencies can be measured more accurately, the focus of this thesis is on the dynamical properties of the BEC.

This work is structured as follows: Chapter 1 gives a basic overview of the theoretical models used throughout the rest of this work. In Chapter 2 the numerical methods used to solve the GPE are presented and a few examples of a BEC in a harmonic trap are discussed. Chapter 3 deals with the interaction potential between the BEC and the surface. Different models to calculate the potential are presented and it is shown how the interaction potential is included in the GPE. In Chapter 4 the frequency shift of the center-of-mass motion is discussed. Results for the frequency shift based on numerical results as well as analytical approximations are presented. Furthermore the impact of the dipole orientation of the atoms in the BEC on the frequency shift is investigated. The effect of the surface potential on the BEC shape fluctuations is presented in Chapter 5. Finally, a conclusion is given at the end.

Part of the present thesis has been published beforehand in Refs. [55] and [56]. The results that are presented and summarized in Appendix A have been published in Ref. [57].

Chapter 1

Basics

This chapter gives an overview over the basic theory that is used throughout this thesis. Besides the theory also some experimental aspects are discussed. The theory is discussed thoroughly enough, so that it is possible to read and understand this thesis without consulting any further literature. However, the discussion of the topics presented in this chapter is neither intended, nor is it in any way complete. For a more complete discussion, the reader is advised to consult the appropriate literature. The references to the relevant literature is given throughout the text.

1.1 Trapping neutral atoms

Trapping the atoms is a necessary prerequisite for the successful generation of a BEC. Since the atoms do not carry an electrical charge, one cannot use static electric fields to create a trapping potential. One method to trap neutral atoms is the use of time dependent electric fields, like for example the electric field of a laser. These so-called optical dipole traps [58] rely on the AC Stark effect [59], where one uses a laser which is red or blue detuned in relation to an optical transition frequency of the atom. If the laser is red detuned the atoms are drawn to regions of high field intensity and if the laser is blue detuned the atoms feel an attractive force towards regions of low intensity. This way the atoms are trapped either in a local minimum or a local maximum of the laser field. Making use of the magnetic dipole moment of the atoms, static magnetic fields can also be used to generate a trap. Depending on its internal magnetic spin state, an atom is either drawn to regions of high magnetic field strength or regions of low magnetic field strength. Those internal spin states are often referred to as high field seeker and low filed seeker, respectively. As it turns out, it is impossible to

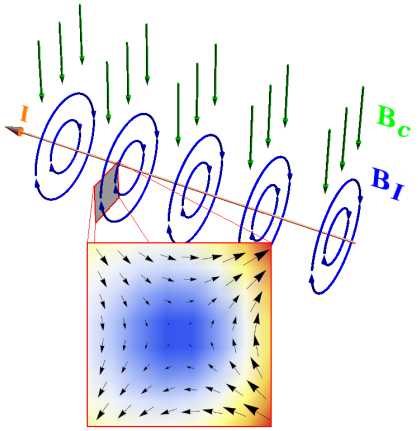

Figure 1.1: Schematic setup for a waveguide. The current I (orange) generates the magnetic field $\mathbf{B}_I$ (blue), which is superposed by the homogenous field $\mathbf{B}_c$ (green). They cancel each other on a line parallel to the wire. A cut of the magnetic field distribution in the region of the minimum is presented in the inset (red box). The black arrows indicate the magnetic field lines and the color map shows the modulus of the magnetic field. Blue indicates a weak field and red indicates a strong field.

generate a magnetic field maximum in a current free region [60, 61], thus only a local field minimum comes into consideration to form a trap. This implies that only low field seeker states can be trapped by static magnetic fields.

1.1.1 Conventional magnetic microtraps

One of the simplest setups one can think of, in order to generate a magnetic field trap, is a single long wire which generates a circular magnetic field. A schematic depiction of the setup is presented in Fig. 1.1. The current I (orange) flowing along the long wire, generates a circular magnetic field $\mathbf{B}_I$ (blue). The circular field $\mathbf{B}_I$ is superposed by a homogenous field $\mathbf{B}_c$ (green), which is oriented perpendicular to the wire. $\mathbf{B}_c$ is called the compression or the bias field. $\mathbf{B}_I$ and $\mathbf{B}_0$ cancel each other out along a line parallel to the wire. The inset of Fig. 1.1 shows a cut of the magnet field distribution in the region of the minimum. The color map represents $|\mathbf{B}|$, where blue indicates a weak magnetic field and red a strong magnetic field. A good approximation of the field modulus close to the minimum is given by $|\mathbf{B}| = a_r \cdot r$, where r is the radial coordinate measured from the minimum of the potential and $a_r = \frac{2\pi}{\mu_0}\frac{B_c^2}{I}$ [62]. In order to avoid a magnetic field zero at the minimum, as

well as a cusp, a homogenous field $\mathbf{B}_0$ (not depicted in the figure) is applied parallel to the wire. This yields a magnetic field distribution of the form $|\mathbf{B}| \approx B_0 + \frac{1}{2}\frac{a_r^2}{B_0} \cdot r^2$. With that the atoms are confined in two dimensions by a harmonic potential. A confinement in the axial direction is achieved by additional wires perpendicular to the first one. For more details on the discussed setup see Ref. [62]. A variety of different setups and geometries is presented in the review articles [9, 63, 64].

The electric circuits necessary to generate the magnetic field trap can also be miniaturized and incorporated on a chip. Such a device is often called an atom chip [65] or it is also referred to as a microtrap [9]. Atom chips are not restricted to devices that are based on static magnetic fields, but also integrated devices where the confining fields are optical or static electrical fields. One motivation for the miniaturization of magnetic microtraps is that the confinement of the atoms gets stronger, the closer one gets to the field generating current. An even more interesting possibility that is offered by integrated devices is the vast number of different and easily realizable wire geometries on the chip. This makes it possible to create interesting trapping potentials, like for example double well potentials or lattice structures.

An interesting aspect is the possibility to generate traps close to the surface of the chip. If the atoms can be positioned close enough to the surface, the interaction of the atoms with the surface can be studied. Creating a BEC in such a trap opens up the possibility to study the interaction between the BEC and the surface.

If the BEC is brought close to the surface of a conventional conductor, the lifetime of the BEC is reduced due to a significantly increased atom loss rate from the trap. The reason for the increased loss rate are fluctuations of the electrical current, the Johnson noise [10, 11, 66–68], which translates to fluctuations of the magnetic field. These fluctuations drive transitions between the spin states of the atom, so that an atom in a low field seeker state can flip into a high field seeker state. If that happens, the atom gets expelled from the trap. If the intensity of the field fluctuations at the corresponding frequency is high enough, this mechanism leads to an atom loss rate that drastically reduces the BEC lifetime [10, 11].

1.1.2 Superconducting magnetic microtraps

In order to avoid the losses due to the Johnson noise, the use of superconducting microtraps is advantageous compared to conventional metallic microtraps. In a superconductor the Johnson noise is drastically suppressed, which leads to significantly lower spin-flip rates. Thus the lifetime of the

BEC is considerably increased [69–72]. Despite the technical difficulties posed by the combination of ultrahigh vacuum technology with cryostat technology, in the recent years superconducting microtraps have been successfully realized [25–30].

The goal is to bring the minimum of the harmonic trap as close as possible to the superconducting surface. However, the Meissner effect poses an obstacle. The expulsion of the magnetic field from the superconductor lowers the trap depth close to the superconductor [27]. This effect limits the minimal distance between the superconductor and the trap. The consequences of the Meissner effect can be reduced by replacing the type-I superconductor by a type-II superconductor [28, 73]. In the so-called mixed state or vortex state, the magnetic field is able to penetrate the superconductor in the form of vortices [74]. However, in the region where a vortex forms, the superconductivity breaks down, which leads to an increase of the spin-flip rate.

Despite the impact of the Meissner effect, it was shown that the formation of a trap close to the surface is still possible [49, 72, 75, 76]. So far a trap distance of 14 μm has been realized in an experiment [49]. Theoretical calculations of the magnetic field distribution of a rectangular superconducting strip have shown that it is even possible to create a trap in a distance below 1 μm [75]. However, such a close approach is only possible at the corners of the superconductor.

The close approach to the superconductor, combined with the increased lifetime of the BEC, makes the superconducting microtrap the ideal tool to study the interaction between a superconductor and a BEC.

1.2 Bose-Einstein condensation

The central object of this thesis is the Bose-Einstein condensate. A cloud of Bose atoms is trapped by an appropriate potential and cooled below the transition temperature T_c. The case of non-interacting particles is standard textbook knowledge and therefore not covered in detail here (see for example [59, 77, 78]). At the transition temperature T_c the occupation of the ground state becomes macroscopic, meaning that it is of the order of the total number of atoms N, while the occupation of the excited states becomes of order 1. As the temperature is further reduced, more and more atoms occupy the ground state, until at $T = 0$ all atoms are in the ground state. The macroscopic occupation of the ground state is called Bose-Einstein condensation.

1.2.1 Stationary Gross-Pitaevskii equation for a dipolar BEC

In the case that the bosons under consideration are atoms, like for example ^{87}Rb, the interaction between the atoms can not be neglected. For example, the transition temperature is modified due to the interaction between the atoms. However, in this section, and also throughout the rest of this thesis, the case $T = 0$ is discussed. This is an appropriate assumption if the temperature of the system is far below the transition temperature. Consider N interacting bosons trapped in a potential $V_{\mathrm{T}}(\mathbf{r})$. Say the interaction potential between two atoms at the positions $\mathbf{r}_i$ and $\mathbf{r}_j$ is $U(\mathbf{r}_i - \mathbf{r}_j)$. The Hamiltonian for this system is given by

$$\hat{H} = \sum_{i=1}^{N} \left[\frac{\mathbf{p}_i^2}{2m} + V_{\mathrm{T}}(\mathbf{r}_i) \right] + \frac{1}{2} \sum_{i=1}^{N} \sum_{j \neq i}^{N} U(\mathbf{r}_i - \mathbf{r}_j), \tag{1.1}$$

where $\mathbf{p}_i$ is the momentum operator of the i-th atom. All atoms in the trap are of the same kind and therefore have the same mass m. In order to find an expression for the energy of the system, it is necessary to find an appropriate many body wave function for the bosons. Within a mean field approach the so-called *Hartree ansatz* is used for the wave function, where the many body wave function Ψ_{H} is expressed as a product of all single body wave functions of the individual atoms. At zero temperature all atoms occupy the same single body state ψ. With that the Hartree ansatz reads

$$\Psi_{\mathrm{H}}(\mathbf{r}_1, \mathbf{r}_2, \ldots, \mathbf{r}_N) = \prod_{i=1}^{N} \psi(\mathbf{r}_i). \tag{1.2}$$

Evidently, the wave function is already symmetric, so that there is no need for symmetrization of the wave function. The energy of the system of interacting bosons is calculated as the expectation value of the Hamiltonian (1.1) with respect to the wave function (1.2), which yields the following energy functional

$$\begin{aligned} E[\psi] &= \left\langle \hat{\mathrm{H}} \right\rangle \\ &= \int_{\mathbb{R}^{3N}} \mathrm{d}\mathbf{r}_1 \mathrm{d}\mathbf{r}_2 \ldots \mathrm{d}\mathbf{r}_N \, \Psi_{\mathrm{H}}^*(\mathbf{r}_1, \mathbf{r}_2, \ldots, \mathbf{r}_N) \, \hat{H} \Psi_{\mathrm{H}}(\mathbf{r}_1, \mathbf{r}_2, \ldots, \mathbf{r}_N). \end{aligned}$$

After evaluating this expression, the energy functional is found to be

$$E[\psi] = N\int \mathrm{d}\mathbf{r}\left\{-\frac{\hbar^2}{2m}|\boldsymbol{\nabla}\psi(\mathbf{r})|^2 + V_{\mathrm{T}}(\mathbf{r})|\psi(\mathbf{r})|^2 + \frac{N-1}{2}\int \mathrm{d}\mathbf{r}' U(\mathbf{r}-\mathbf{r}')|\psi(\mathbf{r})|^2|\psi(\mathbf{r}')|^2\right\}. \quad (1.3)$$

In order to find the ground state of the system, the energy needs to be minimized under the constraint that the number of atoms

$$N[\psi] = \int d\mathbf{r}\ |\psi(\mathbf{r})|^2$$

remains constant. This is most conveniently accomplished by the method of Lagrange multipliers. It leads to the minimization of $E[\psi] - \mu N[\psi]$, where μ is the chemical potential. Here μ is introduced as Lagrange multiplier and makes sure that the number of atoms remains constant. The result of the minimization reads

$$\left\{-\frac{\hbar^2\boldsymbol{\nabla}^2}{2m} + V_{\mathrm{T}}(\mathbf{r}) + (N-1)\int \mathrm{d}\mathbf{r}' U(\mathbf{r}-\mathbf{r}')|\psi(\mathbf{r}')|^2\right\}\cdot\psi(\mathbf{r}) = \mu\cdot\psi(\mathbf{r}). \quad (1.4)$$

This is the so-called *Gross-Pitaevskii equation* (GPE) [59, 78]. It is a non-linear Schrödinger equation. Its eigenvalue is the chemical potential and not the energy, as it is the case for the linear Schrödinger equation. The non-linear term in the GPE appears due to the interaction between the atoms. In the non-interacting case with $U(\mathbf{r}-\mathbf{r}') = 0$, the GPE reduces to the standard linear Schrödinger equation and the chemical potential gives the energy per particle. The external potential $V_{\mathrm{T}}(\mathbf{r})$ confines the atoms and in the following it is referred to as *trapping potential* or simply as *trap*. In principle the trapping potential can be arbitrary. However, usually a harmonic potential is used. Therefore, for the remainder of this work, V_{T} is assumed to be a harmonic potential of the form

$$V_{\mathrm{T}}(\mathbf{r}) = \frac{m}{2}\left(\omega_x^2x^2 + \omega_y^2y^2 + \omega_z^2z^2\right). \quad (1.5)$$

Obviously, the mass m of the atoms is a fixed parameter. The only tuneable parameters are the trap frequencies ω_x, ω_y, and ω_z.

The interaction potential $U(\mathbf{r}-\mathbf{r}')$ can have different kinds of contributions. The dominant interaction at low temperatures is the *s-wave scattering* [59, 78]. This interaction is modeled with the potential

$$U_s(\mathbf{r}-\mathbf{r}') = g_s\delta(\mathbf{r}-\mathbf{r}'). \quad (1.6)$$

The parameter

$$g_s = \frac{4\pi\hbar^2}{m} a_s \tag{1.7}$$

gives the strength of this contact interaction, with a_s being the scattering length. In the case of ^{87}Rb the scattering length has been experimentally determined to be $a_s = 5.7\,\mathrm{nm}$ [4]. The atom density of a BEC is typically of the order of $10^{13}\,\mathrm{cm}^{-3}$. Thus, the mean distance between two atoms is of the order of a few 100 nm. So that the distance is much larger than the scattering length. In this sense the interaction between the atoms is considered weak and is usually referred to as a weakly interacting Bose gas.

If the atoms carry a magnetic dipole moment, an additional contribution to $U(\mathbf{r}-\mathbf{r}')$ needs to be considered. The magnetic interaction potential between two dipoles is given by [79]

$$U_{\mathrm{md}}(\mathbf{r}-\mathbf{r}') = -\frac{\mu_0}{4\pi} \frac{3\,(\boldsymbol{\mu}_{\mathrm{d}}\cdot\hat{\mathbf{n}})\,(\boldsymbol{\mu}'_{\mathrm{d}}\cdot\hat{\mathbf{n}}) - \boldsymbol{\mu}_{\mathrm{d}}\cdot\boldsymbol{\mu}'_{\mathrm{d}}}{|\mathbf{r}-\mathbf{r}'|^3}, \tag{1.8}$$

where $\hat{\mathbf{n}} = (\mathbf{r}-\mathbf{r}')/|\mathbf{r}-\mathbf{r}'|$ is the normalized distance vector between the two magnetic dipole moments $\boldsymbol{\mu}_{\mathrm{d}}$ and $\boldsymbol{\mu}'_{\mathrm{d}}$, and μ_0 is the vacuum permeability. Applying an homogeneous external magnetic field leads to the polarization of the BEC. In the following, the BEC is always considered to be completely polarized. In the case that the atoms are not all in the same spin state, the Hartree ansatz (1.2) is no longer applicable. It needs to be expanded in order to describe the other involved spin states as well. This results in a system of coupled GPEs rather than a single equation. Unless explicitly stated otherwise, the direction in which the dipoles are oriented is always the z-direction. Since all the atoms carry the same magnetic dipole moment μ_{d} one can write that $\boldsymbol{\mu}_{\mathrm{d}} = \boldsymbol{\mu}'_{\mathrm{d}} = \mu_{\mathrm{d}}\cdot\hat{\mathbf{e}}_z$. Thus the expression for the dipole-dipole interaction potential simplifies to

$$U_{\mathrm{md}}(\mathbf{r}-\mathbf{r}') = -\frac{g_D}{4\pi}\left(\frac{3\,(z-z')^2}{|\mathbf{r}-\mathbf{r}'|^5} - \frac{1}{|\mathbf{r}-\mathbf{r}'|^3}\right). \tag{1.9}$$

Here the parameter

$$g_D = \mu_0 \mu_{\mathrm{d}}^2, \tag{1.10}$$

is introduced. It is a measure for the strength of the dipole-dipole interaction. In contrast to the s-wave interaction, the dipole-dipole interaction is a long ranged, anisotropic interaction. Depending on the relative position of the two interacting dipoles the interaction sign may be negative or positive. An attractive interaction between the atoms can cause an instability of the

condensate. If the dipole-dipole interaction becomes too strong, the BEC may become unstable [80]. Using the mathematical identities

$$\frac{3\left(z-z'\right)^2}{\left|\mathbf{r}-\mathbf{r}'\right|^5}-\frac{1}{\left|\mathbf{r}-\mathbf{r}'\right|^3}=\frac{\partial^2}{\partial z^2}\frac{1}{\left|\mathbf{r}-\mathbf{r}'\right|}-\frac{1}{3}\boldsymbol{\nabla}_{\mathbf{r}}^2\frac{1}{\left|\mathbf{r}-\mathbf{r}'\right|},$$

and

$$-\boldsymbol{\nabla}_{\mathbf{r}}^2\frac{1}{\left|\mathbf{r}-\mathbf{r}'\right|}=4\pi\delta\left(\mathbf{r}-\mathbf{r}'\right),$$

the expression for the dipole-dipole interaction is rewritten in the following way [57]

$$U_{\mathrm{md}}\left(\mathbf{r}-\mathbf{r}'\right)=-g_s\underbrace{\frac{g_D}{3g_s}}_{\equiv\varepsilon_D}\left(\frac{3}{4\pi}\frac{\partial^2}{\partial z^2}\frac{1}{\left|\mathbf{r}-\mathbf{r}'\right|}+\delta\left(\mathbf{r}-\mathbf{r}'\right)\right). \tag{1.11}$$

Here, yet another dimensionless interaction parameter is introduced:

$$\varepsilon_D\equiv\frac{g_D}{3g_s}. \tag{1.12}$$

It is a measure for the strength of the dipole-dipole interaction relative to the strength of the contact interaction [6, 80]. The stability of the condensate is only guaranteed if $-1/2<\varepsilon_D<1$, which becomes apparent in the next section. Beyond the bounds of this interval, the stability of the BEC depends on the geometry of the trapping potential. The full interaction potential is now written as

$$U\left(\mathbf{r}-\mathbf{r}'\right)=g_s\left[\left(1-\varepsilon_D\right)\delta\left(\mathbf{r}-\mathbf{r}'\right)-3\varepsilon_D\frac{1}{4\pi}\frac{\partial^2}{\partial z^2}\frac{1}{\left|\mathbf{r}-\mathbf{r}'\right|}\right]. \tag{1.13}$$

This expression shows that the dipole-dipole interaction modifies the strength of the contact interaction, and that it introduces a long ranged component to the interaction potential. If $|\varepsilon_D|\ll 1$, the dipole-dipole interaction does not play an important role and may be neglected. For example, ^{87}Rb has a value of $\varepsilon_D\approx 0.007$, which means that only the contact interaction needs to be considered. Since alkali atoms have only a single electron in the outer shell, they have a magnetic dipole moment of $1\mu_B$, which is the reason for this small value of ε_D. ^{52}Cr has 6 electron in its outer shell, which leads to a magnetic dipole moment of $6\mu_B$. The magnetic dipole moment enters the parameter ε_D quadratically, so that for chromium the value of the parameter is considerably larger. It was experimentally determined to be $\varepsilon_D\approx 0.15$ [5, 81]. Here the dipole-dipole interaction does have an substantial influence on the BEC properties. A BEC where that is the case is called

a *dipolar BEC*. Besides ^{52}Cr there are other elements with large magnetic dipole moments which have already been condensed. ^{168}Er [7,82] which has a magnetic dipole moment of $7\mu_B$, or ^{164}Dy [8,83] with a magnetic dipole moment of $10\mu_B$, promise to have very large ε_D values. However, the exact values for ε_D have not yet been experimentally determined. In Ref. [8] it was suggested that ^{164}Dy may have an ε_D value larger than 1.

1.2.2 The Thomas-Fermi approximation

Solving the GPE is not an easy task. The main difficulties arise due to the non-linear term. Of course the presence of the long ranged, anisotropic dipole-dipole interaction does not simplify the matter. In general, for both cases ($\varepsilon_D = 0$ and $\varepsilon_D \neq 0$), the stationary GPE needs to be solved numerically. However, there is a useful approximation which can be applied in case that there is a sufficiently large number of atoms in the condensate. If this is the case, the shape of the ground state is determined between the balance of the interaction term, which in the case of a repulsive interaction potential drives the atoms apart, and the external trapping potential, which keeps the atoms together. It turns out that the kinetic term becomes more and more negligible. That this is actually the case can be seen by appropriately scaling the GPE [84]. It is useful to split this discussion into two parts: First the case without dipole-dipole interaction is discussed. The effects of $\varepsilon_D \neq 0$ are discussed afterward.

It is known from the linear Schrödinger equation (see for example [85,86]) that the harmonic oscillator energy scale is given by $\epsilon_{\mathrm{ho}} = \hbar\omega$, where ω is the geometric mean of the three trap frequencies: $\omega = (\omega_x\omega_y\omega_z)^{1/3}$. In the following ϵ_{ho} is used as energy scale. The length ξ is used as measure of distance. Next, the GPE is scaled using the quantities $\tilde{\mathbf{r}} = \mathbf{r}/\xi$, $\tilde{\mu} = \mu/\epsilon_{\mathrm{ho}}$, and $\tilde{\omega}_a = \omega_a/\omega$, with $a \in \{x, y, z\}$. The appropriate scaling of the wave function is derived from the normalization condition

$$\int \mathrm{d}\mathbf{r}\ |\psi(\mathbf{r})|^2 = 1 \stackrel{!}{=} \int \mathrm{d}\tilde{\mathbf{r}}\ \left|\tilde{\psi}(\tilde{\mathbf{r}})\right|^2 = \int \mathrm{d}\mathbf{r}\ \frac{\left|\tilde{\psi}(\tilde{\mathbf{r}})\right|^2}{\xi^3} \quad \Rightarrow \psi(\mathbf{r}) = \frac{\tilde{\psi}(\tilde{\mathbf{r}})}{\xi^{3/2}}.$$

The scaled GPE reads

$$\begin{aligned}\tilde{\mu}\cdot\tilde{\psi}(\tilde{\mathbf{r}}) \;=\; \Bigg\{ &-\frac{1}{\xi^2}\frac{\hbar}{m\omega}\frac{1}{2}\tilde{\boldsymbol{\nabla}}^2 + \frac{1}{2}\frac{m\omega}{\hbar}\xi^2\left(\tilde{\omega}_x^2\tilde{x}^2 + \tilde{\omega}_y^2\tilde{y}^2 + \tilde{\omega}_z^2\tilde{z}^2\right) \\ &+4\pi\frac{Na_s\hbar}{m\omega\xi^3}\left|\tilde{\psi}(\tilde{\mathbf{r}})\right|^2\Bigg\}\cdot\tilde{\psi}(\tilde{\mathbf{r}}).\end{aligned}$$

Consider the case where the kinetic term and the harmonic potential term are of the same order. Equating the coefficients of the two terms yields

$$\frac{1}{\xi^2}\frac{\hbar}{m\omega} = \frac{m\omega}{\hbar}\xi^2 \quad \Rightarrow \xi = \sqrt{\frac{\hbar}{m\omega}} \equiv a_\omega,$$

and the GPE takes the guise

$$\tilde{\mu}\cdot\tilde{\psi}\left(\tilde{\mathbf{r}}\right) = \left\{-\frac{1}{2}\tilde{\boldsymbol{\nabla}}^2 + \frac{1}{2}\left(\tilde{\omega}_x^2\tilde{x}^2 + \tilde{\omega}_y^2\tilde{y}^2 + \tilde{\omega}_z^2\tilde{z}^2\right) + 4\pi\frac{Na_s}{a_\omega}\left|\tilde{\psi}\left(\tilde{\mathbf{r}}\right)\right|^2\right\}\cdot\tilde{\psi}\left(\tilde{\mathbf{r}}\right).$$

The length scale associated with this case is found to be the harmonic oscillator length a_ω. This is the length scale that is found for the harmonic oscillator ground state from the linear Schrödinger equation. As long as $Na_s \ll a_\omega$ the interaction term can be neglected and the ground state is dominated by the kinetic term and the external potential term. The result is the linear Schrödinger equation for a harmonic oscillator.

Next, consider the case that the external potential term and the interaction term are of the same order. Again the coefficients of the respective terms are equated in order to determine the associated length scale:

$$4\pi\frac{Na_s\hbar}{m\omega\xi^3} = \frac{1}{2}\frac{m\omega}{\hbar}\xi^2 \quad \Rightarrow \xi = \left(8\pi\frac{Na_s}{a_\omega}\right)^{1/5} a_\omega \equiv \Lambda_{\mathrm{TF}}.$$

A convenient, dimensionless parameter which describes the strength of the s-wave interaction is given by

$$G_N = 8\pi\frac{Na_s}{a_\omega}. \tag{1.14}$$

It sets the strength of the contact interaction in relation to the harmonic trapping potential. With $\xi = \Lambda_{\mathrm{TF}} = G_N^{1/5}a_\omega$ the GPE reads

$$\tilde{\mu}\cdot\tilde{\psi}\left(\tilde{\mathbf{r}}\right) = \left(-\frac{1}{2}\frac{1}{G_N^{2/5}}\tilde{\boldsymbol{\nabla}}^2 + \frac{1}{2}G_N^{2/5}\left(\tilde{\omega}_x^2\tilde{x}^2 + \tilde{\omega}_y^2\tilde{y}^2 + \tilde{\omega}_z^2\tilde{z}^2\right) + \frac{1}{2}G_N^{2/5}\left|\tilde{\psi}\left(\tilde{\mathbf{r}}\right)\right|^2\right)\cdot\tilde{\psi}\left(\tilde{\mathbf{r}}\right).$$

This clearly shows that the kinetic term becomes more and more insignificant as the value of the parameter G_N increases. As the number of atoms in the BEC becomes larger, eventually the region is reached where $Na_s \gg a_\omega$, and with that also $G_N \gg 1$. In this limit the kinetic term in the GPE can be neglected, which leads to the so-called *Thomas-Fermi* (TF) approximation. In this limit the GPE reduces to an algebraic equation where the non-linear term is no longer an obstacle. The result is the TF equation, which in the unscaled form reads

$$V_{\mathrm{T}}(\mathbf{r}) + N g_s |\psi(\mathbf{r})|^2 = \mu. \tag{1.15}$$

Defining the atom density $n_{\mathrm{TF}}(\mathbf{r}) = N|\psi(\mathbf{r})|^2$, the above equation yields

$$\begin{aligned} n_{\mathrm{TF}}(\mathbf{r}) &= \frac{1}{g_s}\left[\mu - \frac{m}{2}\left(\omega_x^2 x^2 + \omega_y^2 y^2 + \omega_z^2 z^2\right)\right] \\ &= n_0^{(0)}\left(1 - \frac{x^2}{\left[\lambda_x^{(0)}\right]^2} - \frac{y^2}{\left[\lambda_y^{(0)}\right]^2} - \frac{z^2}{\left[\lambda_z^{(0)}\right]^2}\right). \end{aligned} \tag{1.16}$$

Within the TF approximation, a BEC in an harmonic trap has an ellipsoidal shape. The three TF semi axes of the BEC are given by

$$\lambda_a^{(0)} = \sqrt{\frac{2\mu}{m\omega_a^2}}, \quad a \in \{x, y, z\} \tag{1.17}$$

and the central atom density of the BEC is

$$n_0^{(0)} = \frac{\mu^{(0)}}{g_s}. \tag{1.18}$$

The superscript (0) indicates that these are the quantities for a non-dipolar BEC with $\varepsilon_D = 0$. The chemical potential $\mu^{(0)}$ is fixed by the normalization condition

$$\int_{\mathbb{D}_{\mathrm{TF}}} \mathrm{d}\mathbf{r}\, n_{\mathrm{TF}}(\mathbf{r}) = N, \tag{1.19}$$

where the integration domain $\mathbb{D}_{\mathrm{TF}}$ is defined as the region where expression (1.16) is positive

$$\mathbb{D}_{\mathrm{TF}} = \left\{ \mathbf{r} \in \mathbb{R}^3 \,\middle|\, \frac{x^2}{\left[\lambda_x^{(0)}\right]^2} + \frac{y^2}{\left[\lambda_y^{(0)}\right]^2} + \frac{z^2}{\left[\lambda_z^{(0)}\right]^2} \leq 1 \right\}.$$

Integral (1.19) can be solved analytically, which yields the chemical potential

$$\mu^{(0)} = 15^{2/5}\left(\frac{N a_s}{a_\omega}\right)^{2/5} \frac{\hbar\omega}{2}. \tag{1.20}$$

This implies that the central density of the TF ellipsoid reads

$$n_0^{(0)} = \frac{15}{8\pi} \frac{N}{\lambda_x^{(0)} \lambda_y^{(0)} \lambda_z^{(0)}}. \tag{1.21}$$

The presence of the dipole-dipole interaction complicates the situation considerably. Under the scaling transformation $\mathbf{r} \to \tilde{\mathbf{r}} = \mathbf{r}/\xi$, the dipole-dipole interaction potential U_{md} behaves identical to the s-wave scattering potential U_s. Thus the previously presented argument, which motivated the Thomas-Fermi approximation, still holds [84]. However, the resulting TF equation

$$(1-\varepsilon_D)\, n_{\mathrm{TF}}(\mathbf{r}) - 3\varepsilon_D \frac{1}{4\pi}\frac{\partial^2}{\partial z^2}\int\limits_{\mathbb{D}_{\mathrm{TF}}} \mathrm{d}\mathbf{r}' \frac{n_{\mathrm{TF}}(\mathbf{r})}{|\mathbf{r}-\mathbf{r}'|} = \frac{\mu - V_T(\mathbf{r})}{g_s} \tag{1.22}$$

can no longer be simply solved for the density distribution. The density distribution $n_{\mathrm{TF}}(\mathbf{r})$ is determined by this integral equation. The integration domain is again defined as the region where the density distribution remains positive. It has been shown by Eberlein et al. [80] that the density distribution for the case $\varepsilon_D \neq 0$ remains ellipsoidal. The dipole-dipole interaction only modifies the semi axes of the BEC, so that the density distribution is still of the form

$$n_{\mathrm{TF}}(\mathbf{r}) = n_0 \left(1 - \frac{x^2}{\lambda_x^2} - \frac{y^2}{\lambda_y^2} - \frac{z^2}{\lambda_z^2}\right). \tag{1.23}$$

Indeed, with this ansatz for the density distribution the TF equation can be solved self consistently. The first task is to find a solution to the integral that appears in (1.22). This integral has the same form as an integral which describes the gravitational potential generated by an ellipsoidal mass density distribution. Chandrasekhar encountered the same type of integral during his study of rotating gas clouds. Due to the rotation the density distribution of the gas clouds becomes ellipsoidal, just like the atom distribution in the BEC. Chandrasekhar shows in Ref. [87] that the three dimensional integral over this ellipsoidal density distribution has an exact one dimensional representation. With $\rho(\mathbf{r}) = n_{\mathrm{TF}}(\mathbf{r})/n_0$, the potential at a point inside the ellipsoid $\mathbf{r} \in \mathbb{D}_{\mathrm{TF}}$ is expressed as

$$\phi(\mathbf{r}) = \frac{1}{4\pi}\int\limits_{\mathbb{D}_{\mathrm{TF}}} \mathrm{d}\mathbf{r}' \frac{\rho(\mathbf{r}')}{|\mathbf{r}-\mathbf{r}'|} = \frac{\lambda_x\lambda_y\lambda_z}{8}\int\limits_0^\infty \mathrm{d}u \frac{\left(1 - \frac{x^2}{\lambda_x^2+u} - \frac{y^2}{\lambda_y^2+u} - \frac{z^2}{\lambda_z^2+u}\right)^2}{\sqrt{(\lambda_x^2+u)\left(\lambda_y^2+u\right)(\lambda_z^2+u)}}. \tag{1.24}$$

At a point $\mathbf{r} \notin \mathbb{D}_{\mathrm{TF}}$ outside the density distribution it is given by

$$\phi(\mathbf{r}) = \frac{\lambda_x\lambda_y\lambda_z}{8}\int\limits_{W(\mathbf{r})}^\infty \mathrm{d}u \frac{\left(1 - \frac{x^2}{\lambda_x^2+u} - \frac{y^2}{\lambda_y^2+u} - \frac{z^2}{\lambda_z^2+u}\right)^2}{\sqrt{(\lambda_x^2+u)\left(\lambda_y^2+u\right)(\lambda_z^2+u)}}. \tag{1.25}$$

$W(\mathbf{r})$ is the elliptic coordinate of the point $\mathbf{r}$ and is defined by

$$\frac{x^2}{\lambda_x^2 + W(\mathbf{r})} + \frac{y^2}{\lambda_y^2 + W(\mathbf{r})} + \frac{z^2}{\lambda_z^2 + W(\mathbf{r})} = 1. \tag{1.26}$$

Geometrically this equation defines an ellipsoid shell with semi axes $\bar{\lambda}_a = \sqrt{\lambda_a^2 + W(\mathbf{r})}$, which contains the point $\mathbf{r}$. For the moment only the case $\mathbf{r} \in \mathbb{D}_{\mathrm{TF}}$ is required. In Chapter 3 also the case $\mathbf{r} \notin \mathbb{D}_{\mathrm{TF}}$ becomes important.

It is known that the solution to the potential problem posed by (1.24) is given by the Poisson equation $-\boldsymbol{\nabla}^2 \phi(\mathbf{r}) = \rho(\mathbf{r})$. This equation is used to replace the TF density distribution in equation (1.22), which then takes the guise

$$-\frac{1}{n_0}\left\{(1-\varepsilon_D)\left(\frac{\partial^2}{\partial x^2} + \frac{\partial^2}{\partial y^2}\right) + (1+2\varepsilon_D)\frac{\partial^2}{\partial z^2}\right\}\phi(\mathbf{r}) = \frac{\mu - V_{\mathrm{T}}(\mathbf{r})}{g_s}.$$

In order for the solution of this differential equation to be stable, the differential operator needs to be positive definite [57], which is only the case for

$$-\frac{1}{2} < \varepsilon_D < 1. \tag{1.27}$$

This means that only in this interval the stability of the BEC is guaranteed. Beyond this region the BEC might still be stable, depending in the trapping potential V_{T}.

What is actually needed to solve the TF equation is the derivative of the potential given in (1.24). The derivative is easily calculated and reads

$$\frac{\partial^2}{\partial z^2}\phi(\mathbf{r}) = -\frac{\lambda_x \lambda_y \lambda_z}{2}\int_0^\infty \mathrm{d}u \frac{\left(1 - \frac{x^2}{\lambda_x^2+u} - \frac{y^2}{\lambda_y^2+u} - 3\frac{z^2}{\lambda_z^2+u}\right)\frac{1}{\lambda_z^2+u}}{\sqrt{(\lambda_x^2+u)\left(\lambda_y^2+u\right)(\lambda_z^2+u)}}.$$

At this point it is convenient to define the so-called index integrals [57, 87]

$$\begin{aligned} I_a &\equiv I_a(\lambda_x, \lambda_y, \lambda_z) \\ &= \int_0^\infty \frac{\mathrm{d}u}{\sqrt{(\lambda_x^2+u)\left(\lambda_y^2+u\right)(\lambda_z^2+u)}} \frac{1}{(\lambda_a^2+u)} \end{aligned} \tag{1.28}$$

and

$$\begin{aligned} I_{ab} &\equiv I_{ab}\left(\lambda_x, \lambda_y, \lambda_z\right), \\ &= \int_0^\infty \frac{\mathrm{d}u}{\sqrt{\left(\lambda_x^2+u\right)\left(\lambda_y^2+u\right)\left(\lambda_z^2+u\right)}} \frac{1}{\left(\lambda_a^2+u\right)\left(\lambda_b^2+u\right)} \end{aligned} \tag{1.29}$$

with $a, b \in \{x, y, z\}$. In terms of the index integrals the expression for the second derivative of the potential $\phi(\mathbf{r})$ is written as

$$\begin{aligned} \varphi(\mathbf{r}) &\equiv \frac{\partial^2}{\partial z^2}\phi(\mathbf{r}) \\ &= -\frac{\lambda_x\lambda_y\lambda_z}{2}\left(I_z - I_{xz}x^2 - I_{yz}y^2 - 3I_{zz}z^2\right). \end{aligned} \tag{1.30}$$

Inserting everything in the TF equation and solving it for zero yields

$$\begin{aligned} 0 = &\left((1-\varepsilon_D)\, n_0 + \frac{3\varepsilon_D}{2} n_0\lambda_x\lambda_y\lambda_z I_z - \frac{\mu}{g_s}\right)\cdot 1 \\ &+\left(-\frac{(1-\varepsilon_D)\, n_0}{\lambda_x^2} - \frac{3\varepsilon_D}{2} n_0\lambda_x\lambda_y\lambda_z I_{xz} + \frac{m\omega_x^2}{2g_s}\right)\cdot x^2 \\ &+\left(-\frac{(1-\varepsilon_D)\, n_0}{\lambda_y^2} - \frac{3\varepsilon_D}{2} n_0\lambda_x\lambda_y\lambda_z I_{yz} + \frac{m\omega_y^2}{2g_s}\right)\cdot y^2 \\ &+\left(-\frac{(1-\varepsilon_D)\, n_0}{\lambda_z^2} - \frac{9\varepsilon_D}{2} n_0\lambda_x\lambda_y\lambda_z I_{zz} + \frac{m\omega_z^2}{2g_s}\right)\cdot z^2. \end{aligned} \tag{1.31}$$

This gives a set of four equations for the five unknown quantities λ_x, λ_y, λ_z, n_0 and μ. The normalization condition adds the fifth equation $n_0 = \frac{15}{8\pi}\frac{N}{\lambda_x\lambda_y\lambda_z}$. In general this system of coupled equations needs to be solved numerically. Compared to the case $\varepsilon_D = 0$, where everything is given by analytical expressions, the case with dipole-dipole interaction is a lot less convenient. For this reason, the typical approach used throughout the present work, is to consider the case $\varepsilon_D = 0$ first in order to get some analytical approximation. Afterward, the case $\varepsilon_D \neq 0$ is calculated in order to quantify the error made by the previous simplification.

In Chapter 4, a more general case of the here presented equations is needed. Namely the case that the dipoles are not oriented along one of the directions defined by the harmonic trap, but are arbitrarily orientated in one of the planes spanned by two of the trap axes. The self consistency equations for that case are presented in Ref. [57], where also the effects

on the BEC are discussed. For the convenience of the reader, the central results of Ref. [57] that are relevant for this work are also presented in Appendix A.

1.2.3 Dynamics of a BEC

The main focus of this work is on the dynamical behavior of the condensate. In order to describe the time evolution, the time dependent GPE is a suitable tool. Similar to the stationary GPE it can also be derived using a variational argument. The ground state was determined by minimizing the energy, the dynamics follows the principle of minimal action s. The action is given by

$$s\left[\psi\right] = \int_{t_1}^{t_2} \mathrm{d}t \int \mathrm{d}\mathbf{r}\, \mathcal{L},$$

where $\mathcal{L}$ is the Lagrange density [59]

$$\mathcal{L}\left[\psi\right] = \frac{i\hbar}{2}\left(\psi^* \frac{\partial \psi}{\partial t} - \psi \frac{\partial \psi^*}{\partial t}\right) - \mathcal{E}\left[\psi\right].$$

In the above expression $\mathcal{E}$ is the energy density, and one can see that for a time independent ψ, the Lagrange density reduces to the energy density. Minimizing the action s becomes equivalent to minimizing the energy E. However, if ψ is time dependent, minimizing the action yields the time dependent GPE [59, 78]

$$\begin{aligned} i\hbar \frac{\partial}{\partial t}\psi\left(\mathbf{r},t\right) &= \left(-\frac{\hbar^2}{2m}\boldsymbol{\nabla}^2 + V_{\mathrm{T}}\left(\mathbf{r}\right) + \right. \\ &\quad \left. + N \int \mathrm{d}\mathbf{r}'\, U\left(\mathbf{r}-\mathbf{r}'\right) \left|\psi\left(\mathbf{r}',t\right)\right|^2 \right) \psi\left(\mathbf{r},t\right). \end{aligned} \quad (1.32)$$

This equation describes the time evolution of a BEC at zero temperature within mean field approximation. An analytical solution of this equation is in general not possible and the use of numerical tools becomes necessary. This issue is addressed in the next chapter. However, there is a useful approximation, similar to the TF approximation in the stationary case, which provides some analytical insight. Especially in the case that V_{T} is a harmonic potential. The wave function ψ is in general a complex number, therefore it can be expressed in terms of the phase $S\left(\mathbf{r},t\right)$ and its

modulus $|\psi(\mathbf{r},t)|$. The modulus is connected to the density distribution via $n(\mathbf{r},t) = N|\psi(\mathbf{r},t)|^2$, and with that the wave function reads

$$\psi(\mathbf{r},t) = \frac{1}{\sqrt{N}}\sqrt{n(\mathbf{r},t)}e^{iS(\mathbf{r},t)}.$$

Inserting this in the time dependent GPE (1.32) yields the following set of coupled differential equations

$$\hbar\frac{\partial}{\partial t}S(\mathbf{r},t) = -\frac{\hbar}{2m}\left[\boldsymbol{\nabla}S(\mathbf{r},t)\right]^2 - V_{\mathrm{T}}(\mathbf{r}) - \int \mathrm{d}\mathbf{r}'\, U(\mathbf{r}-\mathbf{r}')\, n(\mathbf{r}',t)\,, \quad (1.33)$$

and

$$\frac{\partial}{\partial t}n(\mathbf{r},t) + \frac{\hbar}{m}\boldsymbol{\nabla}\cdot\left[n(\mathbf{r},t)\,\boldsymbol{\nabla}S(\mathbf{r},t)\right] = 0. \quad (1.34)$$

These two equations describe the time evolution of the BEC phase and the density. Equation (1.34) is the continuity equation. This becomes more obvious if the gradient of the phase is replaced by the velocity field $\mathbf{v}(\mathbf{r},t)$ via $\boldsymbol{\nabla}S(\mathbf{r},t) = \frac{m}{\hbar}\mathbf{v}(\mathbf{r},t)$. With that equation (1.34) takes the guise $\frac{\partial}{\partial t}n(\mathbf{r},t) = -\boldsymbol{\nabla}\cdot\left[n(\mathbf{r},t)\,\mathbf{v}(\mathbf{r},t)\right]$.

Furthermore, it is important to mention that in order to arrive at equation (1.33), it is necessary to drop the so-called *quantum pressure* term $-\frac{\hbar^2}{2m\sqrt{n(\mathbf{r},t)}}\boldsymbol{\nabla}^2\sqrt{n(\mathbf{r},t)}$. This term describes the kinetic energy associated with the spatial change of the wave function modulus. It is equivalent to the TF approximation in the stationary case. This becomes evident by inserting $\psi(\mathbf{r},t) = e^{-i\frac{\mu}{\hbar}t}\psi(\mathbf{r})$ in the time dependent GPE, which yields the stationary GPE (1.4). Equations (1.33) and (1.34) are often referred to as hydrodynamic equations, and in the stationary case reduce to the TF equation (1.22).

From the TF approximation the ground state density distribution of the BEC is known to be an ellipsoid. As an ansatz for the time dependent density distribution, an ellipsoid with time dependent semi axes, which can also perform center-of-mass motions, seems a natural choice. The ansatz reads

$$n(\mathbf{r},t) = n_0(t)\left(1 - \frac{(x+\eta_x(t))^2}{\lambda_x^2(t)} - \frac{(y+\eta_y(t))^2}{\lambda_y^2(t)} - \frac{(z+\eta_z(t))^2}{\lambda_z^2(t)}\right). \quad (1.35)$$

The center-of-mass motion is described by $\boldsymbol{\eta}(t)$. Making a similar ansatz for the phase $S(\mathbf{r},t)$ and inserting both in the hydrodynamic equations yields after some calculation the following set of equations:

$$0 = \frac{\ddot{\lambda}_a}{\lambda_a} + \omega_a^2 - \frac{2g_s}{m}n_0\left[\frac{1-\varepsilon_D}{\lambda_a^2} + C_a\varepsilon_D\lambda_x\lambda_y\lambda_z I_{az}\right], \quad \text{for } a \in \{x,y,z\} \quad (1.36)$$

with

$$C_x = C_y = \frac{3}{2}, \quad \text{and} \quad C_z = \frac{9}{2},$$

and for the center-of-mass motion the equations read

$$\ddot{\eta}_a = -\omega_a^2 \eta_a, \quad a \in \{x, y, z\}\,.$$

This means that the time evolution of the semi axes is described by a set of three coupled differential equations. The center-of-mass motion is simply a harmonic oscillation with frequency ω_a in the respective direction. This result is important, since it shows that in a harmonic potential the center-of-mass motion is decoupled from the ellipsoidal shape fluctuations of the BEC. For the discussion presented in Chapter 5 this is a major issue. The time evolution of the semi axes based on (1.36) was studied for the non-dipolar case in Ref. [88] and for the dipolar case in Ref. [89].

Since the equations presented in (1.36) are still difficult to solve, one can make some further simplifications. If only small amplitude oscillations are of interest, it is sufficient to consider linear fluctuations, $\delta s\,(\mathbf{r}, t)$ and $\delta n\,(\mathbf{r}, t)$, around the equilibrium quantities. The ansatz for the phase reads

$$S\,(\mathbf{r}, t) = -\frac{\mu}{\hbar} t + \delta s\,(\mathbf{r}, t)$$

and for the density

$$n\,(\mathbf{r}, t) = n_{\mathrm{TF}}\,(\mathbf{r}) + \delta n\,(\mathbf{r}, t)\,.$$

The density fluctuation $\delta n\,(\mathbf{r}, t)$ needs to be chosen such that $n\,(\mathbf{r}, t)$ remains an ellipsoid at all times. Additionally the density fluctuations must conform with particle conservation. This leads to a set of three coupled ordinary differential equations

$$\frac{2 n_0 g_s}{m} \begin{pmatrix} C_{xx,xx} & C_{xx,yy} & C_{xx,zz} \\ C_{yy,xx} & C_{yy,yy} & C_{yy,zz} \\ C_{zz,xx} & C_{zz,yy} & C_{zz,zz} \end{pmatrix} \begin{pmatrix} \widehat{\rho}_{xx} \\ \widehat{\rho}_{yy} \\ \widehat{\rho}_{zz} \end{pmatrix} = \Omega^2 \begin{pmatrix} \widehat{\rho}_{xx} \\ \widehat{\rho}_{yy} \\ \widehat{\rho}_{zz} \end{pmatrix}. \tag{1.37}$$

A detailed derivation and discussion of this result is given in Ref. [57]. The shape fluctuation $\delta n\,(\mathbf{r}, t)$ of the density is connected to the coefficients $\widehat{\rho}_{aa}$. The definitions of $\widehat{\rho}_{aa}$ and the matrix elements $C_{aa,bb}$ are listed in Appendix A. The eigenmodes of the system are given by the eigenvectors of (1.37). The corresponding oscillation frequency Ω (more precisely the square of the frequency) is the eigenvalue. The here described modes are called the *monopole-quadrupole modes* of the BEC. There are three more eigenmodes

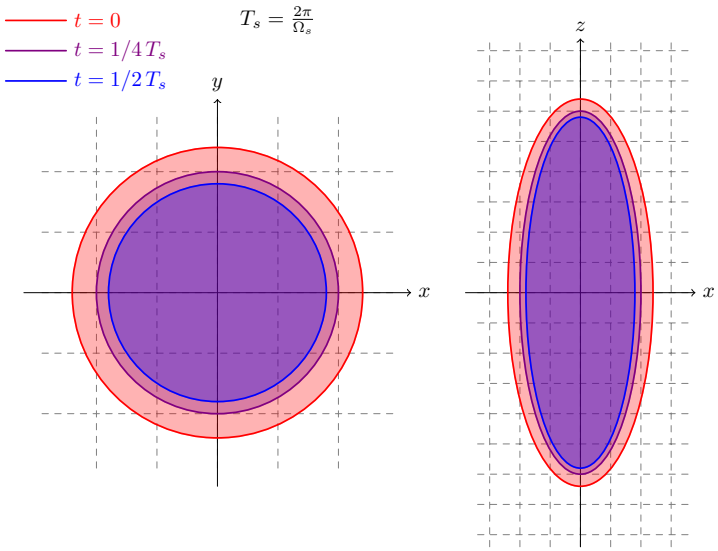

Figure 1.2: Monopole mode density fluctuation $\boldsymbol{\rho}(t) = \hat{\boldsymbol{\rho}}_s \cos(\Omega_s t)$ for a BEC that is elongated in the z-direction. Depicted are the contour lines $n(\mathbf{r}, t) = 0$. The left panel shows the contour line in the x-y-plane and the right panel in the x-z-plane. The lines are shown for three different times: $t = 0$ (red), $t = T_s/4$ (purple), and $t = T_s/2$ (blue). The BEC performs a periodic, isotropic contraction and expansion. Therefore the mode is often called breather mode.

of this type which were omitted here, the so-called scissor modes [90–92]. They are connected to coefficients $\widehat{\rho}_{xy}$, $\widehat{\rho}_{xz}$, and $\widehat{\rho}_{yz}$ (see Ref. [57] or Appendix A). For the discussed setup, the scissor modes are not coupled to the other three monopole-quadrupole modes. Since they do not play any role in the following discussion it is not necessary to go into further details here. An illustrative example is the case $\varepsilon_D = 0$ and an spherical trapping potential with $\omega_x = \omega_y = \omega_z = \omega$, the eigenvalue equation reads

$$\omega^2 \begin{pmatrix} 3 & 1 & 1 \\ 1 & 3 & 1 \\ 1 & 1 & 3 \end{pmatrix} \begin{pmatrix} \widehat{\rho}_{xx} \\ \widehat{\rho}_{yy} \\ \widehat{\rho}_{zz} \end{pmatrix} = \Omega^2 \begin{pmatrix} \widehat{\rho}_{xx} \\ \widehat{\rho}_{yy} \\ \widehat{\rho}_{zz} \end{pmatrix}.$$

The mode with the highest eigenvalue is the s-wave symmetric $\widehat{\boldsymbol{\rho}}_s = [1,1,1]^T$ with the corresponding eigenvalue $\Omega_s^2 = 5\omega^2$. This mode is often referred to as breather mode, which becomes clear by the form of this particular shape oscillation, depicted in Fig. 1.2. The eigenvector $\widehat{\boldsymbol{\rho}}_s$ describes an isotropic expansion and compression of the BEC. It is interesting to note, that in a spherical trap the eigenvalue of this mode does not depend on the strength of the dipole-dipole interaction, even though the BEC itself may no longer be a sphere. Also, the isotropy of the motion is not affected by the value of ε_D [57]. If the trap is not isotropic this is no longer the case. The remaining two modes are degenerate in a spherical trap. They have similar shape oscillations, only in different directions. One of the two eigenvectors is given by $\widehat{\boldsymbol{\rho}}_{x^2-y^2} = [1,-1,0]^T$ with the eigenvalue $\Omega^2_{x^2-y^2} = 2\omega^2$. While the density distribution expands in the x-direction, it contracts in the y-direction, and vice versa (see Fig. 1.3). The remaining mode reads $\widehat{\boldsymbol{\rho}}_{z^2} = [-1,0,1]^T$, and the eigenvalue is $\Omega^2_{z^2} = 2\omega^2$. The reason for the different denotation of the modes is the fact that for an elongated trap with $\omega_z > \omega_x = \omega_y$, this mode displays mainly a d_{z^2} symmetry (see Fig. 1.4). In elongated traps the frequency of $\widehat{\boldsymbol{\rho}}_{z^2}$ goes down while the frequency of $\widehat{\boldsymbol{\rho}}_{x^2-y^2}$ hardly changes at all, see Fig 1.5. It is also interesting to note that $\widehat{\boldsymbol{\rho}}_{x^2-y^2}$ remains an exact eigenvalue independent of the dipole-dipole interaction parameter ε_D, provided the dipoles are oriented in the z-direction. In Figs. 1.2 – 1.4 the three types of shape fluctuations are illustrated.

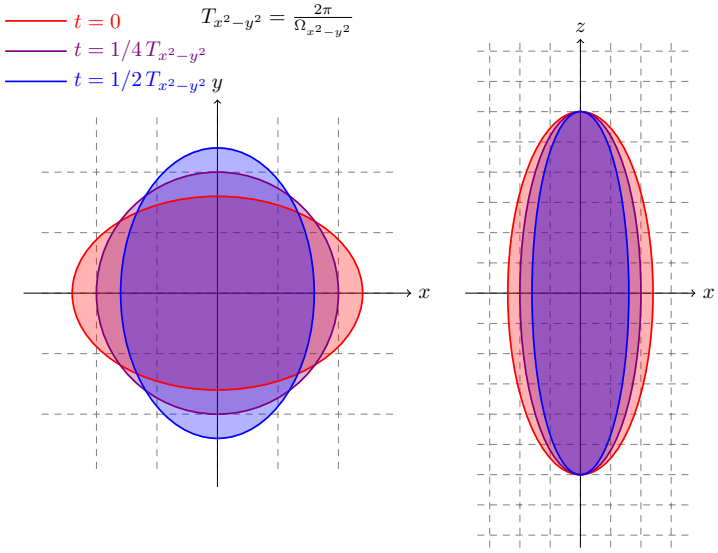

Figure 1.3: $d_{x^2-y^2}$-mode density fluctuation $\boldsymbol{\rho}(t) = \hat{\boldsymbol{\rho}}_{x^2-y^2} \cos(\Omega_{x^2-y^2} t)$: While the BEC contracts in the x-direction it expands in the y-direction. No motion takes place in the z-direction.

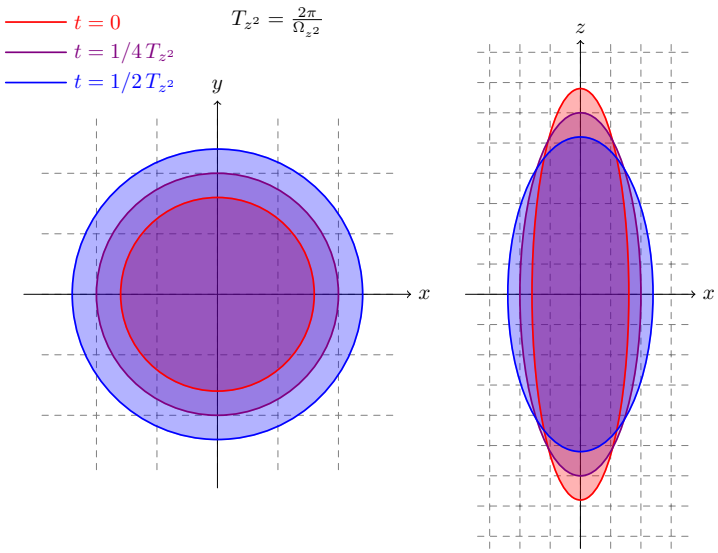

Figure 1.4: d_{z^2}-mode density fluctuation $\boldsymbol{\rho}(t) = \hat{\boldsymbol{\rho}}_{z^2} \cos(\Omega_{z^2} t)$: While the BEC contracts in the z-direction, it symmetrically expands in the x-y-plane.

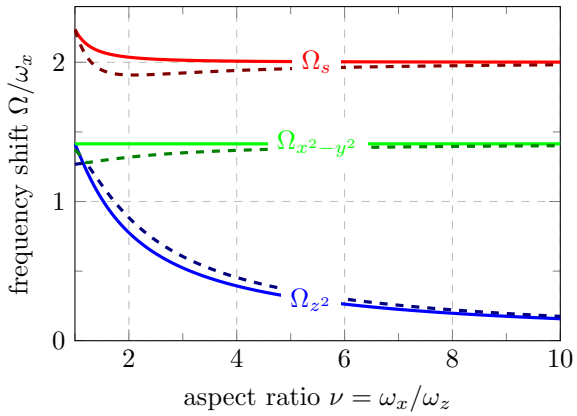

Figure 1.5: The mode frequencies Ω_s, $\Omega_{x^2-y^2}$, and Ω_{z^2} as a function of the trap aspect ratio $\nu = \omega_x/\omega_z$. The other trap aspect ratio is $\kappa = \omega_y/\omega_z = 1$. The solid curves are for a non-dipole BEC, i.e. $\varepsilon_D = 0$. The dashed curves correspond to a dipolar BEC with $\varepsilon_D = 0.8$.

1.3 The superconductor as a magnetic mirror

The magnetic field generated by a magnetic dipole in free space is different than the magnetic field of a dipole close to an ideal conductor. In this section the influence of a superconducting surface on the field of a magnetic dipole is discussed.

1.3.1 Boundary condition for the magnetic field

First, it is necessary to discuss the boundary condition for a magnetic field $\mathbf{B}$ at an ideal conducting surface. The magnetic induction field must of course satisfy the Maxwell equations of electro-magnetism (see for example [79]). Consider the following Maxwell equation $\boldsymbol{\nabla} \cdot \mathbf{B} = 0$, or, for the intended purpose more useful, its integral form $\oiint_{\partial V} \mathrm{d}\mathbf{S} \cdot \mathbf{B} = 0$. This equation holds for any Volume V, so one may chose V such that it contains the interface area of two different media. The size of the box can be arbitrary small. One may shrink the height of the box so that the only contribution into or out of the box comes from two the faces with area ΔA parallel to the interface. Say $\hat{\mathbf{n}}$ is the normal vector of the interface plane, this means that $\oiint_{\partial V} \mathrm{d}\mathbf{S} \cdot \mathbf{B} = (\mathbf{B}_1 \cdot \hat{\mathbf{n}} - \mathbf{B}_2 \cdot \hat{\mathbf{n}})\, \Delta A = (B_{n1} - B_{n2})\, \Delta A = 0$, which is equivalent to $B_{n1} = B_{n2}$. Thus, the normal component of the magnetic field

is continuous at the interface plane. Say one medium is a superconductor. Due to the Meisner-Ochsenfeld effect the magnetic field inside a superconductor vanishes. This means of course that also the normal component is zero, thus the boundary condition for the normal component of the field reads

$$\mathbf{B} \cdot \hat{\mathbf{n}} = 0. \tag{1.38}$$

In order to derive the boundary condition for the tangential component of the magnetic field, consider the following Maxwell equation: $\boldsymbol{\nabla} \times \mathbf{B} = \mu_0 \mathbf{j} - \mu_0 \varepsilon_0 \partial_t \mathbf{E}$, where $\mathbf{j}$ is the electrical current density and $\mathbf{E}$ the electrical field. In its integral form this equation reads $\oint_{\partial A} \mathrm{d}\mathbf{r} \cdot \mathbf{B} = \mu_0 \int_A \mathrm{d}\mathbf{f} \cdot \mathbf{j} - \mu_0 \varepsilon_0 \partial_t \int_A \mathrm{d}\mathbf{f} \cdot \mathbf{E}$. Again this equation must hold for an arbitrary area A, so one may chose it to be a rectangle situated perpendicular to the interface of two media. The height of the rectangle may be reduced so that it only encloses the interface. As the surface area A goes to zero, also the last term in the Maxwell equation vanishes. However, the first term containing the current does not necessarily vanish if there is a surface current $\mathbf{j}_s = j_s \cdot \hat{\mathbf{t}}$ flowing along the interface. After all that has been said one can write $\oint_{\partial A} \mathrm{d}\mathbf{r} \cdot \mathbf{B} = \left(\mathbf{B}_1 \cdot \hat{\mathbf{t}} - \mathbf{B}_2 \cdot \hat{\mathbf{t}}\right) \Delta l = (B_{t1} - B_{t2}) \, \Delta l = \mu_0 \int_A \mathrm{d}\mathbf{f} \cdot \mathbf{j} = \mu_0 j_s \Delta l$, which yields $B_{t1} - B_{t2} = \mu_0 j_s$. This means that if there is a surface current present, the tangential component makes a jump. So even though the magnetic field may be zero inside the conductor, it may still have a finite tangential component at the surface.

All that has been said is of course only true, if the magnetic field inside the conductor actually vanishes completely. In case of a superconductor this is not strictly true. As is well known (see for example [74]), the magnetic field penetrates the superconductor within a thin surface layer. The thickness λ_L of this layer is the so-called London penetration depth. If one is interested in the magnetic field distribution on a length scale of the penetration depth, the above given arguments no longer hold. If the length scale of interest is much larger then the penetration depth, the above given argument is a good approximation and boundary condition (1.38) remains valid. The typical length scale for the penetration depth is $\lambda_L \sim 100\,\mathrm{nm}$ (for example $\lambda_L^{(\mathrm{Nb})} \approx 40\,\mathrm{nm}$). For the present work the relevant length scale is of the order of $\sim 10\,\mu\mathrm{m}$. Thus, boundary condition (1.38) is a good approximation.

1.3.2 The superconducting surface as a magnetic mirror

Now that the boundary condition is known, it is possible to investigate what effect this has on the magnetic field of a nearby dipole $\boldsymbol{\mu}_\mathrm{d} =$

$(\mu_x, \mu_y, \mu_z)^T$. In free space the magnetic induction field generated by a dipole reads [79]

$$\mathbf{B}_{\mathrm{d,free}}(\mathbf{r}) = \frac{\mu_0}{4\pi}\left[\frac{3(\boldsymbol{\mu}_\mathrm{d}\cdot\mathbf{r})\,\mathbf{r}}{|\mathbf{r}|^5} - \frac{\boldsymbol{\mu}_\mathrm{d}}{|\mathbf{r}|^3}\right].$$

The presence of the superconductor modifies the field in such a way that the boundary condition at the surface is met. Say the superconducting plane is located at $x = 0$ and the magnetic dipole moment at $\mathbf{r}_\mathrm{d} = x_d \cdot \hat{\mathbf{e}}_x$. Now a second magnetic dipole $\boldsymbol{\mu}_\mathrm{d}^{(m)}$ is introduced at the position $\mathbf{r}_\mathrm{d}^{(m)} = -x_d \cdot \hat{\mathbf{e}}_x$. It is the mirror dipole of the original dipole and is given by $\boldsymbol{\mu}_\mathrm{d}^{(m)} = (-\mu_x, \mu_y, \mu_y)^T$. The mirror dipole generates itself a magnetic field $\mathbf{B}_{\mathrm{d,free}}^{(m)}$. By adding up $\mathbf{B}_{\mathrm{d,free}}$ and $\mathbf{B}_{\mathrm{d,free}}^{(m)}$ a magnetic field is constructed which satisfies the boundary condition at the surface (see Fig. 1.6). While the normal component of the field vanishes, the tangential component does not. This is due to currents flowing at the surface of the superconductor. These *screening currents* generate a magnetic field which compensates the external field. Thus the interior of the superconductor remains field free. For the remainder of this work, these screening currents are referred to as *eddy currents*. Usually the term eddy current is used in the context of time dependent magnetic fields. Since in the following oscillating dipoles are considered, it seems appropriate to use the term eddy current rather than screening current. However, the oscillation frequency of the considered dipole motion ranges from a few Hz up to 1 kHz. A typical gap frequency of a superconductor (for example Nb) is around ~ 100 GHz. This is by far larger then the oscillation frequencies of the dipole moments. This means that the magnetic field of the oscillating dipoles can be regarded as quasi-statical in the sense that it is not necessary to account for effects arising due to dynamical electro-magnetic fields. For all means and purposes the superconductor in the discussed setup can be regarded as a perfect magnetic mirror.

For the study of the interaction between the superconductor and the dipolar BEC, it is very convenient to replace the effect of the superconductor, or rather the effect of the induced eddy currents in the surface, by the effect of a magnetic mirror image of the dipolar BEC. It is equivalent to study the interaction between the BEC and the mirror BEC. The interaction potential between the two is given by the dipole-dipole interaction potential and is of the same form as (1.8).

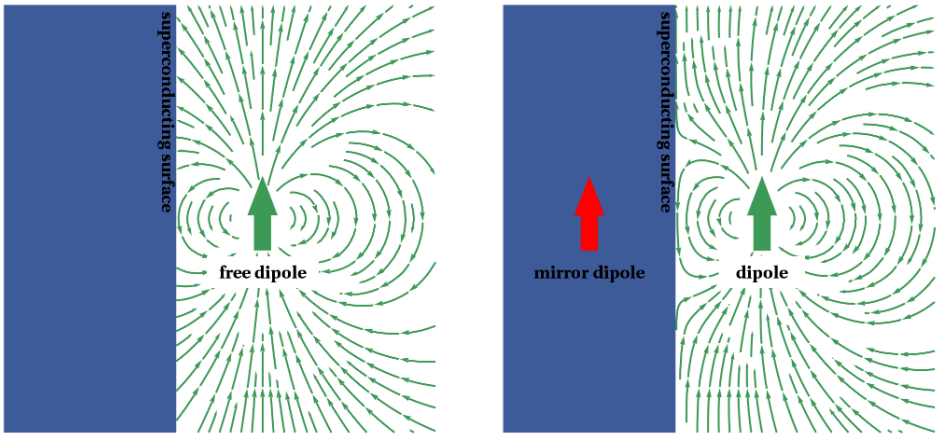

Figure 1.6: The left panel depicts the magnetic field distribution generated by a magnetic dipole in free space. Obviously, the boundary condition $\mathbf{B} \cdot \hat{\mathbf{n}} = 0$ is not satisfied at the surface of the superconductor. The right panel depicts the field distribution for the case that the field of a mirror dipole is superposed. The resulting field lines are distorted such that the boundary condition is satisfied.

Chapter 2

Numerics

A central task of many quantum mechanical problems is the solution of the Schrödinger equation (SE). For complex systems this can be a quite difficult undertaking. In many cases an analytical solution is not possible. There are basically two different approaches to deal with this problem. The first one would be to simplify the problem so far, until an analytical solution becomes possible. Of course the simplified problem still needs to represent the physical system under consideration. Usually, with an analytical approximation this is only the case for a certain parameter regime. The second approach is to leave the original problem unaltered and to search for a numerical solution. Both approaches have their advantages and disadvantages. While an analytical approximation often grants more insight into the problem by some functional relations, the numerical solution usually yields results for a broader parameter range. In general it is reasonable to use both approaches. This allows to compare the results and with that also validate them. If the system becomes too complex to find a meaningful analytical approximation, numerical solutions are often the only way to gain some insight. In the previous chapter it was already established that a weakly interacting Bose gas at $T = 0$ can be described with the GPE. It is essentially a SE with a non-linear term. Not only does the non-linear term in the GPE make the analytical solution more difficult, it also complicates the numerical solution. The numerical methods, used to solve the SE, need to be altered in order to be applicable to the GPE. Throughout the course of this work, the stationary as well as the time dependent GPE need to be solved. In this chapter a method for solving the time independent GPE (1.4) is presented and one for solving the time dependent GPE (1.32). Further complications in solving the GPE arise from the dipole-dipole interaction between the atoms in the BEC. A way to deal with this issue is discussed as well. The potential generated by the mirror BEC poses an additional

issue which is discussed in the next chapter.

The mentioned complications, regarding the numerical solution of the GPE, lead to an increased computational effort compared to the solution of the linear SE. To reduce the time necessary to compute the solution, many parts of the computations are moved from the central processing unit (CPU) to the graphics processing unit (GPU). This allows a parallelization of the computation. The numerical methods presented in this chapter were all implemented using CUDA [93].

2.1 The GPE of a dipolar BEC

Before starting the discussion about the numerical solution of the GPE, it is useful to rewrite the GPE using units that are more convenient for the numerical calculation. The limit for large numbers of atoms N was already discussed. The natural length scale of the BEC for this case is given by $\Lambda_{\mathrm{TF}} = G_N^{1/5} a_\omega$ (see Section 1.2.2). Using Λ_{TF} as unit of length leads to a divergence of the kinetic energy term for the case $G_N = 0$. To avoid this, the oscillator length a_ω is used as a unit of length. An appropriate energy scale is presented by $\hbar\omega$. The time is measured in units $T_x = \frac{2\pi}{\omega_x}$. For the dynamical simulations this is a convenient time unit, since center-of-mass oscillations in the x-direction are at the core of the investigation. As unit for the frequency, the geometric mean of the trap frequencies $\omega = \left(\omega_x\omega_y\omega_z\right)^{1/3}$ is an appropriate choice. Using this frequency unit, the harmonic trap frequencies can be expressed using the trap frequency aspect ratios

$$\nu = \frac{\omega_x}{\omega_z} \quad \text{and} \quad \kappa = \frac{\omega_y}{\omega_x}, \tag{2.1}$$

thus the trap frequencies read

$$\frac{\omega_x}{\omega} = \left(\frac{\nu}{\kappa}\right)^{1/3}, \quad \frac{\omega_y}{\omega} = \left(\kappa^2\nu\right)^{1/3}, \quad \text{and} \quad \frac{\omega_z}{\omega} = \left(\frac{1}{\nu^2\kappa}\right)^{1/3}. \tag{2.2}$$

Throughout the rest of this chapter the aforementioned units are used. The time dependent GPE takes the guise

$$i\frac{1}{2\pi}\frac{\omega_x}{\omega}\frac{\partial}{\partial t}\psi\left(\mathbf{r},t\right) = \hat{H}\psi\left(\mathbf{r},t\right), \tag{2.3}$$

with

$$\hat{H} = \left(-\frac{1}{2}\boldsymbol{\nabla}^2 + V_{\mathrm{T}}\left(\mathbf{r}\right) + G_N\left[\frac{1-\varepsilon_D}{2}\left|\psi\left(\mathbf{r},t\right)\right|^2 - \frac{3\varepsilon_D}{2}\frac{\partial^2\phi\left(\mathbf{r},t\right)}{\partial z^2}\right]\right). \tag{2.4}$$

The function $\phi(\mathbf{r},t)$ represents the long range component of the dipole-dipole interaction potential and is given by

$$\phi(\mathbf{r},t) = \frac{1}{4\pi}\int \mathrm{d}\mathbf{r}' \, \frac{|\psi(\mathbf{r}',t)|^2}{|\mathbf{r}-\mathbf{r}'|}. \tag{2.5}$$

Formally this is the same as a Coulomb potential generated by a charge distribution $|\psi(\mathbf{r}',t)|^2$. It is well known (see for example [79]) that such a potential function needs to satisfy the Poisson equation

$$-\boldsymbol{\nabla}^2\phi(\mathbf{r},t) = |\psi(\mathbf{r},t)|^2 . \tag{2.6}$$

The external trapping potential is given by a harmonic potential of the form

$$V_{\mathrm{T}}(\mathbf{r}) = \frac{1}{2}\left(\frac{\omega_x^2}{\omega^2}x^2 + \frac{\omega_y^2}{\omega^2}y^2 + \frac{\omega_z^2}{\omega^2}z^2\right). \tag{2.7}$$

Note, that V_{T} does not necessarily need to be a harmonic potential but can in general be arbitrary. Of course, the units chosen here might not be appropriate for a different kind of potential. However, as long as the potential displays a mainly harmonic character, the units presented above are still adequate. In this chapter a purely harmonic potential is assumed in order to discuss and test the numerical methods.

In order to perform numerical calculations the solution of the problem needs to be sought on an finite region of space $\mathbb{G} \subset \mathbb{R}^3$ with $\mathbb{G} = [x_1, x_2] \times [y_1, y_2] \times [z_1, z_2]$. In this finite region a numerical lattice with $n = n_x n_y n_z$ discrete lattice points is defined. The lattice point distance between two points in each spatial direction is $\Delta x = \frac{x_2 - x_1}{n_x}$, $\Delta y = \frac{y_2 - y_1}{n_y}$, and $\Delta z = \frac{z_2 - z_1}{n_z}$. With that a set of lattice points is defined by

$$\mathbf{R}_{a,b,c} = (x_1 + a\cdot\Delta x)\,\hat{\mathbf{e}}_x + (y_1 + b\cdot\Delta y)\,\hat{\mathbf{e}}_y + (z_1 + c\cdot\Delta z)\,\hat{\mathbf{e}}_z,$$

$$a \in \{0,1,\ldots n_x - 1\},\ b \in \{0,1,\ldots n_y - 1\},\ c \in \{0,1,\ldots n_z - 1\}.$$

Besides the discretization of space, also a discrete lattice for the time dimension is required. The time evolution is restricted to a finite interval $\mathbb{T} = [t_{\mathrm{init}}, t_{\mathrm{final}}] \subset \mathbb{R}$. Without loss if generality, the initial time coordinate can be set to $t_{\mathrm{init}} = 0$, so that $\mathbb{T} = [0, t_{\mathrm{final}}]$. This continuous interval is divided in $n_t + 1$ discrete lattice points. The separation between two points is given by $\Delta t = t_{\mathrm{final}}/n_t$. The set of lattice points reads

$$t_j = j\cdot\Delta t, \quad j \in \{0,1,\ldots,n_t\}.$$

On this lattice a discrete version of any continuous function $f(\mathbf{r},t)$ is defined via

$$f^j_{abc} \equiv f\left(\mathbf{R}_{a,b,c}, t_j\right).$$

In particular a discrete version of the wave function $\psi^j_{abc} \equiv \psi\left(\mathbf{R}_{a,b,c}, t_j\right)$ is defined on this lattice. In order to keep the amount of indices minimal, the following abbreviation is used:

$$\mathbf{f}^j \equiv \left(f^j_{0,0,0}, f^j_{1,0,0}, \ldots, f^j_{n_x-1,n_z-1,n_z-1}\right)^T.$$

$\mathbf{f}^j$ contains all n elements of f^j_{abc}. For the continuous version of the wave function the norm is defined over the infinite region $\mathbb{R}^3$ via

$$\left\|\psi\left(\mathbf{r},t\right)\right\|^2 \equiv \int\limits_{\mathbb{R}^3} \mathrm{d}\mathbf{r}\ \left|\psi\left(\mathbf{r},t\right)\right|^2.$$

For the discrete version, the integral needs to be replaced by a discrete sum over the finite region $\mathbb{G}$:

$$\left\|\boldsymbol{\psi}^j\right\|^2 \equiv \sum_{a=0}^{n_x-1}\sum_{b=0}^{n_y-1}\sum_{c=0}^{n_z-1}\left|\psi^j_{abc}\right|^2 \Delta x\Delta y\Delta z.$$

In order to calculate expectation values, it is necessary to find a discretization for the operators acting on the wave function. This is easily done for observables where the operator is simply a number, like in the case of the center-of-mass position:

$$\langle x\rangle \equiv \sum_{a=0}^{n_x-1}\sum_{b=0}^{n_y-1}\sum_{c=0}^{n_z-1} x_a\cdot\left|\psi^j_{abc}\right|^2\Delta x\Delta y\Delta z, \quad \text{with} \quad x_a = x_1 + a\cdot\Delta x. \tag{2.8}$$

In the same way the coordinates of the y- and z-component of the center-of-mass position are calculated. The situation becomes more difficult if the observable contains a differential operator. There is a number of different methods to calculate discrete spatial derivatives. The simplest, and probably most intuitive, is the method of finite differences [94]. While this method has the advantage that it requires only little computational effort, the problem is that it is not very accurate. Especially if high accuracy is demanded for long evolution times. Therefore a spectral method is more suited to the task. In the case of periodic boundary conditions a Fourier transformation needs to be used. In the continuous case the transformation is given by

$$\hat{f}\left(\mathbf{k}\right) = \frac{1}{\sqrt{2\pi}^3}\int\limits_{\mathbb{R}^3}\mathrm{d}\mathbf{r}\, f\left(\mathbf{r}\right)e^{-i\mathbf{k}\,\cdot\,\mathbf{r}},$$

and the inverse Fourier transformation reads

$$f(\mathbf{r}) = \frac{1}{\sqrt{2\pi}^3} \int_{\mathbb{R}^3} \mathrm{d}\mathbf{k}\, \hat{f}(\mathbf{k})\, e^{i\mathbf{k}\cdot\mathbf{r}}.$$

A derivative in position space becomes a simple multiplication in momentum space, as can be easily seen

$$\begin{aligned} \frac{\partial^n}{\partial x^n} f(\mathbf{r}) &= \frac{1}{\sqrt{2\pi}^3} \int_{\mathbb{R}^3} \mathrm{d}\mathbf{k}\, \hat{f}(\mathbf{k})\, \frac{\partial^n}{\partial x^n} e^{i\mathbf{k}\cdot\mathbf{r}} \\ &= \frac{1}{\sqrt{2\pi}^3} \int_{\mathbb{R}^3} \mathrm{d}\mathbf{k}\, \hat{f}(\mathbf{k})\, (ik_x)^n\, e^{i\mathbf{k}\cdot\mathbf{r}}, \quad n \in \mathbb{N}. \end{aligned}$$

So what needs to be done is to find the Fourier transform of $f(\mathbf{r})$, multiply it by $(ik_x)^n$ and then perform an inverse Fourier transformation of the function $\hat{f}(\mathbf{k})\,(ik_x)^n$. For a discrete lattice with periodic boundary conditions the discrete Fourier transformation needs to be used. To keep the notation better readable, only one dimensional functions are discussed in the following. The discrete Fourier transformation reads

$$\hat{f}_\alpha = \frac{1}{n_x} \sum_{a=-\frac{n_x}{2}}^{\frac{n_x}{2}-1} f_a e^{-i\alpha\frac{2\pi}{n_x}a}, \quad \alpha \in \left\{-\frac{n_x}{2}, -\frac{n_x}{2}+1, \ldots, \frac{n_x}{2}-1\right\}$$

and the inverse transformation is given by

$$f_a = \sum_{\alpha=-\frac{n_x}{2}}^{\frac{n_x}{2}-1} \hat{f}_\alpha e^{i\alpha\frac{2\pi}{n_x}a}, \quad a \in \left\{-\frac{n_x}{2}, -\frac{n_x}{2}+1, \ldots, \frac{n_x}{2}-1\right\}.$$

The extension to more dimensions is straightforward, each additional dimension adds one more sum to the formula. To distinguish the discrete derivative from the continuous, the notation δ_x^n is used instead of $\frac{\partial^n}{\partial x^n}$. So the discrete derivative is written as

$$\delta_x^n f_a \equiv \sum_{\alpha=-\frac{n_x}{2}}^{\frac{n_x}{2}-1} \left(i\frac{2\pi}{n_x \Delta x}\alpha\right)^n \left(\frac{1}{n_x} \sum_{a'=-\frac{n_x}{2}}^{\frac{n_x}{2}-1} f_{a'} e^{-i\alpha\frac{2\pi}{n_x}a'}\right) e^{i\alpha\frac{2\pi}{n_x}a},$$

$$a \in \left\{-\frac{n_x}{2}, -\frac{n_x}{2}+1, \ldots, \frac{n_x}{2}-1\right\}.$$

As is evident, the computational effort to calculate the spatial derivative for a set of n_x numbers scales with $\mathcal{O}(n_x^2)$. In the case of three spatial

dimensions this can become a significant factor. A more sophisticated method to calculate a discrete Fourier transformation is presented by the *Fast Fourier Transformation* (FFT) [94,95], where the computational effort scales with $\mathcal{O}(n_x \log_2 n_x)$. In all the numerical calculations presented in this work, the Fourier transformations were calculated using the FFT. An algorithm for the FFT is presented in Ref. [94]. In order for the algorithm to work, the number of lattice points needs to be an integer power of 2: $n_x = 2^k$, $n_y = 2^l$ and $n_z = 2^m$ with $k, l, m \in \mathbb{N}$.

In the following the discrete Laplace operator is denoted by

$$\boldsymbol{D}^{(s)} \equiv \delta_x^2 + \delta_y^2 + \delta_z^2, \tag{2.9}$$

where the superscript (s) indicates that this is a spectral operator. Note, that in Fourier space the discrete spectral Laplace operator reads

$$\widehat{\boldsymbol{D}^{(s)}} = -\left(\mathbf{k}_x^2 + \mathbf{k}_y^2 + \mathbf{k}_z^2\right), \tag{2.10}$$

where

$$k_{a,\alpha} = \frac{2\pi}{n_a \Delta a}\alpha, \quad \alpha \in \left\{-\frac{n_a}{2}, -\frac{n_a}{2}+1, \ldots, \frac{n_a}{2}-1\right\}, \quad \text{and } a \in \{x, y, z\}.$$

2.2 Determining the ground state of the BEC

Before the dynamical calculations can be performed, the ground state of the system needs to be determined. This is accomplished by finding the eigenfunction of the stationary GPE (1.4) with the lowest energy. In other words: Which function ψ_g, minimizes the energy functional (1.3)? A basic concept to accomplish this is given by the *imaginary time* method [96,97]. The idea is to propagate the time coordinate t along the imaginary axis, rather than the real axis. The time is given by $t = i\tau$, where τ is a real parameter which describes the propagation along the imaginary time axis. In order to illustrate this concept, consider the following SE

$$i\hbar \frac{\partial}{\partial t} |\psi(t)\rangle = \hat{H} |\psi(t)\rangle. \tag{2.11}$$

Applying the substitution $\tau = -it$, yields the transformed SE

$$\hbar \frac{\partial}{\partial \tau} |\psi(\tau)\rangle = -\hat{H} |\psi(\tau)\rangle. \tag{2.12}$$

Obviously, it is possible to define a time evolution operator (see for example [85])

$$\hat{\mathcal{U}}_t = e^{-i\frac{\hat{H}}{\hbar}t},$$

so that if an initial state $|\psi(t=0)\rangle$ is given at a time $t_0 = 0$, the state at time $t_1 = t$ is given by $|\psi(t)\rangle = \hat{\mathcal{U}}_t |\psi(t=0)\rangle$. That this is true can be easily verified by inserting $|\psi(t)\rangle$ in the SE (2.11). Similarly, the operator

$$\hat{\mathcal{U}}_\tau = e^{-\frac{\hat{H}}{\hbar}\tau}$$

can be defined. Having the initial state $|\psi(\tau=0)\rangle$, the propagated state $|\psi(\tau)\rangle$ is constructed via $|\psi(\tau)\rangle = \hat{\mathcal{U}}_\tau |\psi(\tau=0)\rangle$. Again, the conformation is easily obtained by inserting $|\psi(\tau)\rangle$ in the transformed SE (2.12). In contrast to the time evolution operator $\hat{\mathcal{U}}_t$, the operator $\hat{\mathcal{U}}_\tau$ is not unitary and does not conserve the norm. Say, $\hat{\mathcal{U}}_\tau$ is applied to an arbitrary state $|\psi\rangle$. Let $\{|\phi_n\rangle\}$ be the set of energy eigenstates with energies E_n of the Hamiltonian $\hat{H}$, so that one can write

$$\begin{aligned}
\hat{\mathcal{U}}_\tau |\psi\rangle &= e^{-\frac{\hat{H}}{\hbar}\tau} \sum_n |\phi_n\rangle \underbrace{\langle\phi_n|\psi\rangle}_{C_n} \\
&= \sum_n C_n e^{-\frac{\hat{H}}{\hbar}\tau} |\phi_n\rangle \\
&= \sum_n C_n e^{-\frac{E_n}{\hbar}\tau} |\phi_n\rangle .
\end{aligned}$$

Since the ground state has the lowest energy, the terms in this expansion, corresponding to excited states, are exponentially suppressed compared to the term corresponding to the ground state. The larger the parameter τ gets, the smaller get the terms of the excited states compared to the ground state. In principle, the ground state can be determined to arbitrary precision by applying $\hat{\mathcal{U}}_\tau$ for sufficiently large τ. Since the norm is not conserved, the resulting wave function needs to be normalized, and the ground state is found to be

$$|\psi_g\rangle = \lim_{\tau\to\infty} \frac{\hat{\mathcal{U}}_\tau |\psi\rangle}{\sqrt{\langle\psi| \hat{\mathcal{U}}_\tau^\dagger \hat{\mathcal{U}}_\tau |\psi\rangle}}.$$

The evolution of the system with the imaginary time parameter is similar to a diffusion process, where the system relaxes into its ground state. Therefore this process is referred to in the following as diffusion and $\hat{\mathcal{U}}_\tau$ as diffusion operator. In order to find a numerical approximation for the ground state, the diffusion needs to be discretized.

2.2.1 Normalized gradient flow

The diffusion equation for a BEC is found by substituting $t = -i\tau$ in the time dependent GPE (1.32). In order to determine the BEC ground

state, this diffusion equation needs to be solved. A method to achieve that was presented by Bao et al. [98–101]. In this section, the general principle of this method is discussed and the central equations necessary for the determination of the ground state are presented. Basically, the idea is to apply the method of the steepest decent to the energy functional (1.3). In order to satisfy the constraint of particle conservation the resulting wave function needs to be normalized after each time step. The result is the following *gradient flow with discrete normalization* (GFDN):

$$\begin{aligned} \frac{\partial}{\partial\tau}\psi(\mathbf{r},\tau) &= \left(\frac{\boldsymbol{\nabla}^2}{2} - V_{\mathrm{T}}(\mathbf{r})\right. \\ &\quad \left. -G_N\left[\frac{1-\varepsilon_D}{2}\left|\psi(\mathbf{r},\tau)\right|^2 - \frac{3\varepsilon_D}{2}\varphi(\mathbf{r},\tau)\right]\right)\psi(\mathbf{r},\tau), \end{aligned} \tag{2.13}$$

$$\varphi(\mathbf{r},\tau) = \frac{\partial^2\phi(\mathbf{r},\tau)}{\partial z^2}, \tag{2.14}$$

$$-\boldsymbol{\nabla}^2\phi(\mathbf{r},\tau) = \left|\psi(\mathbf{r},\tau)\right|^2, \quad \mathbf{r}\in\mathbb{G}, \quad \tau_j\le\tau\le\tau_{j+1}, \quad j\ge 1, \tag{2.15}$$

$$\psi(\mathbf{r},\tau_{j+1}) \equiv \psi\left(\mathbf{r},\tau_{j+1}^{+}\right) = \frac{\psi\left(\mathbf{r},\tau_{j+1}^{-}\right)}{\left\|\psi\left(\mathbf{r},\tau_{j+1}^{-}\right)\right\|}, \tag{2.16}$$

$$\psi(\mathbf{r},0) = \psi_0(\mathbf{r}),\ \mathbf{r}\in\mathbb{G}, \quad \text{with} \quad \left\|\psi_0(\mathbf{r})\right\|^2 = 1. \tag{2.17}$$

The right hand side of equation (2.13) is proportional to the negative gradient of the energy functional (1.3), which means that $\frac{\partial}{\partial\tau}\psi \propto -\frac{\delta E[\psi]}{\delta\psi}$. The change of the wave function ψ with the imaginary time parameter τ, follows the negative gradient of the energy functional $E[\psi]$. The gradient flow is described by equations (2.13)-(2.15). The normalization of the wave function after each time step is performed in (2.16). In order to save computation time, the initial wave function $\psi_0(\mathbf{r})$ should be chosen such that it represents already a fairly good approximation of the sought ground state. In the case of a BEC with a sufficiently large number of atoms (i.e. $G_N \gg 1$), the Thomas-Fermi approximation can be used. Using periodic boundary conditions

$$\psi^j_{abc} = \psi^j_{a+n_x,b,c} = \psi^j_{a,b+n_y,c} = \psi^j_{a,b,c+n_z},$$

the spectral discretization (2.9) for the spatial derivative is applicable. For the time discretization a backward Euler method, as was proposed by Bao et al. [100], is applied. The spatial and time discretization of the GFDN

reads:

$$\begin{aligned}
\frac{\boldsymbol{\psi}^* - \boldsymbol{\psi}^j}{\Delta\tau} &= \frac{\boldsymbol{\mathcal{D}}^{(s)}\boldsymbol{\psi}^*}{2} \\
&\quad - \left(\mathbf{V}_\mathrm{T} + G_N\left[\frac{1-\varepsilon_D}{2}\left|\boldsymbol{\psi}^j\right|^2 + \frac{3\varepsilon_D}{2}\boldsymbol{\varphi}^j\right]\right)\boldsymbol{\psi}^*, \quad (2.18)\\
\boldsymbol{\varphi}^j &= \delta_z^2\boldsymbol{\phi}^j, \quad (2.19)\\
-\boldsymbol{\mathcal{D}}^{(s)}\boldsymbol{\phi}^j &= \left|\boldsymbol{\psi}^j\right|^2, \quad (2.20)\\
\boldsymbol{\psi}^{j+1} &= \frac{\boldsymbol{\psi}^*}{\|\boldsymbol{\psi}^*\|}. \quad (2.21)
\end{aligned}$$

This set of equations needs to be solved in every time step j. The (not normalized) wave function $\boldsymbol{\psi}^*$ at the end of the time step is implicitly defined by (2.18). In order to obtain $\boldsymbol{\psi}^*$, an iteration process is applied. Bao et al. present an effective method to solve this implicit equation. They introduce a stabilization parameter α so that the equation reads

$$\frac{\boldsymbol{\psi}^{*,m+1} - \boldsymbol{\psi}^j}{\Delta\tau} = \frac{\boldsymbol{\mathcal{D}}^{(s)}\boldsymbol{\psi}^{*,m+1}}{2} - \alpha\boldsymbol{\psi}^{*,m+1} - \mathbf{A}_m^j,$$

with

$$\mathbf{A}_m^j = \left(\mathbf{V}_\mathrm{T} - \alpha + G_N\left[\frac{1-\varepsilon_D}{2}\left|\boldsymbol{\psi}^j\right|^2 + \frac{3\varepsilon_D}{2}\boldsymbol{\varphi}^j\right]\right)\boldsymbol{\psi}^{*,m},$$

where m is the index for the iteration step. A Fourier transformation of the whole equation yields

$$\frac{\widehat{\boldsymbol{\psi}^{*,m+1}} - \widehat{\boldsymbol{\psi}^j}}{\Delta\tau} = -\left(\alpha + \frac{\mathbf{k}^2}{2}\right)\widehat{\boldsymbol{\psi}^{*,m+1}} + \widehat{\mathbf{A}_m^j}.$$

The hat over the symbol denotes the Fourier transform of the respective quantity. In Fourier space, the Laplace operator $\boldsymbol{\mathcal{D}}^{(s)}$ becomes $\widehat{\boldsymbol{\mathcal{D}}^{(s)}} = -\mathbf{k}^2 = -\left(\mathbf{k}_x^2 + \mathbf{k}_y^2 + \mathbf{k}_z^2\right)$, see (2.10). This equation is now easily solved for $\widehat{\boldsymbol{\psi}^{*,m+1}}$, which reads

$$\widehat{\boldsymbol{\psi}^{*,m+1}} = \frac{2\left(\widehat{\boldsymbol{\psi}^j} + \Delta\tau\cdot\widehat{\mathbf{A}_m^j}\right)}{\left[2 + \Delta\tau\left(2\alpha + \mathbf{k}^2\right)\right]}.$$

Applying a second Fourier transformation to $\widehat{\boldsymbol{\psi}^{*,m+1}}$ yields the result for the particular iteration step. The iteration is stopped when $\boldsymbol{\psi}^{*,m+1}$ and $\boldsymbol{\psi}^{*,m}$ differ only by a small amount, a suitable criterion is

$$\left\| \boldsymbol{\psi}^{*,m+1} - \boldsymbol{\psi}^{*,m} \right\| < \varepsilon. \tag{2.22}$$

Bao et al. also show that there is an optimal value for α, so that the iteration converges as fast as possible. It turns out to be

$$\alpha_{\text{opt}} = \frac{1}{2} \left(b_{\max} + b_{\min} \right),$$

with

$$\begin{aligned} b_{\max} &= \max_{abc} \left(\mathbf{V}_{\text{T}} + G_N \left[\frac{1-\varepsilon_D}{2} \left| \boldsymbol{\psi}^j \right|^2 + \frac{3\varepsilon_D}{2} \boldsymbol{\varphi}^j \right] \right), \\ b_{\min} &= \min_{abc} \left(\mathbf{V}_{\text{T}} + G_N \left[\frac{1-\varepsilon_D}{2} \left| \boldsymbol{\psi}^j \right|^2 + \frac{3\varepsilon_D}{2} \boldsymbol{\varphi}^j \right] \right). \end{aligned}$$

The GFDN with backward Euler time discretization is unconditionally stable for all time step sizes. Note, the iteration needs not necessarily be done until it converges. For example one can make only one iteration step, i.e. $m = 1$, which is equivalent to the so-called backward/forward Euler time discretization. While this reduces the number of iterations, it sets limits on the size of the time step $\Delta\tau$. This is also discussed in Refs. [98, 99, 101], where the limit of the time step size is shown to be $\Delta\tau < \alpha_{\text{opt}}$ for the case $\alpha = \alpha_{\text{opt}}$. For a more detailed discussion of this method see Ref. [98] for the case of a non-dipolar BEC and Ref. [100] for a dipolar BEC. An overview of a number of different numerical methods to solve the GPE are presented in Ref. [101].

In every time step the Poisson equation (2.20) needs to be solved in order to calculate the long range component of the dipole-dipole interaction. Again, the discrete Fourier transformation is used for this task. The transformed equation is easily solved for the potential function $\boldsymbol{\phi}^j$ at the given time step j. The result reads

$$\widehat{\boldsymbol{\phi}^j} = \frac{\widehat{\left| \boldsymbol{\psi}^j \right|^2}}{\mathbf{k}_x^2 + \mathbf{k}_y^2 + \mathbf{k}_z^2}.$$

A divergence occurs when the denominator on the right hand side becomes zero, which is the case for $a = \frac{n_x}{2}$, $b = \frac{n_y}{2}$, and $c = \frac{n_z}{2}$. What is actually

needed for the long range part of the dipole-dipole interaction potential is the second spatial derivative of $\boldsymbol{\phi}^j$. In Fourier space it reads

$$-\mathbf{k}_z^2 \widehat{\boldsymbol{\phi}^j} = -\frac{\mathbf{k}_z^2 \widehat{\left|\boldsymbol{\psi}^j\right|^2}}{\mathbf{k}_x^2 + \mathbf{k}_y^2 + \mathbf{k}_z^2}.$$

To avoid the divergence, the right hand side is simply set to $-\widehat{|\psi^j|^2}$ at the point where the divergence occurs. An alternative method would be to use fixed boundary conditions instead of periodic boundary conditions and thereby to replace the complex Fourier transform by a real discrete sine transform. This approach, as it was proposed by Bao et al. in [100], avoids the occurrence of a divergence.

An inverse Fourier transform of $-\mathbf{k}_z^2 \widehat{\boldsymbol{\phi}^j}$ yields the sought data $\boldsymbol{\varphi}^j = \delta_z^2 \boldsymbol{\phi}^j$. Note, that this does not need to be done in every iteration step m, due to the backward Euler time discretization that was chosen in (2.18). The last task that is left to do in order to finalize the time step, is to normalize the wave function $\boldsymbol{\psi}^*$, which yields the wave function $\boldsymbol{\psi}^{j+1}$ at the time step $j+1$. The diffusion process can be stopped when an additional time step does not significantly change the wave function. Again, this is checked by the criterion

$$\left\| \boldsymbol{\psi}^{j+1} - \boldsymbol{\psi}^j \right\| < \varepsilon. \tag{2.23}$$

The threshold ε is set to be machine precision, i.e. $\varepsilon = 10^{-15}$, so that the determined ground state is as precise as possible. The necessity of this precision is discussed later in this chapter in the context of the time evolution of the BEC.

2.2.2 Ground state in a harmonic trap

For the examples in this section exclusively harmonic external potentials are used. The results for harmonic potentials are well known, which allows to test the numerical results. For $G_N = \varepsilon_D = 0$ the GPE reduces to the linear SE. The ground state density distribution takes a Gaussian shape

$$|\psi_{\mathrm{HO}}(\mathbf{r})|^2 = \pi^{-3/4} \exp\left[-\left(\frac{\omega_x}{\omega} x^2 + \frac{\omega_y}{\omega} y^2 + \frac{\omega_z}{\omega} z^2 \right) \right]. \tag{2.24}$$

For very large G_N the TF approximation is applicable, which yields

$$|\psi_{\mathrm{TF}}(\mathbf{r})|^2 = \frac{15}{8\pi} \frac{1}{\lambda_x \lambda_y \lambda_z} \left(1 - \frac{x^2}{\lambda_x^2} - \frac{y^2}{\lambda_y^2} - \frac{z^2}{\lambda_z^2} \right). \tag{2.25}$$

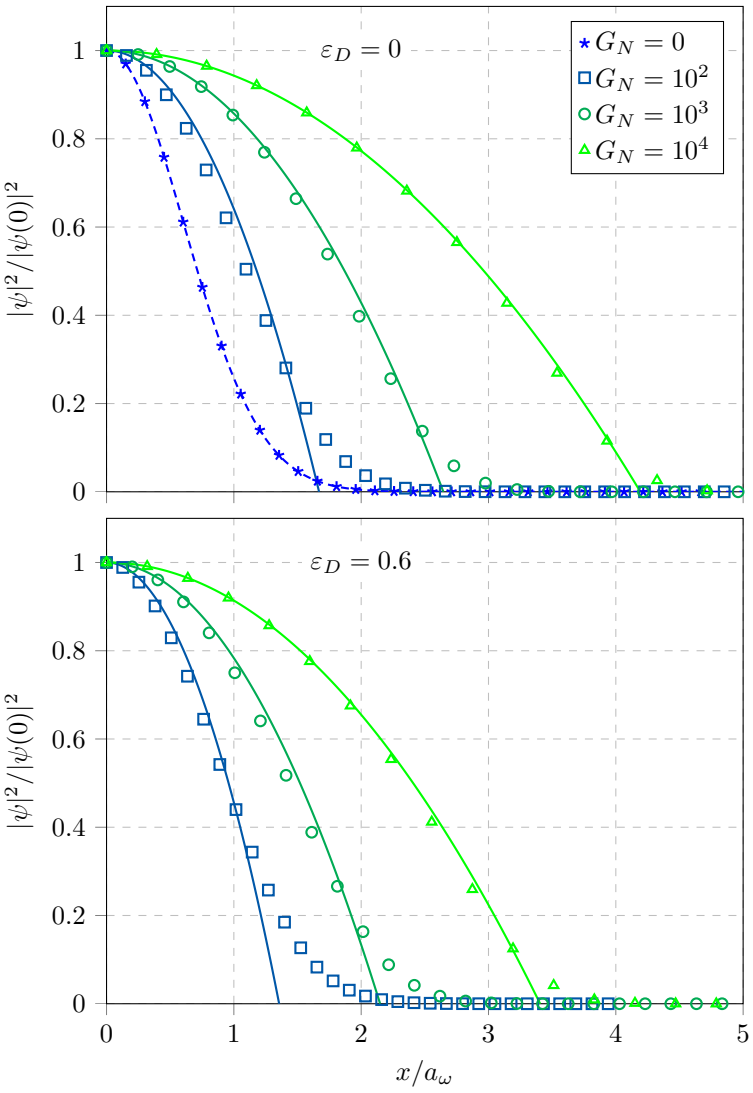

Figure 2.1: Depicted are cuts of $|\psi(\mathbf{r})|^2$ along the line $y = z = 0$ for various interaction strengths G_N. The top panel shows the results for $\varepsilon_D = 0$ and the bottom panel for $\varepsilon_D = 0.6$. The cuts are only presented for $x \geq 0$ since the wave functions are symmetric. The data points show the results from the numerical solution of the stationary GPE. The dashed line shows Gaussian density (2.24) and the solid lines the TF density distribution (2.25). The density distribution is divided by its central value $|\psi(0)|^2$, which is why all curves start at 1. *Parameters*: trap aspect ratios: $\nu = 2$ and $\kappa = 0.8$, diffusion time step size $\Delta\tau = 10^{-3}$, size of numerical lattice: $64 \times 64 \times 64$, expansion of the lattice: $6\lambda_x \times 6\lambda_y \times 6\lambda_z$.

In order to get the atom density distribution $n(\mathbf{r})$, these expressions need to be multiplied by the number of atoms N.

Fig. 2.1 compares these analytical results to the numerical results for different values of G_N and ε_D. Depicted are cuts of the density distribution along the line $y = z = 0$. To allow an easier comparison, the results are all normalized to their central value. For $G_N = 0$ the Gaussian density distribution is exactly reproduced. As G_N increases, the density approaches the TF approximation. Furthermore, it becomes evident that the TF approximation reproduces the density best in the central regions of the BEC and fails at the edges. As G_N becomes larger, the region where the TF approximation fails becomes smaller. For $\varepsilon_D = 0.6$ the size of the BEC is modified. Since the dipoles are oriented in the z-direction, the BEC becomes more elongated in that direction and contracts in the x- and y-direction for larger ε_D.

Besides the shape of the ground state, the energy is also an interesting quantity to compare. The energy is in fact the energy per particle $\epsilon = E/N$. For the case $G_N = \varepsilon_D = 0$, it is well known that the ground state energy is the harmonic oscillator energy

$$\epsilon_{\mathrm{HO}} = \frac{1}{2}\left(\frac{\omega_x}{\omega} + \frac{\omega_y}{\omega} + \frac{\omega_z}{\omega}\right). \tag{2.26}$$

Within the TF approximation, the chemical potential for the case $\varepsilon_D = 0$ is given by

$$\mu^{(0)} = \frac{1}{2}\left(\frac{15}{8\pi}G_N\right)^{2/5}.$$

Since $\mu \propto N^{2/5}$ and $\mu = \frac{\partial E}{\partial N}$ it is immediately clear that

$$\epsilon_{\mathrm{TF}}^{(0)} = \frac{5}{7}\mu^{(0)} = \frac{5}{14}\left(\frac{15}{8\pi}G_N\right)^{2/5} \approx 0.41 \cdot G_N^{2/5}. \tag{2.27}$$

In Ref. [59] an expression for ϵ is derived based on a variational calculation with an Gaussian trial wave function. The result reads

$$\epsilon_{\mathrm{Gauss}} = \frac{5}{4}\left(\frac{2}{\pi}\right)^{1/5}\left(\frac{1}{8\pi}G_N\right)^{2/5} \approx 0.44 \cdot G_N^{2/5}. \tag{2.28}$$

Similar to the TF approximation, this result was derived under the assumption that the number of particles is large enough so that the kinetic energy term can be neglected. One would expect that for small values of G_N the energy is close to ϵ_{HO}. As G_N increases, the kinetic energy term becomes more and more insignificant. As was presented in Fig. 2.1, the actual shape of the wave function lays between a Gaussian wave function

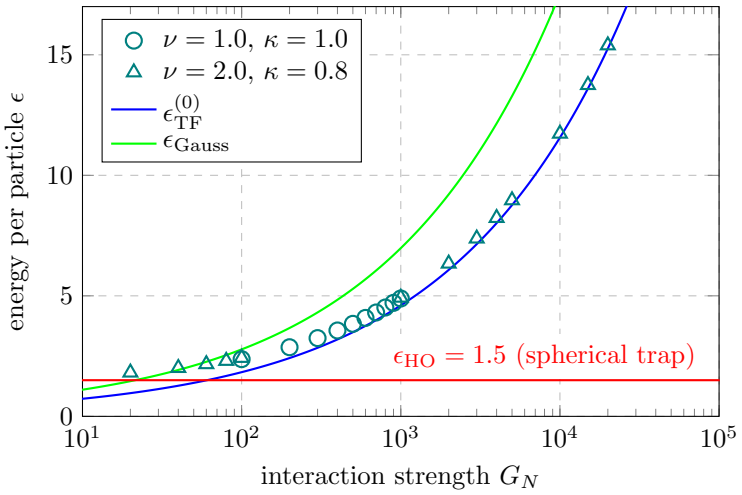

Figure 2.2: Energy per particle $\epsilon = E/N$ vs. interaction strength $G_N = 8\pi\frac{Na_s}{a_\omega}$. The green line shows $\epsilon_{\mathrm{Gauss}}$, the blue line the TF result $\epsilon^{(0)}_{\mathrm{TF}}$. In both cases the kinetic energy was neglected. The harmonic oscillator energy ϵ_{HO} in a spherical trap is marked by a red line. The data points show the results from the numerical calculation. *Parameters*: trap aspect ratios: $\nu = \kappa = 1$ (circles), $\nu = 2$ and $\kappa = 0.8$ (triangles), dipole-dipole interaction strength $\varepsilon_D = 0$, diffusion time step size $\Delta\tau = 10^{-3}$, size of numerical lattice: $64 \times 64 \times 64$, expansion of the lattice: $6\lambda_x \times 6\lambda_y \times 6\lambda_z$.

and a TF ellipsoid. Thus the energy should also lay between $\epsilon_{\mathrm{Gauss}}$ and $\epsilon^{(0)}_{\mathrm{TF}}$. Since for increasing G_N the wave function approaches the TF ellipsoid, the energy approaches $\epsilon^{(0)}_{\mathrm{TF}}$. In Fig. 2.2 the numerical results of the energy are compared to the analytical approximations. As expected the energy ϵ is between $\epsilon_{\mathrm{Gauss}}$ and $\epsilon^{(0)}_{\mathrm{TF}}$ and approaches for large G_N the curve for $\epsilon^{(0)}_{\mathrm{TF}}$.

From the density distribution of the BEC, presented in Fig. 2.1, as well as from the energy presented in Fig. 2.2, one can see that from roughly $G_N = 1000$ the TF approximation yields useful results.

2.3 Time dependent GPE

For the time evolution of the BEC, the time dependent GPE is solved by a discretization of the time evolution operator. The discussion presented in this chapter is limited to the case of static harmonic potentials. However, the presented method is also applicable to other external potentials. In particular, the potential generated by the mirror BEC is incorporated in

the next chapter. Contrary to the method discussed for the stationary case, the method for the dynamical case is an explicit method and does not require an iteration in order to self consistently determine the resulting wave function. This saves a lot of computational time and, as it turns out, the time evolution is still precise enough for the intended purpose. Using periodic boundary conditions, the spatial derivatives, as well as the Poisson equation for the dipole-dipole interaction are again evaluated with Fourier transformations. The essence of the following method is the splitting of the time evolution operator into different parts. In particular, it is split into a part which contains the kinetic term of the Hamiltonian and one part which contains the rest.

2.3.1 Operator splitting

The time evolution operator, which propagates the wave function from a time t_0 to a time $t_0 + \Delta t$, can be written in general as an operator of the form $e^{\hat{A}\Delta t}$. The idea of operator splitting is to write this operator in the form $e^{\hat{B}\Delta t}e^{\hat{C}\Delta t}$, with $\hat{A} = \hat{B} + \hat{C}$. In case that the commutator of those two operators vanishes, $\left[\hat{B}, \hat{C}\right] = 0$, the splitting simply reads $e^{\hat{A}\Delta t} = e^{\hat{B}\Delta t}e^{\hat{C}\Delta t}$. In the case of the time evolution operator, $\hat{B} + \hat{C}$ is mainly given by the Hamiltonian of the system, and in general the terms constituting the Hamiltonian do not commute. The error ε that is made by replacing the time evolution operator by the splitting operator is given by

$$\varepsilon = e^{\hat{A}\Delta t} - e^{\hat{B}\Delta t}e^{\hat{C}\Delta t} = \frac{1}{2}\left[\hat{C}, \hat{B}\right]\Delta t^2 + \mathcal{O}\left(\Delta t^3\right).$$

This result is easily verified by making use of the exponential power series. This shows that this sequential splitting is correct up to linear order in Δt and is actually exact for the case that $\hat{B}$ and $\hat{C}$ commute. This approximation can be improved with different splitting schemes. The splitting scheme used in this work is the Strang splitting [102], it reads

$$e^{\hat{A}\Delta t} = e^{\frac{1}{2}\hat{B}\Delta t}e^{\hat{C}\Delta t}e^{\frac{1}{2}\hat{B}\Delta t} + \varepsilon,$$

with

$$\varepsilon = \frac{1}{24}\left(\left[\hat{B}, \left[\hat{B}, \hat{C}\right]\right] - 2\left[\hat{C}, \left[\hat{C}, \hat{B}\right]\right]\right)\Delta t^3 + \mathcal{O}\left(\Delta t^4\right).$$

This means that the Strang splitting is correct up to second order in Δt.

2.3.2 Time splitting spectral method

In order to adopt the Strang splitting scheme for the time evolution of the BEC, the Hamiltonian is split into two parts:

$$\hat{H} = \hat{K} + \hat{V}.$$

The operator $\hat{K}$ represents the kinetic energy term and $\hat{V}$ the rest consisting of the external potential and the interaction potential. A single time step of length Δt is performed with either $e^{-\frac{i}{2}\frac{\hat{V}}{\hbar}\Delta t}e^{-i\frac{\hat{K}}{\hbar}\Delta t}e^{-\frac{i}{2}\frac{\hat{V}}{\hbar}\Delta t}$ or $e^{-\frac{i}{2}\frac{\hat{K}}{\hbar}\Delta t}e^{-i\frac{\hat{V}}{\hbar}\Delta t}e^{-\frac{i}{2}\frac{\hat{K}}{\hbar}\Delta t}$. In principle both schemes are equivalent. In the following both Versions of the splitting are discussed. It is important to note that the application of $e^{-i\frac{\hat{V}}{\hbar}\Delta t}$ on a wave function ψ does not change the modulus squared of the wave function. Applying the operator $e^{-i\frac{\hat{V}}{\hbar}\Delta t}$ to ψ is equivalent to solving

$$i\hbar\frac{\partial}{\partial t}\psi = \hat{V}\psi.$$

Since the operator $\hat{V}$ simply multiplies the real value V to ψ, the complex conjugate of the equation reads

$$-i\hbar\frac{\partial}{\partial t}\psi^* = V\psi^*.$$

The time derivative of $|\psi|^2$ based on those two differential equations, is found to be

$$\begin{aligned}\frac{\partial}{\partial t}|\psi|^2 &= \psi\frac{\partial\psi^*}{\partial t} + \psi^*\frac{\partial\psi}{\partial t} \\ &= \frac{i}{\hbar}V\left(\psi\psi^* - \psi^*\psi\right) = 0.\end{aligned}$$

Since $|\psi|^2$ remains constant during this part of the time step, expectation values, like for example the center of mass, remain constant as well. This becomes an important point later on. As was already mentioned, applying $\hat{V}$ to ψ corresponds to a simple multiplication in position space. This means that also the operator $e^{-i\frac{\hat{V}}{\hbar}\Delta t}$ is applied by simply multiplying $e^{-i\frac{V}{\hbar}\Delta t}$ to ψ. The value of V depends in the case that $G_N \neq 0$ on $|\psi|^2$ and for $\varepsilon_D \neq 0$ it also involves the solution of a Poisson equation. However, since $|\psi|^2$ is constant during this operation, it is not necessary to do any self consistent calculation. In order to compute the part of the time step which involves the kinetic energy term $\hat{K}$, a Fourier Transformation is employed. Therefore this method is referred to as *time splitting spectral method* (TSSP).

The approach for a single time step is the following:

$$\begin{aligned}
\widehat{\boldsymbol{\psi}_1^j} &= \exp\left\{-i\frac{\Delta t}{2}\left(\mathbf{k}_x^2+\mathbf{k}_y^2+\mathbf{k}_z^2\right)\right\}\cdot\widehat{\boldsymbol{\psi}^j},\\
\widehat{\boldsymbol{\varphi}_1^j} &= -\frac{\mathbf{k}_z^2\widehat{\left|\boldsymbol{\psi}_1^j\right|^2}}{\mathbf{k}_x^2+\mathbf{k}_y^2+\mathbf{k}_z^2},\quad \widehat{\varphi_1^j}=-\widehat{\left|\psi_1^j\right|^2}\quad\text{for}\quad k_x=k_y=k_z=0,\\
\boldsymbol{\psi}_2^j &= \exp\left\{-i\Delta t\left[\mathbf{V}_T+G_N\left(\frac{1-\varepsilon_D}{2}\left|\boldsymbol{\psi}_1^j\right|^2+\frac{3\varepsilon_D}{2}\boldsymbol{\varphi}_1^j\right)\right]\right\}\cdot\boldsymbol{\psi}_1^j,\\
\widehat{\boldsymbol{\psi}^{j+1}} &= \exp\left\{-i\frac{\Delta t}{2}\left(\mathbf{k}_x^2+\mathbf{k}_y^2+\mathbf{k}_z^2\right)\right\}\cdot\widehat{\boldsymbol{\psi}_2^j},
\end{aligned}$$

where the hats indicate the Fourier transform of the respective quantity. In order to calculate this time step, six Fourier transformations are required: $\boldsymbol{\psi}^j\to\widehat{\boldsymbol{\psi}^j}$, $\widehat{\boldsymbol{\psi}_1^j}\to\boldsymbol{\psi}_1^j$, $\left|\boldsymbol{\psi}_1^j\right|^2\to\widehat{\left|\boldsymbol{\psi}_1^j\right|^2}$, $\widehat{\boldsymbol{\varphi}_1^j}\to\boldsymbol{\varphi}_1^j$, $\boldsymbol{\psi}_2^j\to\widehat{\boldsymbol{\psi}_2^j}$, and $\widehat{\boldsymbol{\psi}^{j+1}}\to\boldsymbol{\psi}^{j+1}$. It seems that for consecutive time steps, the last and first Fourier transformation can be omitted. However, if one is interested in some expectation values after the time step, the transformation of the wave function back to position space is necessary. Consider the following scheme:

$$\begin{aligned}
\widehat{\boldsymbol{\varphi}^j} &= -\frac{\mathbf{k}_z^2\widehat{\left|\boldsymbol{\psi}^j\right|^2}}{\mathbf{k}_x^2+\mathbf{k}_y^2+\mathbf{k}_z^2},\quad \widehat{\varphi^j}=0\quad\text{for}\quad k_x=k_y=k_z=0,\\
\boldsymbol{\psi}_1^j &= \exp\left\{-i\frac{\Delta t}{2}\left[\mathbf{V}_T+G_N\left(\frac{1-\varepsilon_D}{2}\left|\boldsymbol{\psi}^j\right|^2+\frac{3\varepsilon_D}{2}\boldsymbol{\varphi}^j\right)\right]\right\}\cdot\boldsymbol{\psi}^j,\\
\widehat{\boldsymbol{\psi}_2^j} &= \exp\left\{-i\Delta t\left(\mathbf{k}_x^2+\mathbf{k}_y^2+\mathbf{k}_z^2\right)\right\}\cdot\widehat{\boldsymbol{\psi}_1^j},\\
\widehat{\boldsymbol{\varphi}_2^j} &= -\frac{\mathbf{k}_z^2\widehat{\left|\boldsymbol{\psi}_2^j\right|^2}}{\mathbf{k}_x^2+\mathbf{k}_y^2+\mathbf{k}_z^2},\quad \widehat{\varphi_2^j}=-\widehat{\left|\psi_2^j\right|^2}\quad\text{for}\quad k_x=k_y=k_z=0,\\
\boldsymbol{\psi}^{j+1} &= \exp\left\{-i\frac{\Delta t}{2}\left[\mathbf{V}_T+G_N\left(\frac{1-\varepsilon_D}{2}\left|\boldsymbol{\psi}_2^j\right|^2+\frac{3\varepsilon_D}{2}\boldsymbol{\varphi}_2^j\right)\right]\right\}\cdot\boldsymbol{\psi}_2^j.
\end{aligned}$$

In order to complete the time step using this scheme, also six Fourier transformations are needed: $\left|\boldsymbol{\psi}^j\right|^2\to\widehat{\left|\boldsymbol{\psi}^j\right|^2}$, $\widehat{\boldsymbol{\varphi}^j}\to\boldsymbol{\varphi}^j$, $\boldsymbol{\psi}_1^j\to\widehat{\boldsymbol{\psi}_1^j}$, $\widehat{\boldsymbol{\psi}_2^j}\to\boldsymbol{\psi}_2^j$, $\left|\boldsymbol{\psi}_2^j\right|^2\to\widehat{\left|\boldsymbol{\psi}_2^j\right|^2}$, and $\widehat{\boldsymbol{\varphi}_2^j}\to\boldsymbol{\varphi}_2^j$. The computational effort for both schemes

is identical. Again it seems, that by a combination of subsequent time steps the first and last Fourier transformation can be omitted. And indeed, using the latter scheme it is possible. Since the application of $e^{-\frac{i}{2}\frac{\hat{V}}{\hbar}\Delta t}$ does not change the expectation values, they can be calculated with respect to the wave function $\boldsymbol{\psi}_2^j$, rather than with respect to the wave function $\boldsymbol{\psi}^{j+1}$. In fact the knowledge of $\boldsymbol{\psi}^{j+1}$ is not needed at all. The time evolution scheme is the following: First the operator $e^{-\frac{i}{2}\frac{\hat{V}}{\hbar}\Delta t}$ is applied, then the operator $e^{-i\frac{\hat{K}}{\hbar}\Delta t}$. Then the expectation values are calculated. What follows is a sequence of $e^{-i\frac{\hat{V}}{\hbar}\Delta t}$ and $e^{-i\frac{\hat{K}}{\hbar}\Delta t}$ for every time step. In order to obtain the final wave function, in the last step the operator $e^{-\frac{i}{2}\frac{\hat{V}}{\hbar}\Delta t}$ is applied. Excluding the first and last time step, the number of necessary Fourier transformations per time step has reduced from six to four.

Note, the described method can also be applied using the previous splitting scheme. However, the resulting time series is shifted by $\Delta t/2$. Therefore, the latter scheme is preferable.

2.3.3 Time evolution in a harmonic potential

To conclude this chapter, the time evolution of a BEC in a harmonic trap is presented. The approach is the following: first the ground state is determined in a harmonic trap, then the harmonic trap minimum is shifted by x_s in the x-direction. The time evolution is calculated in the shifted potential.

The center of mass is expected to perform harmonic oscillations with period $T = 1$. That this is actually the case is presented in Fig. 2.3. The x-coordinate of the center-of-mass $\langle x \rangle$ is presented as a function of time. The first ten periods of the time evolution are shown. Ideally, the norm should be conserved during the time evolution. Due to numerical error this is not the case. The deviation of the wave function norm is measured by $L = \left\|\boldsymbol{\psi}^j\right\| - \left\|\boldsymbol{\psi}^0\right\|$. The longer the time evolution, the greater the error gets. The longest time evolutions presented in this work are up to 10^4 oscillation periods. In this case the error L is of the order 10^{-9}.

In a purely harmonic potential the center of mass oscillates in the harmonic trap while the shape of the BEC remains unaffected. However, this is only the case if the initial wave function is the exact (shifted) ground state. As a measure for the shape oscillations of the BEC, the width

$$\sigma_a = \sqrt{\left\langle (a - \langle a \rangle)^2 \right\rangle},\ a \in \{x, y, z\}$$

of the wave function is an appropriate quantity. Fig. 2.4 shows the relative

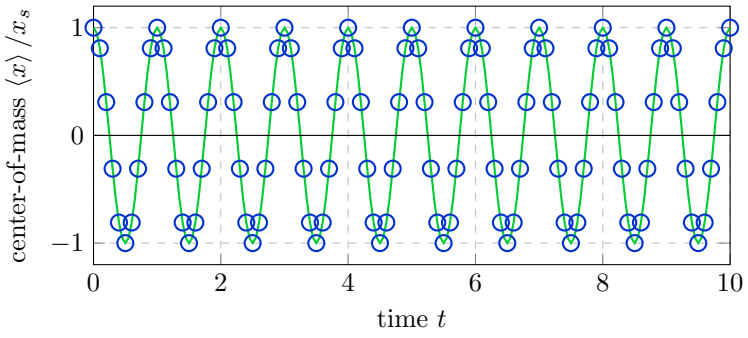

Figure 2.3: Center-of-mass $\langle x \rangle$ vs. time t. The blue circles show the results of the numerical calculation, the green line shows $\cos(2\pi t)$. The energy was conserved within an accuracy of 10^{-8} and the norm within 10^{-12}. *Parameters*: trap aspect ratios: $\nu = \kappa = 1$, dipole-dipole interaction strength $\varepsilon_D = 0$, contact interaction strength $G_N = 1000$, diffusion time step size $\Delta\tau = 10^{-3}$, accuracy threshold $\varepsilon = 10^{-15}$, time step size $\Delta t = 10^{-3}$, potential shift $x_s = 0.3$, size of numerical lattice: $64 \times 64 \times 64$, expansion of the lattice: $6\lambda_x \times 6\lambda_y \times 6\lambda_z$.

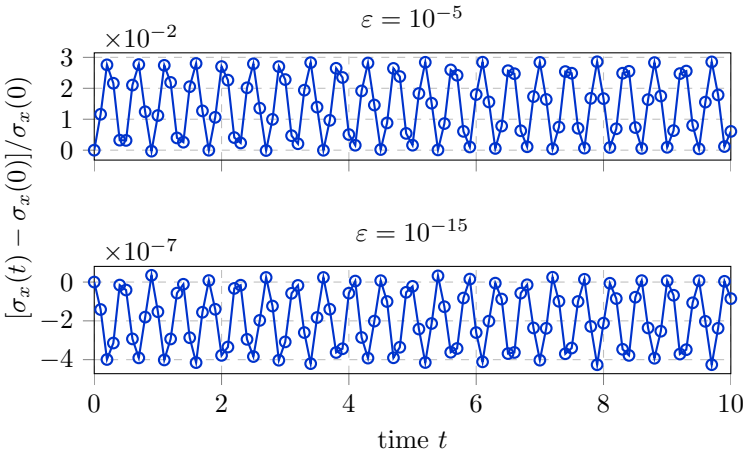

Figure 2.4: Relative fluctuation of the BEC width $\frac{\sigma_x(t)-\sigma_x(0)}{\sigma_x(0)}$ vs. time t. The top panel shows the time evolution based on a ground state determined with accuracy threshold $\varepsilon = 10^{-5}$ and the bottom panel with $\varepsilon = 10^{-15}$. *Parameters*: same as in Fig. 2.3

fluctuations $[\sigma_a(t) - \sigma_a(0)]/\sigma_a(0)$ of the width as a function of time. As it turns out, it is very important to determine the ground state with high accuracy in order to reduce the shape fluctuations. To demonstrate this, in Fig. 2.4 two different results for the shape fluctuations are presented. In one example the threshold (2.23) for the ground state accuracy was set to $\varepsilon = 10^{-5}$ in the other the threshold was set to 10^{-15}. One can see that this reduces the fluctuations of σ_a by several orders of magnitude. In Chapter 5 this high accuracy becomes important since the fluctuations of σ_a due to anharmonic terms in the potential are investigated. Therefore it is necessary that the fluctuations due to numerical errors are orders of magnitude smaller then the fluctuations due to the anharmonic terms.

2.4 Other numerical methods

The discussion presented here is restricted to two numerical methods, the GFDN for the determination of the ground state and the TSSP for the time evolution of the BEC. The GFDN with backward euler time discretization and spectral spatial accuracy is suited for tasks where the ground state needs to be determined with high accuracy [101], as is the case in the present work. The TSSP is an explicit method, which provides a time evolution with sufficient accuracy while the computation effort is relatively small, especially compared to implicit methods like for example the Crank-Nicolson (CN) method, which is also a popular method in this field [103, 104]. The CN requires the solution of a non-linear system of equations in every time step, thus it requires a rather high computational effort. There are a number of different numerical methods to solve a non-linear SE, a comparison of some popular methods is presented in Ref. [105], where also the advantages and disadvantages of each method are discussed.

Chapter 3

Modeling the system

In this chapter a model is presented which describes a dipolar BEC in close proximity to a superconductor. The GPE for a dipolar BEC close to a superconducting surface is derived by a variation of the energy functional. The superconductor is assumed to be an infinite half-space, which allows to calculate the surface potential with the method of magnetic mirror dipoles.

Two different methods for the calculation of the potential, generated by the mirror BEC, are presented. For the first method the mirror BEC is assumed to be a three dimensional TF ellipsoid. The second method relies on a simplified version of the TF density distribution, where the three dimensional ellipsoid is approximated by an one dimensional density distribution.

3.1 The GPE of a dipolar BEC close to the surface of a superconductor

The first task is to find the appropriate GPE for the system under consideration. The following derivation of the GPE is also presented in Ref. [56]. A starting point for this is the Hamiltonian for the atoms in the BEC. In general it can be written as

$$\hat{H} = \hat{H}_0 + \hat{H}_{\mathrm{mir}}, \tag{3.1}$$

where $\hat{H}_0$ is the Hamiltonian for the system without the surface interaction

$$\hat{H}_0 = \sum_{i=1}^{N} \left[\frac{\mathbf{p}_i^2}{2m} + V_{\mathrm{T}}\left(\mathbf{r}_i\right) \right] + \frac{1}{2} \sum_{i=1}^{N} \sum_{j \neq i}^{N} U\left(\mathbf{r}_i, \mathbf{r}_j\right), \tag{3.2}$$

and $\hat{H}_{\mathrm{mir}}$ describes the interaction with the mirror atoms

$$\hat{H}_{\mathrm{mir}} = \sum_{i=1}^{N} \sum_{k=1}^{N} U_{\mathrm{md}} \left(\mathbf{r}_i, \mathbf{r}'_k \right). \tag{3.3}$$

In H_{mir} it is necessary to sum the interaction between all the atoms in the BEC, denoted by the index i, with all the atoms in the mirror BEC, denoted by the index k. In contrast to the interaction between the atoms in the BEC, here the restriction $i \neq k$ is not needed. The reason is of course that an atom also interacts with its own mirror atom. Furthermore, the factor of $\frac{1}{2}$ is unnecessary. Every atom interacts with every mirror atom, which gives a total of N^2 interaction terms.

Next, the energy functional $E = \langle \Psi_{\mathrm{H}} | \hat{H} | \Psi_{\mathrm{H}} \rangle$ needs to be minimized under the constraint that the number of particles is fixed, which means that the norm of the wave function must be fixed. The result for the case $\hat{H}_{\mathrm{mir}} = 0$ was already presented in Section 1.2. This was done by using the standard Hartree ansatz (1.2) for the many body wave function. In the following a similar approach is used. However, instead of (1.2), the appropriate ansatz here is the Hartree ansatz for a mixture consisting of two different kinds of bosons

$$\Phi_{\mathrm{H}} \equiv \Phi_{\mathrm{H}} \left(\mathbf{r}_1, \ldots, \mathbf{r}_N; \mathbf{r}'_1, \ldots, \mathbf{r}'_N \right) = \prod_{i=1}^{N} \psi \left(\mathbf{r}_i \right) \prod_{k=1}^{N} \chi \left(\mathbf{r}'_k \right). \tag{3.4}$$

The first kind of bosons are the original atoms in the BEC. Their single body wave function is denoted by ψ. The other kind of bosons are the mirror atoms, their single body wave function is χ. Of course, the mirror atoms are not real particles, but merely a way to emulate the effect of the eddy currents in the superconducting surface. In the same way χ is not an actual physical wave function. However, this description is valid as long as the ψ and χ remain separate and have no significant overlap. Any interference effects between ψ and χ would be unrealistic. The single body wave functions are as usual normalized to unity

$$\int \mathrm{d}\mathbf{r}_i \; |\psi \left(\mathbf{r}_i \right)|^2 = 1, \quad \text{and} \quad \int \mathrm{d}\mathbf{r}'_k \; |\psi \left(\mathbf{r}'_k \right)|^2 = 1.$$

The norm of the many body wave function reads

$$\int \mathrm{d}\mathbf{R} \, \mathrm{d}\mathbf{R}' \; |\Phi_{\mathrm{H}}|^2 = 1,$$

where the abbreviations

$$\mathrm{d}\mathbf{R} \equiv \mathrm{d}\mathbf{r}_1 \ldots \mathrm{d}\mathbf{r}_N, \quad \text{and} \quad \mathrm{d}\mathbf{R}' \equiv \mathrm{d}\mathbf{r}'_1 \ldots \mathrm{d}\mathbf{r}'_N$$

are used. Furthermore it is convenient to introduce

$$\psi_i \equiv \psi(\mathbf{r}_i), \quad \chi_k \equiv \chi(\mathbf{r}'_k), \quad \text{and} \qquad U_{ik} \equiv U_{\mathrm{md}}(\mathbf{r}_i, \mathbf{r}'_k).$$

For the energy functional two contributions need to be calculated. First, the energy connected with $\hat{H}_0$, which is given by $E_0 = \langle \Phi_{\mathrm{H}} | \hat{H}_0 | \Phi_{\mathrm{H}} \rangle$. Since $\hat{H}_0$ contains only operators which act on ψ and not on χ, E_0 is equal to energy functional (1.3), which was derived using the standard Hartree ansatz Ψ_{H} given in (1.2). That this is actually true is easily verified:

$$\begin{aligned}
\langle \Phi_{\mathrm{H}} | \hat{H}_0 | \Phi_{\mathrm{H}} \rangle &= \int \mathrm{d}\mathbf{R}\, \mathrm{d}\mathbf{R}'\, \Phi^*_{\mathrm{H}} \hat{H}_0 \Phi_{\mathrm{H}} \\
&= \int \mathrm{d}\mathbf{R}\, \mathrm{d}\mathbf{R}' \prod_{i,k=1}^{N} \psi_i^* \chi_k^* \hat{H}_0 \prod_{l,m}^{N} \psi_l \chi_m \\
&= \int \mathrm{d}\mathbf{R} \prod_{i,m=1}^{N} \psi_i^* \hat{H}_0 \psi_l \underbrace{\prod_{k,m=1}^{N} \int \mathrm{d}\mathbf{R}' \chi_k^* \chi_m}_{=1} \\
&= \langle \Psi_{\mathrm{H}} | \hat{H}_0 | \Psi_{\mathrm{H}} \rangle ,
\end{aligned}$$

where Ψ_{H} is the standard Hartree ansatz

$$\Psi_{\mathrm{H}}(\mathbf{r}_1, \ldots, \mathbf{r}_N) = \prod_{i=1}^{N} \psi(\mathbf{r}_i). \tag{3.5}$$

What is left to do is to calculate the contribution of the mirror potential to the energy functional

$$\begin{aligned}
E_{\mathrm{mir}}[\psi, \chi] &= \langle \Phi_{\mathrm{H}} | \hat{H}_{\mathrm{mir}} | \Phi_{\mathrm{H}} \rangle \\
&= \int \mathrm{d}\mathbf{R}\, \mathrm{d}\mathbf{R}' \prod_{i,k=1}^{N} \psi_i^* \chi_k^* \left(\sum_{\alpha=1}^{N} \sum_{\beta=1}^{N} U_{\alpha\beta} \right) \prod_{l,m}^{N} \psi_l \chi_m \\
&= \sum_{\alpha=1}^{N} \sum_{\beta=1}^{N} \int \mathrm{d}\mathbf{r}_1 \, |\psi_1|^2 \ldots \int \mathrm{d}\mathbf{r}_N \, |\psi_N|^2 \int \mathrm{d}\mathbf{r}'_1 \, |\chi_1|^2 \ldots \int \mathrm{d}\mathbf{r}'_N \, |\chi_N|^2 \\
&\quad \times \int \mathrm{d}\mathbf{r}_\alpha \int \mathrm{d}\mathbf{r}_\beta \, \psi_\alpha^* \psi_\alpha U_{\alpha\beta} \chi_\beta \chi_\beta^* \\
&= N^2 \int \mathrm{d}\mathbf{r} \int \mathrm{d}\mathbf{r}' \, \psi^*(\mathbf{r}) \, \psi(\mathbf{r}) \, U_{\mathrm{md}}(\mathbf{r}, \mathbf{r}') \, \chi^*(\mathbf{r}') \, \chi(\mathbf{r}') .
\end{aligned}$$

To get the expression in the last line, one needs to use the fact that the wave functions are normalized. This makes every factor in the product equal to 1, except the factor with $i = l = \alpha$ and $k = m = \beta$. Since each term in the sum is identical, it is sufficient to pick one and multiply it by the number of terms, which finally yields the last line. Since E_0 is the same as (1.3), the result of the variation is the GPE presented in (1.4). Additional terms can only arise by the variation of E_{mir}. By doing that, it is important to bear in mind that ψ and χ are not independent functions. Since χ describes the mirror atoms, it is merely the shifted and mirrored version of ψ. If x_d is the distance between the atom and the surface, the atom and its mirror are separated by $2x_d$. The relation between the wave functions reads

$$\chi(x, y, z) = \psi(-x + 2x_d, y, z).$$

The variation of ψ^* by $\delta\psi^*$, leads also to the variation of χ^* by $\delta\chi^*$. With that, the variation of the mirror potential is found to be

$$\begin{aligned}
& E_{\mathrm{mir}}[\psi^* + \delta\psi^*, \chi^* + \delta\chi^*] \\
= \; & N^2 \int \mathrm{d}\mathbf{r} \int \mathrm{d}\mathbf{r}' \, [\psi^* + \delta\psi^*] \cdot \psi \cdot U_{\mathrm{md}}(\mathbf{r}, \mathbf{r}') \cdot \chi \cdot [\chi^* + \delta\chi^*] \\
= \; & N^2 \int \mathrm{d}\mathbf{r} \int \mathrm{d}\mathbf{r}' \psi \cdot U_{\mathrm{md}}(\mathbf{r}, \mathbf{r}') \cdot \chi \cdot [\psi^*\chi^* + \psi^*\delta\chi^* + \delta\psi^*\chi^* + \delta\psi^*\delta\chi^*] \\
\approx \; & E_{\mathrm{mir}}[\psi, \chi] + \frac{\delta E_{\mathrm{mir}}}{\delta\psi^*},
\end{aligned}$$

with

$$\frac{\delta E_{\mathrm{mir}}}{\delta\psi^*} = N^2 \int \mathrm{d}\mathbf{r} \int \mathrm{d}\mathbf{r}' \psi \cdot U_{\mathrm{md}}(\mathbf{r}, \mathbf{r}') \cdot \chi \cdot [\psi^*\delta\chi^* + \delta\psi^*\chi^*]. \tag{3.6}$$

In the above expression only the terms linear in the variation are kept, the quadratic term is dropped. The first term in this expression describes the change of the energy of a mirror atom in the potential generated by an atom. The second term describes the change of the energy of an atom in the potential generated by a mirror atom. Inverting the x-coordinate of the second term and shifting it by $2x_d$, shows that both terms are equal. The expression simplifies to

$$\frac{\delta E_{\mathrm{mir}}}{\delta\psi^*} = 2N^2 \int \mathrm{d}\mathbf{r} \int \mathrm{d}\mathbf{r}' U_{\mathrm{md}}(\mathbf{r}, \mathbf{r}') |\chi(\mathbf{r}')|^2 \psi(\mathbf{r}) \delta\psi^*. \tag{3.7}$$

The resulting stationary GPE reads

$$\mu\psi(\mathbf{r}) = \left(-\frac{\hbar^2}{2m}\boldsymbol{\nabla}^2 + V_{\mathrm{T}}(\mathbf{r}) + N\int \mathrm{d}\mathbf{r}'\, U(\mathbf{r},\mathbf{r}')\,|\psi(\mathbf{r}')|^2 + 2V_{\mathrm{mir}}(\mathbf{r}) \right)\psi(\mathbf{r}), \quad (3.8)$$

where $V_{\mathrm{mir}}(\mathbf{r})$ is the potential generated by the mirror BEC and reads

$$V_{\mathrm{mir}}(\mathbf{r}) = N\cdot\int \mathrm{d}\mathbf{r}'\, U_{\mathrm{md}}(\mathbf{r},\mathbf{r}')\,|\chi(\mathbf{r}')|^2 . \quad (3.9)$$

3.2 The mirror potential

In this section the mirror potential (3.9) is discussed and different models that are used to calculate it are presented.

3.2.1 Potential generated by a TF ellipsoid

In the following the mirror potential V_{mir} is calculated with the help of the TF approximation. In Section 1.2.2 it was established that the TF approximation provides a good method to find an accurate approximation for the BEC density distribution. The TF approximation fails at the edges of the BEC but provides an accurate description deeper inside the BEC (see Fig. 2.1). Since the potential V_{mir} represents merely a small perturbation to the harmonic trapping potential V_{T}, such details of the density distribution of the mirror BEC do not play an important role. Therefore, the TF density distribution is a suitable model for the mirror BEC. To further simplify the matter, the corrections to the density distribution due to the BEC-surface interaction are neglected for the model of mirror BEC. Thus the mirror BEC density distribution is that of a BEC in a harmonic trap

$$N|\chi(\mathbf{r})|^2 = n_{\mathrm{TF}}(\mathbf{r}) = n_0\left(1 - \frac{x^2}{\lambda_x^2} - \frac{y^2}{\lambda_y^2} - \frac{z^2}{\lambda_z^2}\right). \quad (3.10)$$

The task of calculating the mirror potential is very similar to the task of calculating the dipole-dipole interaction potential between the atoms in the BEC, which was discussed in Section 1.2.2. It is again convenient to

use expression (1.11) for the dipole-dipole interaction where the long range and the short range component of the potential are separated

$$U_{\mathrm{md}}\left(\mathbf{r}-\mathbf{r}'\right)=-g_s\varepsilon_D^{(m)}\left(\frac{3}{4\pi}\frac{\partial^2}{\partial z^2}\frac{1}{\left|\mathbf{r}-\mathbf{r}'\right|}+\delta\left(\mathbf{r}-\mathbf{r}'\right)\right). \tag{3.11}$$

Here the parameter $\varepsilon_D^{(m)}$ is introduced. Although it is actually the same parameter as ε_D, which was defined in (1.12), it is still useful to make this distinction. The parameter $\varepsilon_D^{(m)}$ describes the interaction between the atoms and the superconductor, while ε_D describes the interaction between the atoms in the BEC. It is often convenient to set $\varepsilon_D=0$ and study the interaction for the case of a non-dipolar BEC. However, in a real setup, ε_D and $\varepsilon_D^{(m)}$ always have the same value. The delta function in the above expression for the interaction potential never contributes, since a real atom and a mirror atom can never be at the same position. As was stated in the previous section, the case where wave function ψ and χ have a significant overlap is not allowed. Only the long range component of U_{md} plays a role for the mirror potential. With $\rho_{\mathrm{mir}}\left(\mathbf{r}\right)=n_{\mathrm{TF}}\left(\mathbf{r}\right)/n_0$, the mirror potential reads

$$\begin{aligned} V_{\mathrm{mir}}\left(\mathbf{r}\right) &= -3\varepsilon_D^{(m)}g_s n_0\frac{\partial^2}{\partial z^2}\frac{1}{4\pi}\int \mathrm{d}\mathbf{r}'\,\frac{\rho_{\mathrm{mir}}\left(\mathbf{r}'\right)}{\left|\mathbf{r}-\mathbf{r}'\right|} \\ &= -3\varepsilon_D^{(m)}g_s n_0\frac{\partial^2}{\partial z^2}\phi_{\mathrm{mir}}\left(\mathbf{r}\right). \end{aligned} \tag{3.12}$$

The potential function ϕ_{mir} is evaluated in the same way as the potential function ϕ presented in Section 1.2.2. The analogy to the gravitational potential of an ellipsoidal still holds, only this time the potential needs to be evaluated at a point outside of the density distribution ρ_{mir}. In this case the one dimensional representation of the integral is given by (1.25) instead of (1.24). The potential function reads

$$\phi_{\mathrm{mir}}\left(\mathbf{r}\right)=\frac{\lambda_x\lambda_y\lambda_z}{8}\int\limits_{W(\mathbf{r})}^{\infty}\mathrm{d}u\,\alpha\left(\mathbf{r},\,u\right), \tag{3.13}$$

with

$$\alpha\left(\mathbf{r},\,u\right)=\frac{\left(1-\frac{x^2}{\lambda_x^2+u}-\frac{y^2}{\lambda_y^2+u}-\frac{z^2}{\lambda_z^2+u}\right)^2}{\sqrt{\left(\lambda_x^2+u\right)\left(\lambda_y^2+u\right)\left(\lambda_z^2+u\right)}}. \tag{3.14}$$

The integration limit $W\left(\mathbf{r}\right)$ was already defined in (1.26) and reads

$$\frac{x^2}{\lambda_x^2+W\left(\mathbf{r}\right)}+\frac{y^2}{\lambda_y^2+W\left(\mathbf{r}\right)}+\frac{z^2}{\lambda_z^2+W\left(\mathbf{r}\right)}=1. \tag{3.15}$$

Next, the second derivative of ϕ_{mir} with respect to z needs to be determined. By taking the derivative of this expression, one has to keep in mind that the lower integration limit also depends on z. Applying the Leibniz rule, the derivative is found to be

$$\begin{aligned}\frac{\partial \phi_{\text{mir}}(\mathbf{r})}{\partial z} &= \frac{\lambda_x\lambda_y\lambda_z}{8}\frac{\partial}{\partial z}\int\limits_{W(\mathbf{r})}^{\infty} \mathrm{d}u\, \alpha(\mathbf{r},\, u) \\ &= \frac{\lambda_x\lambda_y\lambda_z}{8}\left[-\alpha(\mathbf{r},\, W(\mathbf{r}))\frac{\partial W(\mathbf{r})}{\partial z} + \int\limits_{W(\mathbf{r})}^{\infty} \mathrm{d}u\, \frac{\partial \alpha(\mathbf{r},\, u)}{\partial z}\right].\end{aligned}$$

It is easy to see from definition (3.15) of the elliptic coordinate $W(\mathbf{r})$ that $\alpha(\mathbf{r},\, W(\mathbf{r})) = 0$. Only the second term in the above given expression remains, which yields

$$\frac{\partial \phi_{\text{mir}}(\mathbf{r})}{\partial z} = \frac{\lambda_x\lambda_y\lambda_z}{8}\int\limits_{W(\mathbf{r})}^{\infty} \mathrm{d}u\, \frac{\partial \alpha(\mathbf{r},\, u)}{\partial z}. \tag{3.16}$$

In the same way the second derivative is calculated to be

$$\begin{aligned}\frac{\partial^2 \phi_{\text{mir}}(\mathbf{r})}{\partial z^2} &= \frac{\lambda_x\lambda_y\lambda_z}{8}\frac{\partial}{\partial z}\int\limits_{W(\mathbf{r})}^{\infty} \mathrm{d}u\, \frac{\partial}{\partial z}\alpha(\mathbf{r},\, u) \\ &= \frac{\lambda_x\lambda_y\lambda_z}{8}\left[-\left.\frac{\partial \alpha(\mathbf{r},\, u)}{\partial z}\right|_{u=W(\mathbf{r})}\frac{\partial W(\mathbf{r})}{\partial z} + \int\limits_{W(\mathbf{r})}^{\infty} \mathrm{d}u\, \frac{\partial^2 \alpha(\mathbf{r},\, u)}{\partial z^2}\right].\end{aligned}$$

This time, the derivative of $\alpha(\mathbf{r},\, u)$ is needed. It is easily calculated, and reads

$$\frac{\partial \alpha(\mathbf{r},\, u)}{\partial z} = \frac{-4\frac{z}{\lambda_z^2+u}\left(1 - \frac{x^2}{\lambda_x^2+u} - \frac{y^2}{\lambda_y^2+u} - \frac{z^2}{\lambda_z^2+u}\right)}{\sqrt{\left(\lambda_x^2+u\right)\left(\lambda_y^2+u\right)\left(\lambda_z^2+u\right)}}. \tag{3.17}$$

From the definition of $W(\mathbf{r})$ it is obvious that also the derivate of α vanishes at $u = W(\mathbf{r})$

$$\left.\frac{\partial \alpha(\mathbf{r},\, u)}{\partial z}\right|_{u=W(\mathbf{r})} = 0,$$

which finally yields the following relation for the derivative

$$\frac{\partial^2 \phi_{\text{mir}}(\mathbf{r})}{\partial z^2} = \frac{\lambda_x\lambda_y\lambda_z}{8}\int\limits_{W(\mathbf{r})}^{\infty} \mathrm{d}u\, \frac{\partial^2 \alpha(\mathbf{r},\, u)}{\partial z^2}. \tag{3.18}$$

With the second derivate of α

$$\frac{\partial^2 \alpha\left(\mathbf{r},\, u\right)}{\partial z^2} = 4\frac{\frac{2z^2}{(\lambda_z^2+u)} - \left(1 - \frac{x^2}{\lambda_x^2+u} - \frac{y^2}{\lambda_y^2+u} - \frac{z^2}{\lambda_z^2+u}\right)}{\left(\lambda_z^2+u\right)\sqrt{\left(\lambda_x^2+u\right)\left(\lambda_y^2+u\right)\left(\lambda_z^2+u\right)}}, \tag{3.19}$$

the final result is given by

$$\frac{\partial^2 \phi_{\mathrm{mir}}\left(\mathbf{r}\right)}{\partial z^2} = -\frac{\lambda_x\lambda_y\lambda_z}{2}\int\limits_{W(\mathbf{r})}^{\infty} \mathrm{d}u\, \frac{\left(1 - \frac{x^2}{\lambda_x^2+u} - \frac{y^2}{\lambda_y^2+u} - 3\frac{z^2}{\lambda_z^2+u}\right)}{\left(\lambda_z^2+u\right)\sqrt{\left(\lambda_x^2+u\right)\left(\lambda_y^2+u\right)\left(\lambda_z^2+u\right)}}. \tag{3.20}$$

Again, the use of index integrals is convenient:

$$\begin{aligned} J_a &\equiv J_a\left(\mathbf{r};\lambda_x,\lambda_y,\lambda_z\right) \\ &= \int\limits_{W(\mathbf{r})}^{\infty} \frac{\mathrm{d}u}{\sqrt{\left(\lambda_x^2+u\right)\left(\lambda_y^2+u\right)\left(\lambda_z^2+u\right)}}\frac{1}{\left(\lambda_a^2+u\right)}, \end{aligned} \tag{3.21}$$

and

$$\begin{aligned} J_{ab} &\equiv J_a\left(\mathbf{r};\lambda_x,\lambda_y,\lambda_z\right) \\ &= \int\limits_{W(\mathbf{r})}^{\infty} \frac{\mathrm{d}u}{\sqrt{\left(\lambda_x^2+u\right)\left(\lambda_y^2+u\right)\left(\lambda_z^2+u\right)}}\frac{1}{\left(\lambda_a^2+u\right)\left(\lambda_b^2+u\right)}, \end{aligned} \tag{3.22}$$

with $a, b \in \{x, y, z\}$. This allows to express the second derivative of ϕ_{mir} in terms of the index integrals J, which reads

$$\begin{aligned} \varphi_{\mathrm{mir}}\left(\mathbf{r}\right) &\equiv \frac{\partial^2 \phi_{\mathrm{mir}}\left(\mathbf{r}\right)}{\partial z^2} \\ &= -\frac{\lambda_x\lambda_y\lambda_z}{2}\left(J_z - J_{xz}x^2 - J_{yz}y^2 - 3J_{zz}z^2\right). \end{aligned} \tag{3.23}$$

Note, that this expression is very similar to the expression of φ which was given in Eq. (1.30). However, instead of the index integrals I, the index integrals J appear. The reason for that is that all terms connected to the derivatives of the lower integration limit vanished due to the definition of W. This is not the case for higher derivatives of ϕ_{mir}. A crucial difference between φ_{mir} and φ, is the fact that the index integrals J, contrary to the index integrals I, depend on the position $\mathbf{r}$. Thus, φ_{mir} is a rather complicated function of the coordinates x, y and z and not simply a polynomial of second order like φ.

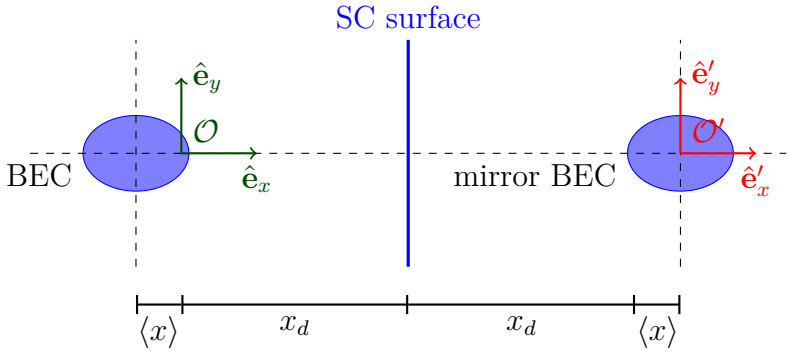

Figure 3.1: The minimum of the harmonic trap is positioned in a distance x_d from the surface. It coincides with the origin $\mathcal{O}$ of the stationary coordinate system $\mathcal{K}$. The BEC is oscillating and its center is shifted by $\langle x \rangle$ away from the origin $\mathcal{O}$. The center of the mirror BEC coincides with the origin $\mathcal{O}'$ of the co-moving coordinate system $\mathcal{K}'$. The mirror potential is calculated within the coordinate System $\mathcal{K}'$ and the numerical calculations are preformed in $\mathcal{K}$. The transformation between $\mathcal{K}'$ and $\mathcal{K}$ is given by $x = x' + 2x_d + \langle x \rangle$.

The above given expressions connected to V_{mir} are all valid in the frame of reference where the center of the mirror BEC coincides with the origin. For the numerical calculation it is preferable to use a coordinate system where the origin coincides with the minimum of the harmonic trapping potential V_{T}. The transformation is simply a shift by $2x_d$ in the x-direction, where x_d is the distance between the minimum of the harmonic trap and the superconducting surface. However, this is only true if the BEC is stationary and does not oscillate in the x-direction. For an oscillating BEC the position of the center-of-mass $\langle x \rangle$ needs to be considered. The sought expression for the mirror potential reads

$$\tilde{V}_{\mathrm{mir}}\left(\mathbf{r};\, x_d, \langle x \rangle\right) = -3\varepsilon_D^{(m)} g_s n_0 \varphi_{\mathrm{mir}}\left(\mathbf{r} - \left(2x_d + \langle x \rangle\right)\hat{\mathbf{e}}_x\right). \tag{3.24}$$

The situation is depicted in Fig 3.1.

Using the index integrals to determine the mirror potential has the advantage that instead of a three-dimensional integral, four one-dimensional integrals need to be solved. The numerical effort involved in solving four one-dimensional integrals is far less than solving one three-dimensional integral. In fact, it is possible to reduce the number of index integrals which need to be calculated numerically, since there exist algebraic relations between the different index integrals. If the BEC is spherical or uni-axial, it is even possible to give analytical expressions for the index integrals.

A more detailed discussion of the integrals is given in Chandrasekhar's book [87], as well as in Ref. [57] for the index integrals I. A summary of the central properties, needed to calculate the mirror potential, is presented in Appendix B.

3.2.2 The column density model

Using a three dimensional TF ellipsoid to model the mirror BEC has the downside that in general the potential needs to be calculated numerically. For the numerical solution of the GPE this is not a very important issue, since it is only a minor numerical task to solve the index integrals, compared to the numerical effort involved in solving the GPE itself. However, for an analytical approximation of the problem, the model for the potential generating mirror BEC needs to be further simplified. Therefore, the so-called *column density* model [52] is presented in this section. Consider a harmonic trap with $\omega_x, \omega_y \gg \omega_z$. The resulting TF ellipsoid is very elongated in the z-direction, i.e. $\lambda_x, \lambda_y \ll \lambda_z$. The minimum of the trap is located in a distance x_d from the superconducting surface which lays in the plane $x = 0$. Assume a situation where the distance x_d is a lot larger than the radial expansion of the BEC: $x_d \gg \lambda_x, \lambda_y$. However, the length $2\lambda_z$ of the BEC may be of the same order as x_d, or even larger. In such a situation, it is reasonable to assume that the details of the atom distribution along the radial direction of the BEC are not very important for the potential generated in a distance $2x_d$. Whereas the distribution of the atoms along the z-direction does play a significant role. In such a case, the three dimensional density distribution $n_{\mathrm{TF}}(\mathbf{r})$ may be approximated by a one-dimensional column density distribution $n_{1\mathrm{D}}(z)$. The column density is constructed from $n_{\mathrm{TF}}(\mathbf{r})$ by integrating over the radial direction. In order for this to work, the BEC may even be tri-axial with $\lambda_x \neq \lambda_y \neq \lambda_z$, as long as both axes are small compared to λ_z and x_d. The resulting column density reads

$$\begin{aligned} n_{1\mathrm{D}}(z) &= n_0 \int \mathrm{d}x \int \mathrm{d}y \left(1 - \frac{x^2}{\lambda_x^2} - \frac{y^2}{\lambda_y^2} - \frac{z^2}{\lambda_z^2}\right) \\ &= n_0 \frac{\pi \lambda_x \lambda_y}{2} \left(1 - \frac{z^2}{\lambda_z^2}\right)^2 . \end{aligned} \tag{3.25}$$

By integrating $n_{1\mathrm{D}}(z)$ along the length of the BEC one finds the number of atoms in the BEC

$$\int_{-\lambda_z}^{\lambda_z} \mathrm{d}z' \, n_{1\mathrm{D}}(z) = N.$$

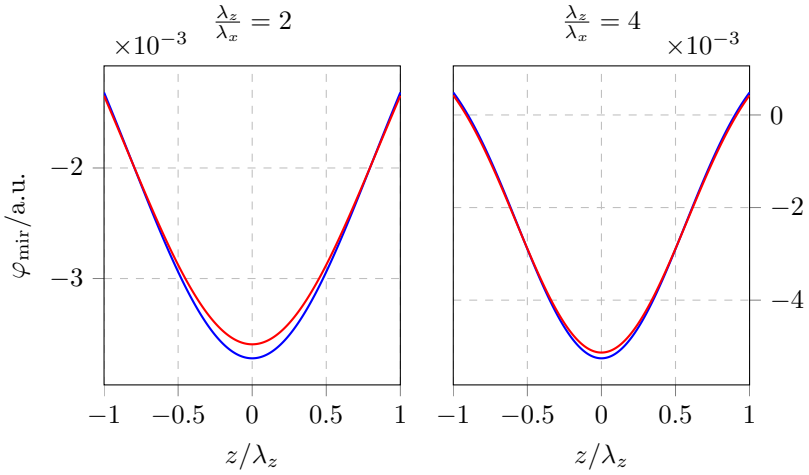

Figure 3.2: φ_{mir} vs. z. The blue lines show φ_{mir} and the red lines show $\varphi_{\mathrm{mir}}^{(1\mathrm{D})}$. The potential is shown along a line with $x = 4\lambda_x$ and $y = 0$. The mirror BEC generating the potential is uni-axial with $\lambda_x = \lambda_y$ and in the left panel has an aspect ratio of $\lambda_z/\lambda_x = 2$ and in the right panel $\lambda_z/\lambda_x = 4$.

Defining the following potential function along the axis of the column density

$$\varphi_{\mathrm{mir}}^{(1\mathrm{D})}(\mathbf{r}) = \frac{1}{4\pi}\int \mathrm{d}z'\,\rho_{1\mathrm{D}}(z')\left[\frac{3(z-z')^2}{|\mathbf{r}-z'\hat{\mathbf{e}}_z|^5} - \frac{1}{|\mathbf{r}-z'\hat{\mathbf{e}}_z|^3}\right], \tag{3.26}$$

with $\rho_{1\mathrm{D}}(z) = n_{1\mathrm{D}}(z)/n_0$, the one dimensional mirror potential takes the guise

$$V_{\mathrm{mir}}^{(1\mathrm{D})}(\mathbf{r}) = -3\varepsilon_D^{(m)} g_s n_0 \varphi_{\mathrm{mir}}^{(1\mathrm{D})}(\mathbf{r}). \tag{3.27}$$

Comparing this expression to (3.24) shows that $\varphi_{\mathrm{mir}}^{(1\mathrm{D})}$ is the approximation of (3.23). The integral that appears in $\varphi_{\mathrm{mir}}^{(1\mathrm{D})}$ can be solved analytically, but since the result is a rather long expression it is not presented here. A comparison of the potential function φ_{mir} and $\varphi_{\mathrm{mir}}^{(1\mathrm{D})}$ is shown in Fig. 3.2. One can see that even for a not very elongated BEC with $\lambda_z/\lambda_x = 2$ the potential of the one dimensional and the three dimensional BEC are almost identical. As the BEC becomes more elongated, the agreement becomes even better. It is also clear that the farther away from the mirror BEC one gets, the better the approximation with the one dimensional mirror BEC gets. The distance presented in Fig. 3.2 is the relevant distance for the calculations in the subsequent chapters.

3.3 Numerical approach to solve the GPE

In Section 2.3.2 a numerical method for the time evolution of the GPE was presented. In this section a way to incorporate the mirror potential into this time evolution scheme is presented. As was discussed in the previous section, the mirror potential depends on the center of mass of the BEC, in particular its x-coordinate. For the determination of the ground state this is not a problem, since the position only changes minimally during the diffusion process and finally relaxes in a fixed position. For the time evolution the situation is rather different. From the stationary GPE (3.8), derived in Section 3.1, it is clear that the time dependent GPE takes the guise

$$\begin{aligned} i\hbar\frac{\partial}{\partial t}\psi(\mathbf{r},t) &= \Bigg(-\frac{\hbar^2}{2m}\boldsymbol{\nabla}^2 + \frac{m}{2}\left(\omega_x^2x^2+\omega_y^2y^2+\omega_z^2z^2\right) \\ &\quad + Ng_s\Bigg[(1-\varepsilon_D)\left|\psi(\mathbf{r},t)\right|^2 - 3\varepsilon_D\frac{1}{4\pi}\frac{\partial^2}{\partial z^2}\int \mathrm{d}\mathbf{r}'\frac{\left|\psi(\mathbf{r}',t)\right|^2}{|\mathbf{r}-\mathbf{r}'|} \\ &\quad - \varepsilon_D^{(m)}\frac{45}{4\pi\lambda_x\lambda_y\lambda_z}\varphi_{\mathrm{mir}}\left(\mathbf{r}-(2x_d+\langle x\rangle)\,\hat{\mathbf{e}}_x\right)\Bigg]\Bigg). \end{aligned} \tag{3.28}$$

The mirror potential φ_{mir} is calculate via (3.23). $\langle x\rangle$ is the center of mass of the BEC at the time t. Since the BEC oscillates, $\langle x\rangle$ is time dependent quantity. Thus, in every time step the position of the center of mass needs to be updated. During a single time step, the center of mass moves from a position $\langle x\rangle = x_j$ to a position $\langle x\rangle = x_{j+1}$. The question is: What position $\langle x\rangle$ to use for the calculation of the mirror potential? If one would simply use $\langle x\rangle = x_j$, a systematic error would be introduced into the time evolution. What is actually needed is some kind of effective position for the center of mass, which is more representative for the whole time step than x_j. The mean $\bar{x} = \frac{1}{2}(x_j + x_{j+1})$ would be such an representative value. Unfortunately the position x_{j+1} is of course unknown before the time step is completed. One possibility to deal with this would be to determine x_{j+1} by a self consistent calculation of every time step. This would lead to a drastic increase of the computational effort involved in calculating a single time step. To avoid this, the time splitting method offers a simple solution. As was shown, the application of $e^{-i\frac{\hat{V}}{\hbar}\Delta t}$ does not change $|\psi|^2$ and with that also the position $\langle x\rangle$ of the center of mass remains constant. Only the application of $e^{-i\frac{\hat{K}}{\hbar}\frac{\Delta t}{2}}$ shifts the position of the center of mass. And since only the operator for a half time step $\Delta t/2$ is applied, it does not

shift $\langle x \rangle$ to its final position x_{j+1}, but rather to an intermediate position $\tilde{x}$. Since the BEC does not move with a constant velocity, but performs an oscillation, $\tilde{x}$ is not exactly equal to $\bar{x}$. Nevertheless, $\tilde{x}$ is a adequate value to represent the center-of-mass position for the whole time step. For the first part of the time step the position of the center of mass is not important, since $\hat{K}$ does not depend on $\langle x \rangle$. Before the time step is continued, it is necessary to calculate the mirror potential using $\langle x \rangle = \tilde{x}$. Next, $e^{-i\frac{\hat{V}}{\hbar}\Delta t}$ is applied and finally $e^{-i\frac{\hat{K}}{\hbar}\frac{\Delta t}{2}}$, which concludes the time step. It is clear that the described method works for the splitting scheme $e^{-\frac{i}{2}\frac{\hat{K}}{\hbar}\Delta t}e^{-i\frac{\hat{V}}{\hbar}\Delta t}e^{-\frac{i}{2}\frac{\hat{K}}{\hbar}\Delta t}$. But what about the splitting scheme $e^{-\frac{i}{2}\frac{\hat{V}}{\hbar}\Delta t}e^{-i\frac{\hat{K}}{\hbar}\Delta t}e^{-\frac{i}{2}\frac{\hat{V}}{\hbar}\Delta t}$? As was shown in Section 2.3.2 this splitting scheme is useful since it reduces the number of necessary Fourier transformation per time step. The same arguments as above also apply for this scheme. In terms of a single time step, the only difference is: instead of a single center-of-mass position representing the whole time step, one has two center-of-mass position in order to calculate the mirror potential. For the first half of the time step the initial center-of-mass position is used, and for the last half of the time step, the final position is used.

The approach for the numerical calculations is the following: First the ground state is determined by solving the stationary GPE (3.8), using the GFDN with backward Euler time discretization presented in Section 2.2.1. The distance between the superconducting surface and the harmonic trap minimum is set to be $x_d - x_s$. Next, the time evolution is calculated by solving the time dependent GPE (3.28) using the TSSP, presented in Section 2.3.2, with the above described scheme to deal with the mirror potential. The distance between the superconducting surface and the minimum of the harmonic trap is set to x_d. In this shifted potential the previously determined ground state becomes an excited state, which performs a center-of-mass oscillation with the amplitude x_s around its equilibrium position. Note, that the presence of the mirror potential leads to a slight shift of the minimum of the potential. This means that the equilibrium position of the oscillation is not the minimum of the harmonic trap, but the new potential minimum. The results from these numerical calculations are presented in the next two chapters.

The computational time necessary to solve the GPE was reduced by performing certain parts of the numerical calculation parallel rather than serial. One such operation, that was parallelized, is the three-dimensional Fourier transformation necessary to determine the spatial derivatives. It is composed of one-dimensional Fourier transformations along one-dimensional cuts of the three-dimensional lattice in each spatial direction. These one-

dimensional Fourier transformations are independent operations and can therefore be performed at the same time. Furthermore, since the application of $e^{-i\frac{\hat{V}}{\hbar}\Delta t}$ in position space and the application of $e^{-i\frac{\hat{K}}{\hbar}\Delta t}$ in Fourier space are merely multiplications, they can be evaluated independently at each lattice point. The numerical code was implemented with CUDA and the parallel computations were performed on the GPU. Compared to CPUs, GPUs have a lot more computational cores, thus allow for a much higher degree of parallelization. Besides the above mentioned operations, also the calculation of expectation values, like for example the norm or the center of mass, was parallelized. For this purpose the reduction algorithm form Ref. [93] was used.

Chapter 4

Center-of-mass frequency shift

The mirror potential, which was discussed in the previous chapter, has an influence on the dynamics of a dipolar BEC close to a superconducting surface. In Refs. [54–56] this influence was discussed using the models presented in the previous chapter. Some of the results presented here can also be found in those references.

In this chapter the focus is on the center-of-mass motion of the BEC, and in particular on its oscillation frequency. In a harmonic trap, the center of mass performs a harmonic oscillation. The frequency of the oscillation is determined by the harmonic trap frequency. The mirror potential, generated by the superconducting surface, modifies the curvature of the potential and thereby changes the oscillation frequency.

Since this effect is rather small, it is not clear if the magnitude of the frequency shift is large enough to be detected in an experiment. As a threshold serves a frequency shift of 10^{-5}. In Ref. [53] such an accuracy was demonstrated in an experiment, where the influence of the Casimir-Polder force on the motion of a BEC was investigated. In Refs. [54] and [55] the frequency shift due to the eddy current effect was discussed using the column density model. It was found that if the BEC consists of ^{87}Rb atoms, the frequency shift is of the order of 10^{-5}. This makes the detection of the frequency shift difficult. Especially the measurement of the variation of the frequency shift is rather difficult on this scale. Since a ^{87}Rb atom has a dipole moment of only $1\mu_B$, it is not a good choice for this kind of experiment. A BEC consisting of atoms with larger magnetic dipole moments, like for example ^{52}Cr, which has a six times larger magnetic dipole moment than ^{87}Rb, is preferable. In the case of ^{52}Cr the frequency shift due to the eddy current effect reaches up to an order of 10^{-3}. A frequency shift of this magnitude is well within experimental precision. Measuring the frequency shift of this order, and variations of the frequency shift on this scale, does

not pose a problem. Since those results are based on the column density model, it is necessary to confirm them using more sophisticated models, which was done in Ref. [56]. Those results, alongside with the results form the column density model are presented here in Section 4.1 and Section 4.2.

The eddy current effect is not the only effect that has an influence on the oscillation frequency close to a surface. For example, the Casimir-Polder force, which was already mentioned above, has also an impact on the center-of-mass motion. This makes it necessary to find some characteristic of the eddy current effect, which clearly identifies it. One such characteristic is the dependence of the frequency shift on the number of atoms in the BEC. This was discussed in Refs. [54–56] and is also presented here. Another characteristic is the dependence of the frequency shift on the orientation of the dipoles relative to the surface and relative to the BEC. For dipole orientations parallel to the surface, this was presented in Ref. [56]. Those results are presented here in Section 4.3. Additionally, more general polarizations are presented and discussed here.

As already mentioned, the frequency shift shows a characteristic dependence on the number of atoms in the BEC. However, it is necessary to specify which parameters remain constant while the number of atoms changes. For example one could simply change the number of atoms in the trap, while the trap frequencies remain constant. From the result of the TF approximation for the chemical potential (1.20), it is clear that an increase of the number of atoms leads to a larger chemical potential $\mu^{(0)} \propto N^{2/5}$, and since $n_0^{(0)} = \mu^{(0)}/g_s$, this means that also $n_0^{(0)} \propto N^{2/5}$. Increasing the number of atoms leads to an increase of the BEC density, which means that three body collisions become more probable. Contrary to two body collisions, three body collisions can lead to the formation of molecules. Two of the three atoms form the molecule and the third atom carries away the binding energy. The binding energy is usually larger than the depth of the trap, thus the atom escapes. All three atoms that were involved in the collision are no longer part of the BEC. This mechanism leads to an increased atom loss rate and reduces the life time of the BEC [106]. Therefore the central density shall remain constant rather than the trap frequencies. In order to keep the central density constant while the number of atoms changes, the trap frequencies need to be adjusted properly. The goal is to have different BEC aspect ratios λ_z/λ_x for different numbers of atoms. The BEC is supposed to become more elongated as the number of atoms increases. This is accomplished by keeping the radial trap frequencies constant and adjusting only the axial trap frequency. It is convenient

to work with the ratios of the trap frequencies rather than the number of atoms. That the trap aspect ratio $\nu = \omega_x/\omega_z$ is proportional to the number of atoms is easily seen:

$$\nu = \frac{\omega_x}{\omega_z} = \frac{\lambda_z^{(0)}}{\lambda_x^{(0)}} = \frac{15}{8\pi} \frac{1}{\left[\lambda_x^{(0)}\right]^2 \lambda_y^{(0)}} \frac{N}{n_0^{(0)}} = \frac{15}{8\pi} \frac{\kappa}{\left[\lambda_x^{(0)}\right]^3} \frac{N}{n_0^{(0)}}, \tag{4.1}$$

where only the fact was used that the ratio of the semi axes is equal to the inverse ratio of the trap frequencies and expression (1.21) for the central density was inserted. In the last step the semi-axes $\lambda_y^{(0)}$ was expressed with the trap aspect ratio $\kappa = \omega_y/\omega_x = \lambda_x^{(0)}/\lambda_y^{(0)}$. Expression (4.1) shows that calculating $\gamma(N)$ is equivalent to calculating $\gamma(\nu)$. However, the latter is preferable since it is a more general approach. The semi axes of the BEC are calculated in units of $\Lambda_{\mathrm{TF}} = (G_N)^{1/5} a_\omega$, which yields

$$\frac{\lambda_a^{(0)}}{\Lambda_{\mathrm{TF}}} = \left(\frac{15}{8\pi}\right)^{1/5} \frac{\omega}{\omega_a}, \quad a \in \{x, y, z\}.$$

Since the frequency ω/ω_a can be expressed using solely the trap aspect ratios ν and κ (see (2.2)), the semi axes depend merely on the harmonic trap frequency ratios. Of course, for a dipolar BEC they also depend on ε_D. Measuring the distance to the surface x_d as well as the oscillation amplitude x_s in units of $\lambda_x^{(0)}$, eliminates almost completely the necessity to use absolute units. For the TF calculations absolute values for the number of atoms or semi axes are not needed at all. Only for the numerical calculations they play a somewhat minor role. The only parameter that is influenced by those absolute values is the contact interaction parameter G_N. After some algebra the interaction parameter is found to be

$$G_N = 8\pi \cdot \frac{N \cdot a_s}{a_\omega} = \frac{(8\pi)^{9/4}}{15} \left(a_s n_0^{(0)}\right)^{5/4} \left[\lambda_x^{(0)}\right]^{5/2} \left(\frac{\nu}{\kappa}\right)^{5/6}. \tag{4.2}$$

To determine G_N, the following parameters are used here: The semi axis is set to $\lambda_x^{(0)} = 7\,\mu\mathrm{m}$. This value has no special significance, other than the fact that in the following, the distance between BEC and surface is typically set to $x_d = 2\lambda_x^{(0)}$, and a distance of $14\,\mu\mathrm{m}$ between the superconductor and the harmonic trap minimum is a realistic value, which was demonstrated in Ref. [49]. For the central density a typical value used in the following is $n_0^{(0)} = 2.5 \times 10^{13}\,\mathrm{cm}^{-3}$. Using such a density, the three body loss rate in an experiment should be small enough [106] to allow long enough measurement. For the scattering length the value $a_s = 5.7\,\mathrm{nm}$ is used. It is the value for ^{87}Rb atoms and is used here as a typical value. For example, for ^{52}Cr the

scattering length is $a_s = 5.1\,\mathrm{nm}$, thus the above choice does not seem too bad. However, for rare earth atoms like dysprosium or erbium this might not be accurate at all. Nevertheless, it is still adequate to use 5.7 nm, since it is not too important for the purpose of this work. As long as the value of G_N is large enough, so that the BEC is in the TF regime, the precise value of G_N is not important. The only two variable parameters left are the aspect ratios of the harmonic trap frequencies. In the following the trap is always cigar shaped with $\kappa = 1$, or at least almost cigar shaped with $\kappa \approx 1$. The second aspect ratio is typically varied from $\nu = 1$ up to about $\nu = 15$. This corresponds to a variation of the interaction parameter from $G_N \approx 10^3$ to $G_N \approx 10^4$. In any case, the interaction parameter is sufficiently large. In the following the plots usually start at $\nu = 0$, which corresponds to $N = 0$. This means that there is no BEC, which renders the point $\gamma(0) = 0$ meaningless and should be disregarded. Also points very close to $\nu = 0$ are questionable since in the case that there are only a few atoms in the trap, the GPE as well as the TF approximation are not applicable. But since those points are of no interest it is not necessary to further discuss this.

4.1 Frequency shift within TF approximation

In Ref. [52] Antezza et al. presented a way to calculate the frequency shift of a BEC caused by the interaction between the BEC and the surface due to the Casimir-Polder force. For the density distribution of the BEC they used the column density model which was discussed in the previous chapter. However, the method is not restricted to this type of density. Here their method is adopted for the purpose of calculating the frequency shift due to the eddy current effect. In this section, the method of Antezza et al. is recapitulated and it is shown how to adopt it for the eddy current effect.

Consider a BEC in a harmonic trap $V_\mathrm{T}(\mathbf{r})$ close the the surface of the superconductor. The potential generated by the superconductor is denoted by $V_\mathrm{mir}(\mathbf{r})$. The total external potential is $V(\mathbf{r}) = V_\mathrm{T}(\mathbf{r}) + V_\mathrm{mir}(\mathbf{r})$. Say the BEC consists of N atoms. The center of mass of each individual atom is given by $\langle x_i \rangle$, which means that the BEC center of mass is

$$x_\mathrm{c.m.} = \frac{1}{N} \left\langle \sum_{i=1}^{N} x_i \right\rangle . \tag{4.3}$$

The total momentum of the BEC is the sum of the momenta $p_{x,i}$ of each

atom in the BEC

$$P_x = \left\langle \sum_{i=1}^{N} p_{x,i} \right\rangle . \tag{4.4}$$

The total momentum P_x is connected to the velocity of the center of mass via

$$\frac{\mathrm{d}x_{\mathrm{c.m.}}}{\mathrm{d}t} = \frac{P_x}{Nm}. \tag{4.5}$$

Newtons second law states that the force F is given by the time derivative of the momentum. On the other hand the force is also equal to the negative gradient of the external potential. With that the time derivative of the x-component of the total momentum reads

$$\begin{aligned} \frac{1}{N}\frac{\mathrm{d}P_x}{\mathrm{d}t} &= -\frac{1}{N}\left\langle \sum_{i=1}^{N} \frac{\partial V(\mathbf{r}_i)}{\partial x_i} \right\rangle \\ &= -\frac{m\omega_x^2}{N}\left\langle \sum_{i=1}^{N} x_i \right\rangle - \frac{1}{N}\left\langle \sum_{i=1}^{N} \frac{\partial V_{\mathrm{mir}}(\mathbf{r}_i)}{\partial x_i} \right\rangle \\ &= -m\omega_x^2 x_{\mathrm{c.m.}}(t) - \frac{1}{N}\int \mathrm{d}\mathbf{r}\, n(\mathbf{r},t)\, \frac{\partial V_{\mathrm{mir}}(\mathbf{r})}{\partial x}, \end{aligned} \tag{4.6}$$

where the expectation value $\langle a \rangle = N^{-1}\int \mathrm{d}\mathbf{r}\, a \cdot n(\mathbf{r},t)$ was inserted. Since the BEC performs a harmonic oscillation, its atom density distribution $n(\mathbf{r},t)$ is a time dependent quantity. The situation can be simplified by the assumption that the shape of the BEC remains constant during the oscillation. If that is the case, the time dependent density can be written as $n(\mathbf{r},t) = n_{\mathrm{TF}}(\mathbf{r} - x_{\mathrm{c.m.}}(t)\,\hat{\mathbf{e}}_x)$. Here it was already assumed that the density distribution is a TF ellipsoid (1.23). Actually it is not true that the shape of the BEC remains constant during the oscillation. In fact, the BEC shape oscillations are in the focus of the next chapter. However, the shape fluctuations of the BEC are too small to be of significance here. With all that has been said, equation (4.6) takes the guise

$$\frac{\mathrm{d}^2 x_{\mathrm{c.m.}}}{\mathrm{d}t^2} = -\omega_x^2 x_{\mathrm{c.m.}} - \frac{1}{mN}\int \mathrm{d}\mathbf{r}\, n_{\mathrm{TF}}(\mathbf{r} - x_{\mathrm{c.m.}}\hat{\mathbf{e}}_x)\, \frac{\partial V_{\mathrm{mir}}(\mathbf{r})}{\partial x}. \tag{4.7}$$

For the following it is more convenient to transform the integral in this equation such that the density distribution becomes stationary and the potential becomes a time-dependent quantity. In the center-of-mass frame of the BEC the integral reads

$$Q(t) \equiv \int \mathrm{d}\mathbf{r}\, n_{\mathrm{TF}}(\mathbf{r})\, \frac{\partial}{\partial x} V_{\mathrm{mir}}(\mathbf{r} + x_{\mathrm{c.m.}}\hat{\mathbf{e}}_x). \tag{4.8}$$

Next, the time dependent part of the integrand is expanded into a Taylor series in terms of $x_{\text{c.m.}}$ about $x_{\text{c.m.}} = 0$:

$$\begin{aligned}\frac{\partial}{\partial x}V_{\text{mir}}\left(\mathbf{r}+x_{\text{c.m.}}\hat{\mathbf{e}}_x\right) &= \frac{\partial V_{\text{mir}}(\mathbf{r})}{\partial x}+\frac{\partial^2 V_{\text{mir}}(\mathbf{r})}{\partial x^2}x_{\text{c.m.}}(t)\\ &\quad+\frac{1}{2}\frac{\partial^3 V_{\text{mir}}(\mathbf{r})}{\partial x^3}x_{\text{c.m.}}^2(t)+\frac{1}{6}\frac{\partial^4 V_{\text{mir}}(\mathbf{r})}{\partial x^4}x_{\text{c.m.}}^3(t)\\ &\quad+\mathcal{O}\left(x_{\text{c.m.}}^4(t)\right)\\ &\equiv f(t). \end{aligned} \tag{4.9}$$

Since the center of mass performs a harmonic oscillation, a suitable ansatz for $x_{\text{c.m.}}$ is given by $x_{\text{c.m.}}(t) = x_s\cos(\omega' t)$. Thus, a natural way to express $f(t)$ is a cosine series

$$f(t) = \frac{a_0}{2}+\sum_{n=1}^{\infty}a_n\cos\left(\frac{2\pi}{T}n\cdot t\right),$$

where the coefficients are given by

$$a_n = \frac{2}{T}\int_0^T \mathrm{d}t\, f(t)\cos\left(\frac{2\pi}{T}n\cdot t\right) = \frac{\omega_x'}{\pi}\int_0^{2\pi/\omega_x'}\mathrm{d}t\, f(t)\cos(n\cdot\omega_x' t).$$

Evaluating this expression for $n = 0$ and $n = 1$ yields

$$a_0 = 2\frac{\partial V_{\text{mir}}(\mathbf{r})}{\partial x}+\frac{x_s^2}{2}\frac{\partial^3 V_{\text{mir}}(\mathbf{r})}{\partial x^3},$$

and

$$a_1 = x_s\frac{\partial^2 V_{\text{mir}}(\mathbf{r})}{\partial x^2}+\frac{x_s^3}{8}\frac{\partial^4 V_{\text{mir}}(\mathbf{r})}{\partial x^4}.$$

Since only the frequency shift of the harmonic oscillation is of interest, it is unnecessary to consider higher frequency terms in the cosine series. This result is now inserted back in expression (4.8) for $Q(t)$, which then yields

the following equation of motion:

$$\begin{aligned}
\frac{\mathrm{d}^2 x_{\mathrm{c.m.}}}{\mathrm{d}t^2} &= -\omega_x^2 x_{\mathrm{c.m.}} - \frac{1}{mN}\int d\mathbf{r}\, n_{\mathrm{TF}}(\mathbf{r})\,\frac{a_0}{2} \\
&\quad -\frac{1}{mN}\int d\mathbf{r}\, n_{\mathrm{TF}}(\mathbf{r})\left\{\frac{\partial^2 V_{\mathrm{mir}}(\mathbf{r})}{\partial x^2} + \frac{x_s^2}{8}\frac{\partial^4 V_{\mathrm{mir}}(\mathbf{r})}{\partial x^4}\right\} x_{\mathrm{c.m.}} \\
&= \underbrace{-\frac{1}{mN}\int d\mathbf{r}\, n_{\mathrm{TF}}(\mathbf{r})\,\frac{a_0}{2}}_{x_0\omega_x'^2} \\
&\quad \underbrace{-\left[\frac{1}{mN}\int d\mathbf{r}\, n_{\mathrm{TF}}(\mathbf{r})\left\{\frac{\partial^2 V_{\mathrm{mir}}(\mathbf{r})}{\partial x^2} + \frac{x_s^2}{8}\frac{\partial^4 V_{\mathrm{mir}}(\mathbf{r})}{\partial x^4}\right\} + \omega_x^2\right]}_{=\omega_x'^2} x_{\mathrm{c.m.}} \\
&= -\omega_x'^2\,(x_{\mathrm{c.m.}} - x_0)
\end{aligned}$$

The solution to this equation is obviously given by $x_{\mathrm{c.m.}} = x_s\cos(\omega_x' t) + x_0$, where x_0 is the new equilibrium position of the oscillation and ω_x' the new oscillation frequency. If the difference between the new oscillation frequency and the harmonic trap frequency is small, one can write

$$\omega_x'^2 - \omega_x^2 = (\omega_x' - \omega_x)(\omega_x' + \omega_x) \approx (\omega_x' - \omega_x)\,2\omega_x,$$

and with that the relative frequency shift reads

$$\begin{aligned}
\gamma &\equiv \frac{\omega_x' - \omega_x}{\omega_x} \approx \frac{\omega_x'^2 - \omega_x^2}{2\omega_x^2} \\
&= \frac{1}{2\omega_x^2 mN}\int d\mathbf{r}\, n_{\mathrm{TF}}(\mathbf{r})\left\{\frac{\partial^2 V_{\mathrm{mir}}(\mathbf{r})}{\partial x^2} + \frac{x_s^2}{8}\frac{\partial^4 V_{\mathrm{mir}}(\mathbf{r})}{\partial x^4}\right\}. \qquad (4.10)
\end{aligned}$$

In the case that only small amplitude oscillations are considered, it is sufficient to evaluate the first term in this expression. Oscillations where the amplitude x_s is a lot smaller than the expansion of the BEC are considered small amplitude oscillations. For a TF ellipsoid a measure for the expansion is given by the semi axes λ_x. Note, only the expansion of the BEC in the direction of the motion is relevant for this comparison. As soon as the oscillation amplitude becomes comparable to the BEC expansion, the second term in the above expression becomes important as well. Since in the following, the size of the amplitude of the oscillation is restricted by the distance between the BEC and the surface, higher order corrections in x_s are not needed. That the quadratic term in x_s is sufficient is shown in the following sections.

So far one important fact has been neglected. As the BEC moves, the mirror BEC moves as well. To be more precise, the mirror BEC moves in opposite phase to the original BEC. To account for this, the above given expression for the relative frequency shift needs to be modified. The derivatives of V_{mir} need to be taken with respect to $x/2$ rather than with respect to x. This generates an extra factor of 4 in the term with the second derivative, and an extra factor of 16 in the term with the fourth derivative. The substitutions

$$\frac{\partial^2 V_{\mathrm{mir}}(\mathbf{r})}{\partial x^2} \to 4\frac{\partial^2 V_{\mathrm{mir}}(\mathbf{r})}{\partial x^2}, \tag{4.11}$$

and

$$\frac{\partial^4 V_{\mathrm{mir}}(\mathbf{r})}{\partial x^4} \to 16\frac{\partial^4 V_{\mathrm{mir}}(\mathbf{r})}{\partial x^4} \tag{4.12}$$

need to be performed.

Now, everything is set up to calculate the frequency shift. In Section 4.1.1 the frequency shift is calculated using a three dimensional TF ellipsoid. In Section 4.1.2 the simpler column density model is used.

4.1.1 Frequency shift based on a Thomas-Fermi ellipsoid

In order to calculate the frequency shift the derivatives of the mirror potential V_{mir} are required. As shown in Section 3.2.1, in the case of a three-dimensional Thomas-Fermi ellipsoid, the mirror potential is mainly given by $\varphi_{\mathrm{mir}}(\mathbf{r})$ (see Eq. (3.24)). Now the task is to evaluate the first four derivatives of $\varphi_{\mathrm{mir}}(\mathbf{r})$ with respect to x. The explicit calculation of these derivatives is a rather cumbersome task. Therefore it is not presented here, but in Appendix C instead. The resulting expression for the frequency shift reads

$$\gamma_{\mathrm{TF}} = -\frac{45\varepsilon_D^{(m)}}{8\pi}\frac{\left[\lambda_x^{(0)}\right]^3\lambda_y^{(0)}\lambda_z^{(0)}}{\lambda_x\lambda_y\lambda_z}\int\limits_{\mathbb{D}_{\mathrm{TF}}} d\mathbf{r}\,\rho_{\mathrm{TF}}(\mathbf{r})\left\{F(\mathbf{r}) + \frac{x_s^2}{2}\left.\frac{\partial^2 F(\mathbf{r}')}{\partial x'^2}\right|_{\mathbf{r}'=\mathbf{r}}\right\}, \tag{4.13}$$

with

$$\rho_{\mathrm{TF}}(\mathbf{r}) = \frac{n_{\mathrm{TF}}(\mathbf{r})}{n_0} = \left(1 - \frac{(x-2x_d)^2}{\lambda_x^2} - \frac{y^2}{\lambda_y^2} - \frac{z^2}{\lambda_z^2}\right) \tag{4.14}$$

and the integration domain

$$\mathbb{D}_{\mathrm{TF}} = \left\{\mathbf{r}\in\mathbb{R}^3 \,\middle|\, \frac{(x-2x_d)^2}{\lambda_x^2} + \frac{y^2}{\lambda_y^2} + \frac{z^2}{\lambda_z^2} \le 1\right\}. \tag{4.15}$$

The function F is defined in (C.9). Although it is a very complicated function of the position $\mathbf{r}$, it is nevertheless possible to evaluate it analytically. This is also true for the second derivative of F, which is given in (C.11). Besides the position $\mathbf{r}$, the function F also depends on the BEC semi axes. F is evaluated in the frame of the mirror BEC, which is the reason why the BEC density distribution is shifted by $2x_d\hat{\mathbf{e}}_x$. Note, expression (4.13) only depends on the BEC semi axes (dipolar and non-dipolar), the distance to the surface x_d, the oscillation amplitude x_s, and of course the dipole-dipole interaction strength $\varepsilon_D^{(m)}$.

The integral in (4.13) needs to be solved numerically. Taking the symmetry of the problem into account, it is clear that it is not necessary to integrate over the full ellipsoid. The integrand $K(\mathbf{r}) = F(\mathbf{r}) + \frac{x_s^2}{2}\frac{\partial^2 F(\mathbf{r})}{\partial x^2}$ is symmetric in y as well as in z. This means that it is sufficient to integrate the quarter of the ellipsoid with $y >$ and $z > 0$. The reduced integration domain reads

$$\bar{\mathbb{D}}_{\mathrm{TF}} = \left\{ x \in \mathbb{R}, \{y, z\} \in \mathbb{R}_+^2 \,\middle|\, \frac{(x-2x_d)^2}{\lambda_x^2} + \frac{y^2}{\lambda_y^2} + \frac{z^2}{\lambda_z^2} \leq 1 \right\}. \tag{4.16}$$

The integral over the full domain is connected to the integral over the reduced domain by

$$\begin{aligned} \frac{1}{4}\int\limits_{\mathbb{D}_{\mathrm{TF}}} \mathrm{d}\mathbf{r}\, \rho_{\mathrm{TF}}(\mathbf{r})\, K(\mathbf{r}) &= \int\limits_{\bar{\mathbb{D}}_{\mathrm{TF}}} \mathrm{d}\mathbf{r}\, \rho_{\mathrm{TF}}(\mathbf{r})\, K(\mathbf{r}) \\ &= \int\limits_{-\infty}^{\infty} \mathrm{d}x \int\limits_{0}^{\infty} \mathrm{d}y \int\limits_{0}^{\infty} \mathrm{d}z\, \rho_{\mathrm{TF}}(\mathbf{r}) \cdot F(\mathbf{r}) \cdot \Theta\left(\rho_{\mathrm{TF}}(\mathbf{r})\right), \end{aligned}$$

where $\Theta(x)$ is the Heaviside theta-function

$$\Theta(x) = \begin{cases} 1, & \text{for} \quad x \geq 0 \\ 0, & \text{for} \quad x < 0. \end{cases}$$

In order to solve this integral, the approach is to integrate slices parallel to the plane $y = 0$. The integral in the plane $y = y_i$ reads

$$\begin{aligned} A_i \equiv A(y_i) &= \int\limits_{-\infty}^{\infty} \mathrm{d}x \int\limits_{0}^{\infty} \mathrm{d}z\, \rho_{\mathrm{TF}}(x, y_i, z) \cdot K(x, y_i, z) \cdot \Theta\left(\rho_{\mathrm{TF}}(x, y_i, z)\right) \\ &= \int\limits_{-\lambda_x+2x_d}^{\lambda_x+2x_d} \mathrm{d}x \int\limits_{0}^{z_0(x,y_i)} \mathrm{d}z\, \rho_{\mathrm{TF}}(x, y_i, z) \cdot K(x, y_i, z). \end{aligned} \tag{4.17}$$

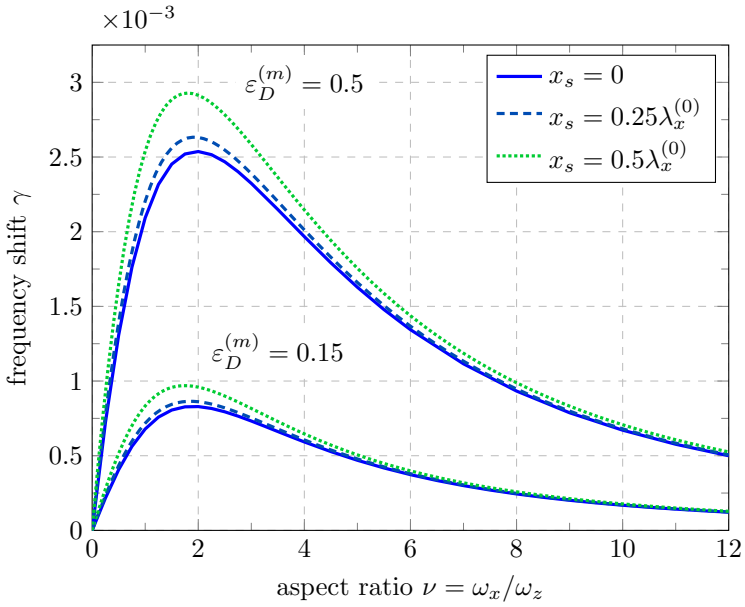

Figure 4.1: Frequency shift γ vs. trap aspect ratio $\nu = \omega_x/\omega_z$. The frequency shift is calculated for a dipolar BEC with $\varepsilon_D = \varepsilon_D^{(m)}$ for two different dipole-dipole interaction parameters $\varepsilon_D^{(m)} = 0.5$ and $\varepsilon_D^{(m)} = 0.15$ (^{52}Cr) and three different oscillation amplitudes $x_s = 0$ (solid line), $x_s = 0.25\lambda_x^{(0)}$ (dashed line) and $x_s = 0.5\lambda_x^{(0)}$ (dotted line). The distance between the harmonic trap minimum and the superconductor is set to $x_d = 2\lambda_x^{(0)}$.

The upper limit of the z-integration is given by

$$z_0\left(x, y_i\right) = \lambda_z \sqrt{1 - \frac{\left(x - 2x_d\right)^2}{\lambda_x^2} - \frac{y_i^2}{\lambda_y^2}}. \tag{4.18}$$

The two dimensional integral (4.17) can be easily solved numerically using software like for example *mathematica*. For the y-integration one can use the trapezoidal rule. Say the quarter ellipsoid is sliced into M slices, separated by Δy from each other. The numerical approximation for the integral reads

$$\int\limits_{\mathbb{D}_{\mathrm{TF}}} \mathrm{d}\mathbf{r}\, \rho_{\mathrm{TF}}\left(\mathbf{r}\right) K\left(\mathbf{r}\right) = 4 \cdot \left(\frac{A_1}{2} + \frac{A_M}{2} + \sum_{i=2}^{M-1} A_i \right) \Delta y.$$

Inserting this into (4.13) yields the frequency shift.

The results are presented in Fig. 4.1, where the frequency shift is shown as a function of the trap aspect ratio ν for different dipole strengths $\varepsilon_D^{(m)}$

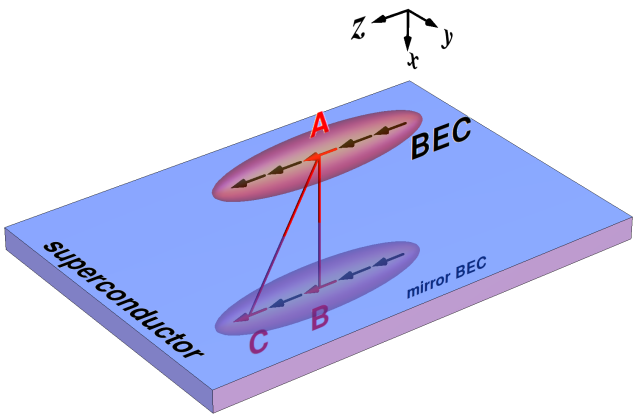

Figure 4.2: Schematic setup, where the dipoles are oriented in the z-direction. Dipole A in the BEC and dipole B in the mirror BEC have a repulsive interaction, since they are standing side by side. The interaction between dipole A and C may have an attractive or repulsive interaction, depending how far out (in z-direction) dipole C is positioned. The farther they are apart, the more changes the character form side-by-side interaction to head-to-tail interaction. This changes the interaction sign. If the BEC is very long, contributions from the edges of the BEC cancel contributions form the center of the BEC, which reduces the overall interaction. The BEC has an optimal length when the interaction between the dipoles and the mirror dipoles is mainly repulsive. This optimal length corresponds to the maxima in the curves in Fig. 4.1.

and oscillation amplitudes x_s. The frequency shift is maximal for an aspect ratio of about $\nu = 2$. The reason for this is discussed in Ref. [54] and Ref. [55] and also depicted in Fig. 4.2, where it is discussed in the figure caption. The large amplitude corrections become significant for oscillation amplitudes that are of the order of the semi-axes $\lambda_x^{(0)}$. For $x_s = 0.25\,\lambda_x^{(0)}$ the corrections are still minor and become clearly visible for $x_s = 0.5\lambda_x^{(0)}$. A more thorough discussion of the results for the frequency shift follows after the column density model is presented.

4.1.2 Frequency shift based on the column density model

Since the method presented in the previous section relies on numerical methods to determine the frequency shift, there are still more simplifications necessary in order to get some analytical approximations. Such a simplification represents the column density $n_{1\mathrm{D}}(z) = n_0 \frac{\pi\lambda_x\lambda_y}{2}\left(1-\frac{z^2}{\lambda_z^2}\right)^2$, which was introduced in Sec. 3.2.2. In this section the column density is used as a model for the mirror BEC which generates the potential. Two different approaches are presented to calculate the frequency shift based on that. In the first approach the BEC itself is also modeled using the column density. The second approach represents a hybrid approach where the BEC is modeled by a three-dimensional TF ellipsoid and the mirror BEC by a column density model.

In both approaches the mirror potential $V_{\mathrm{mir}}^{(1\mathrm{D})}$, generated by the column density and which is given in Eq. (3.27), needs to be integrated over the BEC density distribution. In order to do that it is convenient to perform the variable shift

$$z'' = z - z' \Rightarrow z' = z - z''.$$

In order to improve the readability, the double primed variable is renamed to a single primed variable: $z'' \to z'$. Furthermore, the radial coordinate $r = \sqrt{x^2+y^2}$ is introduced. The expression for the mirror potential reads

$$V_{\mathrm{mir}}^{(1\mathrm{D})}(\mathbf{r}) = -\frac{g_D}{4\pi}\int_{-\lambda_z+z}^{\lambda_z+z} \mathrm{d}z'\, n_{1\mathrm{D}}(z'-z)\left(\frac{3z'^2}{\left(r^2+z'^2\right)^{5/2}} - \frac{1}{\left(r^2+z'^2\right)^{3/2}}\right). \tag{4.19}$$

The shifted column density distribution is a fourth order polynomial in z' which reads

$$n_{1\mathrm{D}}(z'-z) = n_0 \frac{\pi\lambda_x\lambda_y}{2}\sum_{k=0}^{4}\Gamma_k(z)\cdot z'^k, \tag{4.20}$$

where the coefficients $\Gamma_k(z)$ are defined by

$$\begin{aligned}
\Gamma_0(z) &= 1 - 2\frac{z^2}{\lambda_z^2} + \frac{z^4}{\lambda_z^4} = \left(1 - \frac{z^2}{\lambda_z^2}\right)^2, \\
\Gamma_1(z) &= 4\frac{z}{\lambda_z^2} - 4\frac{z^3}{\lambda_z^4}, \\
\Gamma_2(z) &= 6\frac{z^2}{\lambda_z^4} - \frac{2}{\lambda_z^2}, \\
\Gamma_3(z) &= -4\frac{z}{\lambda_z^4}, \\
\Gamma_4(z) &= \frac{1}{\lambda_z^4}.
\end{aligned}$$

The integrals that need to be solved are all of the form

$$C_k(\mathbf{r}) = \frac{1}{8\lambda_z} \int_{-\lambda_z+z}^{\lambda_z+z} \mathrm{d}z' \left(\frac{3z'^2}{(r^2+z'^2)^{5/2}} - \frac{1}{(r^2+z'^2)^{3/2}} \right) z'^k, \tag{4.21}$$

with $k \in \{0,1,2,3,4\}$. This type of integral can be solved analytically. The results are rather long and therefore omitted here.

Approach 1: Full column density model

Since in this approach it is assumed that the BEC density distribution is also given by a column density model, the problem reduces to the plane $y = 0$, where the column density resides. The radial coordinate becomes $r = x$. In this case the frequency shift is given by

$$\gamma^{(z)} = \frac{1}{2\omega_x^2 mN} \int_{-\lambda_z}^{\lambda_z} \mathrm{d}z\, n_{1\mathrm{D}}(z)\, 4\, \frac{\partial^2 V_{\mathrm{mir}}(x,z)}{\partial x^2}\bigg|_{x=2x_d}, \tag{4.22}$$

where the correction term for large amplitudes from expression (4.10) was dropped. The following discussion is restricted to the small amplitude case. The extension to large amplitudes is straightforward. The superscript (z) merely indicates the orientation of the dipoles. Using the integrals C_k given in (4.21) and expression (4.20) for the column density, the mirror potential

is written as

$$\begin{aligned} V_{\mathrm{mir}}^{(1\mathrm{D})}(x,z) &= -3\varepsilon_D^{(m)} g_s n_0 \varphi_{\mathrm{mir}}^{(1\mathrm{D})}(\mathbf{r}) \\ &= -3\varepsilon_D^{(m)} g_s n_0 \frac{1}{4\pi} \int \mathrm{d}z'\, \rho_{1\mathrm{D}}(z'-z) \left(\frac{3z'^2}{(x^2+z'^2)^{5/2}} - \frac{1}{(x^2+z'^2)^{3/2}} \right) \\ &= -3\varepsilon_D^{(m)} g_s n_0 \lambda_x \lambda_y \lambda_z \sum_{k=0}^{4} \Gamma_k(z)\, C_k(x,z) \end{aligned} \tag{4.23}$$

In the above expression the abbreviations $V_{\mathrm{mir}}(x,z) \equiv V_{\mathrm{mir}}(x,y=0,z)$ and $C_k(x,z) \equiv C_k(x,y=0,z)$ were used. With that the frequency shift reads

$$\gamma^{(z)} = -\frac{45}{16}\varepsilon_D^{(m)} \left[\lambda_x^{(0)}\right]^3 \lambda_y^{(0)} \frac{\lambda_z^{(0)}}{\lambda_z} \sum_{k=0}^{4} H_k^{(z)}(x_d, \lambda_z), \tag{4.24}$$

with

$$H_k^{(z)}(x_d,\lambda_z) = \int_{-\lambda_z}^{\lambda_z} \mathrm{d}z\, \Gamma_0(z)\, \Gamma_k(z)\, \left.\frac{\partial^2 C_k(x,z)}{\partial x^2}\right|_{x=2x_d}. \tag{4.25}$$

Result (4.24) is reached by using the expression for the central density (1.21), as well as TF semi axes (1.17). Furthermore the relation $n_{1\mathrm{D}}(z) = n_0 \frac{\pi\lambda_x\lambda_y}{2}\Gamma_0(z)$ was used. The derivatives of $C_k(x,z)$ are very long expression and therefore are not given here. Using software like *mathematica*, the derivatives are easily determined. Within this approach, all integrals can be solved analytically.

From the above given result one can see that the relative frequency shift only depends on the geometry of the setup, namely the TF semi axes and the distances to the surface. Besides that it also depends on the strength of the dipole-dipole interaction via the parameter $\varepsilon_D^{(m)}$. The parameter ε_D plays also a role, however, it is only a minor role. Depending on ε_D the length of the semi axis λ_z gets modified. This changes the value of $H_k^{(z)}(x_d,\lambda_z)$ and also the value of of $\lambda_z^{(0)}/\lambda_z$. Since λ_z as well as $\lambda_z^{(0)}$ go from 0 to ∞ as ν goes from 0 to ∞ both functions, $H_k^{(z)}(x_d,\lambda_z)$ as well as $H_k^{(z)}\left(x_d,\lambda_z^{(0)}\right)$, go through the same range of values. They are merely shifted relative to each other. This means that the position of the maximum is shifted. The strength of the frequency shift is modified via $\lambda_z^{(0)}/\lambda_z$. For the case that the dipoles are oriented in the z-direction the value of $\lambda_z^{(0)}/\lambda_z$ can be determined analytically for the limit $\nu \to \infty$, using the self-consistency equations (1.31). It is found to be $(1-\varepsilon_D)^{-1/5}$. However, given the fact that the frequency shift goes rapidly down as the aspect ratio increases (see Fig.

4.3), the precise value of $\lambda_z^{(0)}/\lambda_z$ is not very important. Using the column density model, it is actually possible to show that the frequency shift goes to zero for an infinitely elongated BEC. In the limit $\nu \to \infty$ also the semi axes λ_z goes to ∞. Using the analytical expressions for $H_k^{(z)}(x_d, \lambda_z)$, one finds the limit

$$\lim_{\lambda_z \to \infty} H_k^{(z)}(x_d, \lambda_z) = 0 \quad \forall k \in \{0, 1, 2, 3, 4\}.$$

Since $\lambda_z^{(0)}/\lambda_z$ goes to some finite value, the frequency shift vanishes.

Using the column density model also an estimate on the maximal possible frequency shift for a given distance x_d can be determined [54,55]. To do this, one first needs an estimate on the optimal length of the BEC. Consider a dipole in the center of the BEC at $z = 0$. In order for the interaction with all atoms in the mirror BEC to be repulsive, the semi axes λ_z of the mirror BEC may not exceed $\sqrt{2}x_d$, which in this case also determines the optimal length of the BEC. The frequency shift of a single atom in the center of the BEC is given by expression (4.24), where one simply drops the integration over $n_{1\mathrm{D}}$ and evaluates the expression at $z = 0$, which yields for a non-dipolar BEC ($\varepsilon_D = 0$) with $\lambda_z^{(0)} = \sqrt{2}x_d$ the frequency shift

$$\gamma_{\max}^{(z)} \approx 0.11 \frac{\left[\lambda_x^{(0)}\right]^4}{x_d^4} \varepsilon_D^{(m)}. \tag{4.26}$$

For the distance $x_d = 2\lambda_x^{(0)}$ this yields $\gamma_{\max}^{(z)} \approx 0.007\varepsilon_D^{(m)}$, i.e. for $\varepsilon_D^{(m)} = 0.15$ (^{52}Cr) on gets $\gamma_{\max}^{(z)} \approx 10^{-3}$ and for $\varepsilon_D^{(m)} = 0.5$ one gets $\gamma_{\max}^{(z)} \approx 3.5 \times 10^{-3}$. Comparison with Fig. 4.5a shows that this estimate is a bit too high, but is still gives a rough idea of the maximal frequency shift. Estimate (4.26) furthermore shows that the frequency shift becomes rapidly smaller as the ratio $x_d/\lambda_x^{(0)}$ increases. This is partly due to the fact that $\lambda_x^{(0)}$ is connected to the harmonic trap frequency. As $\lambda_x^{(0)}$ gets smaller, ω_x gets larger, which results in a smaller relative frequency shift. And if $\lambda_x^{(0)}$ remains constant and x_d is increased, the interaction gets simply weaker, which also reduces the frequency shift.

Approach 2: Hybrid model

This approach is basically identical to the approach presented in Section 4.1.1 for the three dimensional mirror BEC. The only difference is, that in expression (4.13), the mirror potential V_{mir} given in (3.24) is replaced by $V_{\mathrm{mir}}^{(1\mathrm{D})}$ given in (4.19).

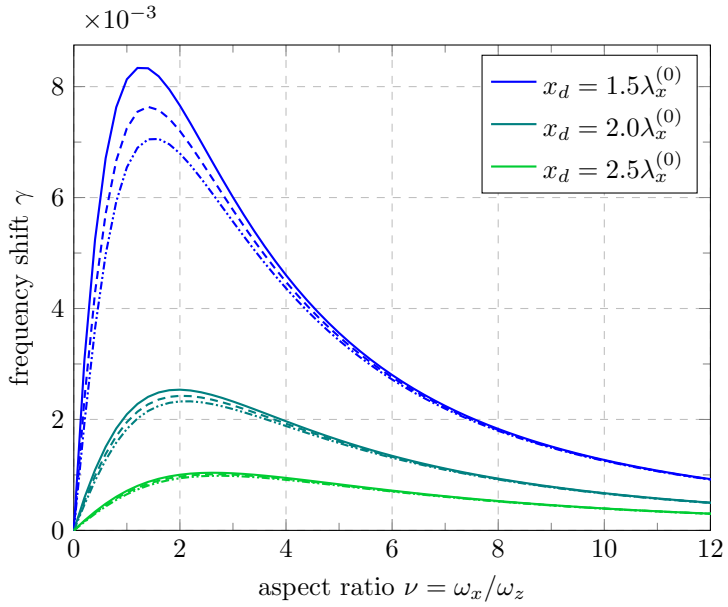

Figure 4.3: Frequency shift γ vs. trap aspect ratio $\nu = \omega_x/\omega_z$. The small amplitude approximation ($x_s = 0$) for a dipolar BEC with $\varepsilon_D = \varepsilon_D^{(m)} = 0.5$ is presented for three different distances $x_d = 1.5\lambda_x^{(0)}$, $x_d = 2\lambda_x^{(0)}$, and $x_d = 2.5\lambda_x^{(0)}$. The three dimensional TF results are indicated by a solid line, the full column density model (approach 1) by a dotted line, and the hybrid model (approach 2) by a dashed line.

This approach seems to be somewhat inconsistent, since the BEC is modeled by a TF ellipsoid and its mirror by a column density. However, the difference between the potential generated by the three dimensional mirror and the one dimensional mirror, at the position of the BEC, is only minor (as was shown in Fig. 3.2). To replace the three dimensional mean of the TF ellipsoid in (4.13) by a one dimensional integral along the axis of the column density, is only a good approximation if the variation of the potential (or to be more precise of its derivatives) over the extent of the BEC can be neglected. As it turns out, this is not quite the case.

In Fig. 4.3 the results of both approaches are compared to the results of the three dimensional TF model. As one would expect the results of the hybrid approach lay between the results of the full three dimensional and the full one-dimensional model. As the distance x_d gets larger, the three models converge. The three models also converge for very elongated BECs. This behavior can be easily understood: The more elongated the BEC gets

the better describes the column density model the actual three-dimensional BEC. And the larger the distance between BEC and superconductor the better is it possible to describe the interaction between mirror BEC and BEC by using column density models. The biggest difference between the three models appears around the position of the maximum, which lays between $\nu = 1$ and $\nu = 2$. In this region the BEC is not very elongated and has a more sphere like character, thus the column density is not a good approximation.

While the hybrid model does yield more accurate results than the column density model, the increased computational effort still does not seem justified. In order to get approximate analytical results the full one dimensional column density model is a very good tool. How well the three dimensional TF model compares to the numerical results is presented in the next section.

4.2 Numerical results for the frequency shift

In order to obtain the frequency shift from the numerical calculations, the center-of-mass motion needs to be analyzed. The BEC does not move in the y- and z-direction, so only the x-coordinate of the center of mass is of interest. The numerical calculation yields time curves of the expectation values, like for example the center-of-mass coordinate. A discrete Fourier transformation of the time data provides the frequency spectra. Since the frequency shift is expected to be rather small, it is necessary to perform a rather long time evolution. In the presented calculations the length of the time evolution is $t_{\mathrm{end}} = 10^4\, T_x$, with $T_x = 2\pi/\omega_x$. This translates to a frequency resolution of $\Delta\omega/\omega_x = 10^{-4}$. In order to determine the center-of-mass oscillation frequency, the mean frequency is calculated over a certain interval in the spectrum. It is clear that the peak in the spectrum is very close to ω_x, as is shown in Fig. 4.4. Therefore it is sufficient to consider a small interval $I = [\omega_x - \delta, \omega_x + \delta]$. Within this interval, all data points $\hat{\Omega}_i$ are summed up and weighed by the respective frequency Ω_i. Dividing the result by the sum of all $\hat{\Omega}_i$ in this interval, yields the mean frequency

$$\bar{\Omega} = \frac{\sum_{i\in I} \hat{\Omega}_i \cdot \Omega_i}{\sum_{i\in I} \hat{\Omega}_i}. \tag{4.27}$$

In Fig. 4.4 two example spectra are presented and the determined mean frequencies are indicated by vertical lines. The Fourier coefficients $\hat{\Omega}_i$ are normalized to the oscillation amplitude x_s. In Fig. 4.4 one of the peaks reaches roughly up to 1. The other peak is a bit smaller, since the actual

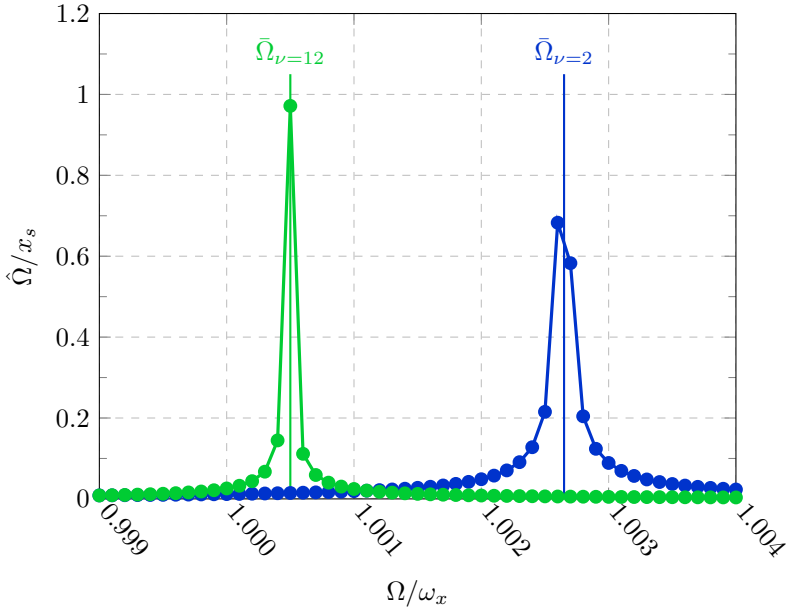

Figure 4.4: The frequency spectra for the x-coordinate of the center-of-mass motion. The GPE for a dipolar BEC with $\varepsilon_D = \varepsilon_D^{(m)} = 0.5$ was numerically solved for two different trap aspect ratios: $\nu = 2$ (blue) and $\nu = 12$ (green). The mean frequency $\bar{\Omega}$ given in (4.27) was calculated over an interval of the size $2\delta = 0.4\,\omega_x$. The resulting frequencies are $\bar{\Omega}_{\nu=2} = 1.00265\,\omega_x$ and $\bar{\Omega}_{\nu=12} = 1.0005\,\omega_x$. The frequency shift γ corresponding to these results is presented in Fig. 4.5b. *Parameters*: $\kappa = \omega_y/\omega_x = 1$, distance to surface $x_d = 2\lambda_x^{(0)}$, oscillation amplitude $x_s = 0.25\,\lambda_x^{(0)}$, length of the time evolution for the GPE: $t = 10^4\,T_x$, $\Delta t = 10^{-3}T_x$, with $T_x = 2\pi/\omega_x$, size of numerical lattice: $64 \times 64 \times 64$, expansion of the lattice: $6\lambda_x \times 6\lambda_y \times 6\lambda_z$, central density: $n_0^{(0)} = 2.5 \times 10^{13}\,\mathrm{cm}^{-3}$.

maximum position of the peak lays between two data points. The frequency shift connected with the mean frequency is given by $\gamma = \left(\bar{\Omega} - \omega_x\right)/\omega_x$. Fig. 4.5 shows the results for the frequency shift for different dipole interaction strengths and oscillation amplitudes. As a comparison, the results from the TF approximation are presented. The results obtained by the three dimensional TF approximation show an excellent agreement with the results from the GPE. Up to an amplitude of $x_s = 0.1\lambda_x^{(0)}$, shown in Fig. 4.5a, it is not necessary to calculate the large amplitude corrections in (4.10). For the larger amplitudes, presented in Fig. 4.5b, the correction term proportional to x_s^2 reproduces the change of the frequency shift very well. This demonstrates that the three dimensional TF model is an excellent tool to calculate the frequency shift, for small as well as for large amplitudes, very accurately. The column density model is useful for qualitative analysis of the behavior of the frequency shift and also to determine analytical approximations.

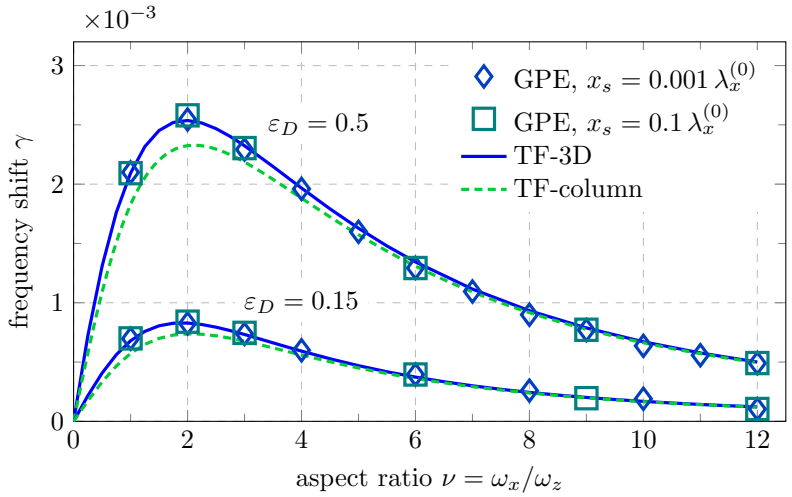

(a) GPE results for amplitudes $x_s = 0.001\lambda_x^{(0)}$ (diamonds) and $x_s = 0.1\lambda_x^{(0)}$ (squares) compared to small amplitude TF approximations.

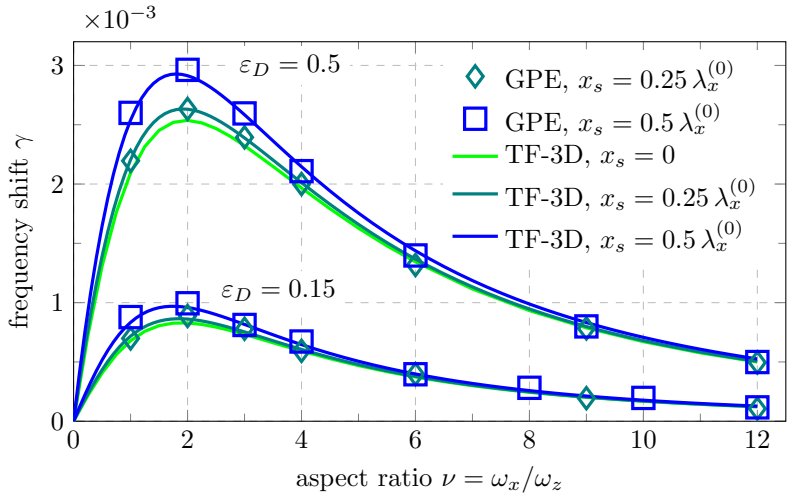

(b) GPE results for amplitudes $x_s = 0.25\lambda_x^{(0)}$ (diamonds) and $x_s = 0.5\lambda_x^{(0)}$ (squares) compared to TF approximations with large amplitude correction.

Figure 4.5: Frequency shift γ vs. trap aspect ratio $\nu = \omega_x/\omega_z$. Results from the numerical solution (data points) are compared to the results of the three dimensional TF model (solid lines) and the TF column density model (dashed lines). *Parameters*: $\kappa = \omega_y/\omega_x = 1$, distance to surface $x_d = 2\lambda_x^{(0)}$, length of the time evolution for the GPE: $t = 10^4\, T_x$, $\Delta t = 10^{-3} T_x$, with $T_x = 2\pi/\omega_x$, size of numerical lattice: $64 \times 64 \times 64$, expansion of the lattice: $6\lambda_x \times 6\lambda_y \times 6\lambda_z$, central density: $n_0^{(0)} = 2.5 \times 10^{13}\,\mathrm{cm}^{-3}$.

4.3 Frequency shift for different polarizations of the BEC

So far it was always assumed that the BEC is fully polarized in the z-direction, which is the direction of the long axis of the ellipsoid. Of course, the dipoles can be oriented in an arbitrary direction, given that it is technically possibly to apply a magnetic field in this direction. The relative orientation between the dipoles in the BEC and the mirror BEC affects the strength and also the interaction sign of the dipole-dipole interaction. Therefore, the polarization of the BEC also has an impact on the center-of-mass motion of the BEC.

Instead of discussing the most general case where the orientation is completely general, it is useful to investigate first the special cases. The first case that is presented, is the situation where the dipoles are all oriented in the y-direction. Meaning they remain parallel to the surface but are no longer facing along the long axis of the ellipsoid but perpendicular to it (see Fig. 4.6). Following that, the case that the dipoles are oriented perpendicular to the surface (see Fig. 4.9) is investigated. And finally, more general dipole orientations are discussed. It is always assumed that the BEC is 100% polarized. Furthermore, only small amplitude oscillations are considered. To account for corrections due to large amplitudes, one can apply the same method as was presented in Section 4.1.

The discussion of the frequency shift for the different polarizations is based completely on the column density model (approach 1 presented in Section 4.1.2). While the results may not be as good as the results from the three dimensional TF model, it is a good tool to investigate the general behavior and to find characteristic features.

4.3.1 Polarization in the y-direction

Let the magnetic dipoles of the atoms in the BEC all be oriented in the y-direction: $\boldsymbol{\mu}_\mathrm{d} = \mu_\mathrm{d} \cdot \hat{\mathbf{e}}_y$. The long axis of the BEC is oriented in the z-direction. This setup is depicted in Fig. 4.6. With that also the direction of the column density distribution is along the z-axis. The dipole-dipole interaction potential between two dipoles that are both oriented in y-direction is given by

$$U_\mathrm{md}\left(\mathbf{r}-\mathbf{r}'\right) = -\frac{g_D}{4\pi}\left(\frac{3\left(y-y'\right)^2}{\left|\mathbf{r}-\mathbf{r}'\right|^5} - \frac{1}{\left|\mathbf{r}-\mathbf{r}'\right|^3}\right), \tag{4.28}$$

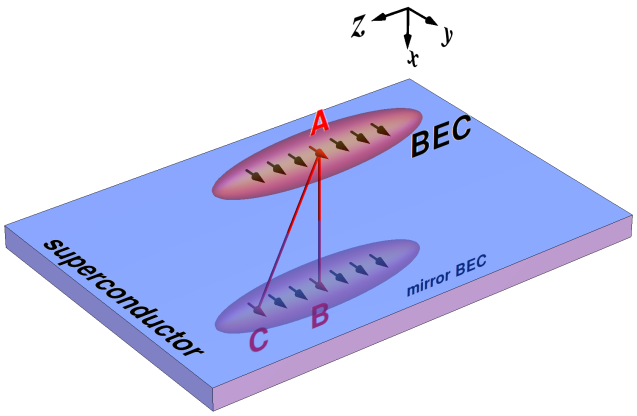

Figure 4.6: Schematic setup with the dipoles oriented in the y-direction. The interaction between the dipole A and dipole B is repulsive. The interaction between the dipole A and dipole C is also repulsive, independent of how far away on the z-axis the dipole C is located. The character of the interaction remains always side-by-side, thus the interaction sign does not change, merely the interaction strength decreases the farther apart the dipoles are.

as can be easily verified by inserting $\boldsymbol{\mu}_\mathrm{d} = \boldsymbol{\mu}'_\mathrm{d} = \mu_\mathrm{d} \cdot \hat{\mathbf{e}}_y$ in (1.8). In the chosen setup, the y-coordinate of the dipole position is always $y = y' = 0$. Furthermore it is convenient to chose the coordinate system such that $x' = 0$. This simplifies the dipole-dipole interaction potential considerably, which reduces to

$$U_\mathrm{md}\left(\mathbf{r} - \mathbf{r}'\right) = \frac{g_D}{4\pi} \frac{1}{\left[x^2 + \left(z - z'\right)^2\right]^{3/2}}. \tag{4.29}$$

From this already an important difference to the case where the dipoles are oriented in the z-direction can be seen. In this setup the sign of the dipole-dipole interaction potential does not change, no matter where the two interacting dipoles are located on the z-axis. For $\boldsymbol{\mu}_\mathrm{d} = \mu_\mathrm{d} \cdot \hat{\mathbf{e}}_z$ the dipole-dipole interaction sign changes as they move further apart on the z-axis, which was explained and depicted in Fig. 4.2.

The potential generated by the mirror BEC is given by

$$V_\mathrm{mir}^{(1\mathrm{D})}\left(x, z\right) = \frac{g_D}{4\pi} \int_{-\lambda_z}^{\lambda_z} \mathrm{d}z' \, \frac{n_{1\mathrm{D}}\left(z'\right)}{\left[x^2 + \left(z - z'\right)^2\right]^{3/2}}. \tag{4.30}$$

To calculate the frequency shift, the same approach as in Sec. 4.1.2 is used: First the z-coordinate is shifted, then expression (4.20) is inserted for $n_{1\mathrm{D}}(z'-z)$, which yields for the mirror potential

$$V_{\mathrm{mir}}^{(1\mathrm{D})}(\mathbf{r}) = 3\varepsilon_D^{(m)} g_s n_0 \lambda_x \lambda_y \lambda_z \sum_{k=0}^{4} \Gamma_k(z)\, D_k(x,z)\,, \tag{4.31}$$

with

$$D_k(x,z) = \frac{1}{8\lambda_z} \int_{-\lambda_z+z}^{\lambda_z+z} \mathrm{d}z' \, \frac{z'^k}{\left(x^2+z'^2\right)^{3/2}}. \tag{4.32}$$

The expression for the frequency shift reads

$$\gamma^{(y)} = \frac{45}{16}\varepsilon_D^{(m)} \left[\lambda_x^{(0)}\right]^3 \lambda_y^{(0)} \frac{\lambda_z^{(0)}}{\lambda_z} \sum_{k=0}^{4} H_k^{(y)}(x_d, \lambda_z)\,. \tag{4.33}$$

with

$$H_k^{(y)}(x_d,\lambda_z) = \int_{-\lambda_z}^{\lambda_z} \mathrm{d}z\, \Gamma_0(z)\, \Gamma_k(z)\, \left.\frac{\partial^2 D_k(x,z)}{\partial x^2}\right|_{x=2x_d}. \tag{4.34}$$

The case $\varepsilon_D = 0$

From (4.29) it is clear that the interaction sign between each dipole in the BEC with each dipole in the mirror BEC has the same sign. This means that the overall interaction becomes stronger as the number of atoms is increased. Therefore $\gamma^{(y)}$ is expected to be a function that monotonically increases with N. Just like before, the number of atoms is increased in such a way that the central density $n_0^{(0)}$ remains constant for all N. Again, the aspect ratio ν is used rather then the number of atoms N. In Fig. 4.7, the frequency shift $\gamma^{(y)}$ is presented as a function of the trap ratio ν. The frequency shift rapidly increases for small values of ν and then quickly saturates. To see if that is actually the case, the limit $\nu \to \infty$ needs to be determined. This means that $\lambda_z^{(0)} \to \infty$, while $n_0^{(0)} = \text{const.}$, $\lambda_x^{(0)} = \text{const.}$, and $\lambda_y^{(0)} = \text{const.}$:

$$\gamma_{\max}^{(y)} = \lim_{\lambda_z^{(0)}\to\infty} \gamma^{(y)} = \frac{45\varepsilon_D^{(m)}}{16} \left[\lambda_x^{(0)}\right]^3 \lambda_y^{(0)} \sum_{k=0}^{4} \lim_{\lambda_z^{(0)}\to\infty} H_k^{(y)}\left(x_d, \lambda_z^{(0)}\right), \tag{4.35}$$

Although $H_k^{(y)}$ can be calculated analytically, here only the limiting value of $H_k^{(y)}$ is presented:

$$\lim_{\lambda_z^{(0)}\to\infty} H_0^{(y)}\left(x_d, \lambda_z^{(0)}\right) = \frac{8}{105}\frac{1}{x_d^4}, \tag{4.36}$$

and

$$\lim_{\lambda_z^{(0)}\to\infty} H_k^{(y)}\left(x_d, \lambda_z^{(0)}\right) = 0, \quad \text{for} \quad k = \{1,2,3,4\}\,. \tag{4.37}$$

For a cylindrically symmetric trap with $\lambda_x^{(0)} = \lambda_y^{(0)}$, the expression for the maximal frequency shift takes the guise

$$\gamma_{\max}^{(y)} = \frac{3}{14}\varepsilon_D^{(m)}\left[\frac{\lambda_x^{(0)}}{x_d}\right]^4. \tag{4.38}$$

This value represents the largest possible frequency shift that can be achieved for this dipole orientation. A comparison of the maximal value for the case that the dipoles are oriented in the z-direction, given in (4.26), shows that $\gamma_{\max}^{(y)}$ is roughly by a factor of two larger. However, making this comparison, one needs to bare in mind that $\gamma_{\max}^{(z)}$ is merely an estimate, while $\gamma_{\max}^{(y)}$ is the exact limit of the column density model. Nevertheless, the comparison is useful and shows that in terms of the strength of the effect, a dipole orientation in the y-direction is advantageous.

The case $\varepsilon_D \neq 0$

For the case that $\varepsilon_D \neq 0$, the expression for the maximal frequency shift reads

$$\gamma_{\max}^{(y)} = \lim_{\nu\to\infty}\gamma^{(y)} = \frac{45\varepsilon_D^{(m)}}{16}\left[\lambda_x^{(0)}\right]^3\lambda_y^{(0)}\sum_{k=0}^{4}\lim_{\nu\to\infty}\frac{\lambda_z^{(0)}}{\lambda_z}H_k^{(y)}\left(x_d,\lambda_z\right).$$

The limit of the function $H_k^{(y)}$ is given by $\lim_{\lambda_z\to\infty} H_k^{(y)}\left(x_d,\lambda_z\right)$. The results are the same as before and are given in (4.36) and (4.37). Assuming a cylindrical symmetric trap, the maximal frequency shift reads

$$\gamma_{\max}^{(y)} = \frac{3}{14}\varepsilon_D^{(m)}\left[\frac{\lambda_x^{(0)}}{x_d}\right]^4\lim_{\nu\to\infty}\frac{\lambda_z^{(0)}}{\lambda_z}. \tag{4.39}$$

The modification of the frequency shift due to $\varepsilon_D \neq 0$ is given by the factor $\lim_{\nu\to\infty}\frac{\lambda_z^{(0)}}{\lambda_z}$. The value of this can be determined with the help of the self-consistency equations (1.31) for the BEC semi axes. Unfortunately it is not possible to give a closed expression for this factor. The reason is that the BEC is a tri-axial ellipsoid with $\lambda_x \neq \lambda_y \neq \lambda_z$, even though the trap is symmetrical and with that also $\lambda_x^{(0)} = \lambda_y^{(0)}$. But the symmetry is broken since the dipoles are oriented in the y-direction and not in the z-direction.

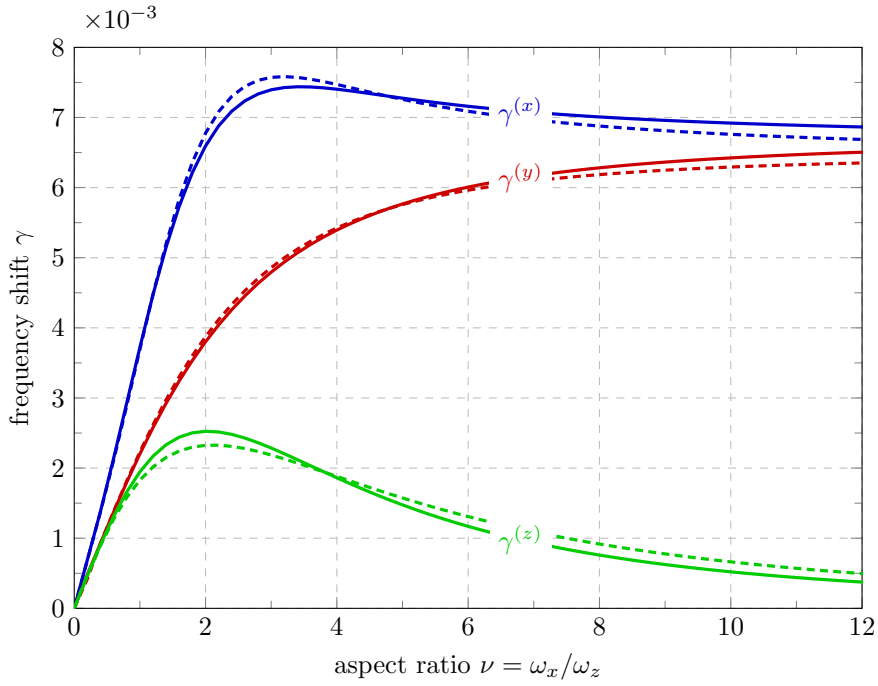

Figure 4.7: Frequency shift γ vs. trap aspect ratio $\nu = \omega_x/\omega_z$. The frequency shift is calculated using the column density model for $\varepsilon_D^{(m)} = 0.5$, for a non-dipolar BEC with $\varepsilon_D = 0$ (dashed lines) and a dipolar BEC with $\varepsilon_D = \varepsilon_D^{(m)}$ (solid lines). Three different polarizations of the BEC are presented: $\boldsymbol{\mu}_\mathrm{d} = \mu_\mathrm{d}\hat{\mathbf{e}}_x$ (blue), $\boldsymbol{\mu}_\mathrm{d} = \mu_\mathrm{d}\hat{\mathbf{e}}_y$ (red), and $\boldsymbol{\mu}_\mathrm{d} = \mu_\mathrm{d}\hat{\mathbf{e}}_z$ (green). The distance between harmonic trap minimum and surface is $x_d = 2\lambda_x^{(0)}$.

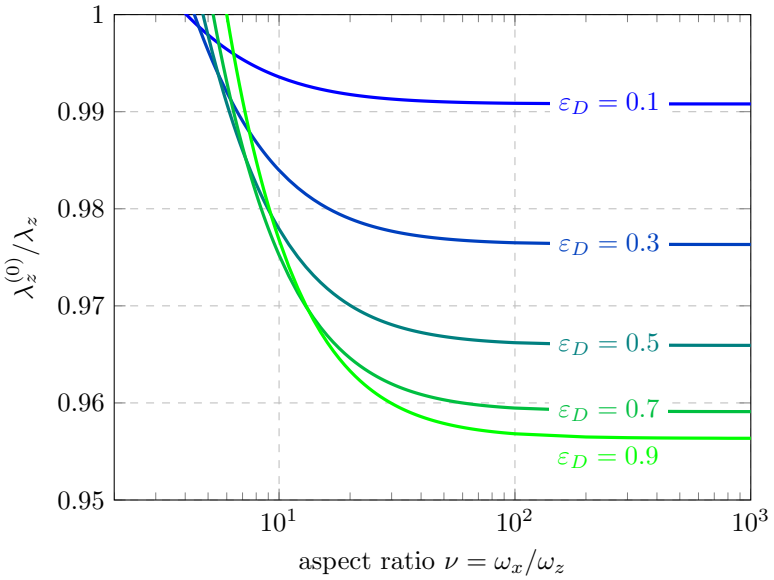

Figure 4.8: The factor $\lambda_z^{(0)}/\lambda_z$ vs. the trap aspect ratio $\nu = \omega_x/\omega_z$ in a uniaxial trap with $\kappa = \omega_y/\omega_x = 1$. The dipoles are oriented in the y-direction. The curves correspond to different values of the interaction parameter ε_D: from $\varepsilon_D = 0.1$ to $\varepsilon_D = 0.9$ in steps of 0.2.

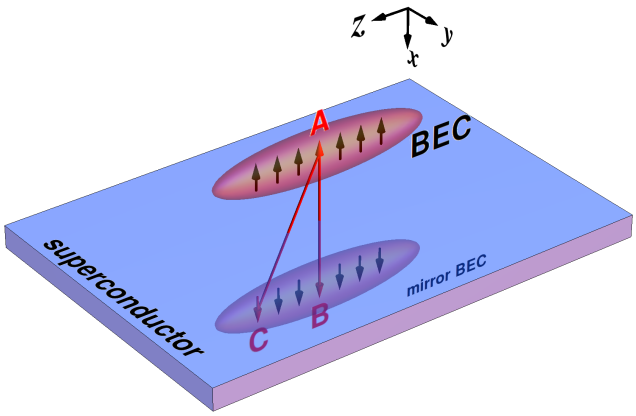

Figure 4.9: Schematic depiction of the setup with the dipoles oriented in the x-direction. The interaction between dipole A and dipole B is repulsive, since they are facing each other tail-to-tail (or head-to-head if they are oriented in the opposite direction). The interaction sign between A and C depends on how far apart the two dipoles are. If they are close, the interaction has mainly a tail-to-tail (or head-to-head) like character. The further apart they are, the more changes the interaction to side-by-side with opposite facing dipoles. This means the interaction gets attractive and the interaction sign changes. If the BEC is long enough, contributions from the edges cancel contributions from the center. Thus there is an optimal length of the BEC, where the interaction is maximal.

In Fig. 4.8 the factor $\lambda_z^{(0)}/\lambda_z$ is presented as a function of ν. It shows that the modification due to the shape deformation is not too drastic. Even for large values of ε_D the corrections are below five percent. Also the curves for $\gamma^{(y)}$ in Fig. 4.7 show that the results for $\varepsilon_D = 0$ and $\varepsilon_D = \varepsilon_D^{(m)}$ are very similar.

4.3.2 Polarization in the x-direction (perpendicular to the surface)

Assume that the polarization of the BEC is along the x-axis, which is perpendicular to the surface (see Fig. 4.9).

There are two possibilities to orient the dipoles: $\boldsymbol{\mu}_\mathrm{d} = \pm\mu_\mathrm{d} \cdot \hat{\mathbf{e}}_x$. The magnetic mirror dipoles are oriented in the exact opposite direction $\boldsymbol{\mu}'_\mathrm{d} = \mp\mu_\mathrm{d} \cdot \hat{\mathbf{e}}_x$. Either way the interaction potential between the dipoles and the

mirror dipoles is given by

$$U_{\mathrm{md}}\left(\mathbf{r}-\mathbf{r}'\right)=\frac{g_D}{4\pi}\left(\frac{3\left(x-x'\right)^2}{\left|\mathbf{r}-\mathbf{r}'\right|^5}-\frac{1}{\left|\mathbf{r}-\mathbf{r}'\right|^3}\right). \tag{4.40}$$

Using the column density model, only the potential within the plane $y=0$ is of interest. Again, the mirror BEC is positioned at $x'=0$. The dipole-dipole interaction potential reads

$$U_{\mathrm{md}}\left(\mathbf{r}-\mathbf{r}'\right)=\frac{g_D}{4\pi}\left(\frac{3x^2}{\left[x^2+\left(z-z'\right)^2\right]^{5/2}}-\frac{1}{\left[x^2+\left(z-z'\right)^2\right]^{3/2}}\right). \tag{4.41}$$

This expression looks similar to potential (1.9), where the dipoles are oriented in the z-direction. Depending in the relative position of the interacting dipoles, this expression is either positive or negative. Within the column density model the frequency shift reads

$$\gamma^{(x)}=\frac{45\varepsilon_D^{(m)}}{16}\left[\lambda_x^{(0)}\right]^3\lambda_y^{(0)}\frac{\lambda_z^{(0)}}{\lambda_z}\sum_{k=0}^{4}H_k^{(x)}\left(x_d,\lambda_z\right), \tag{4.42}$$

with

$$H_k^{(x)}\left(x_d,\lambda_z\right)=\int_{-\lambda_z}^{\lambda_z}\mathrm{d}z\,\Gamma_0\left(z\right)\Gamma_k\left(z\right)\left.\frac{\partial^2 G_k\left(x,z\right)}{\partial x^2}\right|_{x=2x_d} \tag{4.43}$$

and

$$G_k\left(x,z\right)=\frac{1}{8\lambda_z}\int_{-\lambda_z+z}^{\lambda_z+z}\mathrm{d}z'\left(\frac{3x^2}{\left[x^2+z'^2\right]^{5/2}}-\frac{1}{\left[x^2+z'^2\right]^{3/2}}\right)z'^k. \tag{4.44}$$

Fig. 4.7 shows the frequency shift $\gamma^{(x)}$ as a function of the aspect ratio ν. Similar to $\gamma^{(z)}$, the curve shows a maximum. However, this maximum is not particularly pronounced. The frequency shift decreases only slightly and does not drop to zero. Instead it appears to approach some finite value. Similar as in the case where the dipoles are oriented in the z-direction, dipoles A and B here also have a repulsive interaction (compare Fig. 4.9 and Fig. 4.2). However, an important difference is that the dipoles are facing each other head to head (or tail to tail), which increases the interaction strength by a factor of 2 compared to the side by side case. This is easily seen from the dipole-dipole potential. In the head to head case with $\boldsymbol{\mu}_{\mathrm{d}}=\mu_{\mathrm{d}}\cdot\hat{\mathbf{e}}_x$,

$\boldsymbol{\mu}'_{\mathrm{d}} = -\mu_{\mathrm{d}} \cdot \hat{\mathbf{e}}_x$, and $\mathbf{r} - \mathbf{r}' = d \cdot \hat{\mathbf{e}}_x$ the potential reads $U_{\mathrm{md}} = \frac{g_D}{4\pi} \frac{2}{d^3}$, while for $\boldsymbol{\mu}_{\mathrm{d}} = \boldsymbol{\mu}'_{\mathrm{d}} = \mu_{\mathrm{d}} \cdot \hat{\mathbf{e}}_z$ and $\mathbf{r} - \mathbf{r}' = d \cdot \hat{\mathbf{e}}_x$ the potential reads $U_{\mathrm{md}} = \frac{g_D}{4\pi} \frac{1}{d^3}$. The potential is by a factor of 2 stronger so that also the scale of the frequency shift should be increased by a factor of 2. Also, with the dipoles oriented in the x-direction, the optimal length of the BEC is $\lambda_z \approx 2\sqrt{2} x_d$, which is twice the optimal length for the case that they are oriented in the z-direction. In Fig. 4.7 one can see that the linear increase for small ν of $\gamma^{(x)}$ is roughly twice as large as $\gamma^{(z)}$. This is due to the increased interaction strength. Furthermore, one can see that the maximum of $\gamma^{(x)}$ appears at a larger trap aspect ratio compared to the maximum of $\gamma^{(z)}$. There are two reasons why $\gamma^{(x)}$ does not drop to zero. First, the contributions from the edges of the BEC have a mainly side-by-side character, which is weaker than the contributions from the central region which have a head-to-head character. Second, the optimal length of the BEC has increased compared to the optimal length for $\gamma^{(z)}$. This means that the compensating contributions from the edges are very weak due to the large distance. Using the analytical results for $H_k^{(x)}$, the limit $\nu \to \infty$ is found to be

$$\gamma_{\max}^{(x)} = \lim_{\nu \to \infty} \gamma^{(x)} = \frac{45 \varepsilon_D^{(m)}}{16} \left[\lambda_x^{(0)}\right]^3 \lambda_y^{(0)} \lim_{\nu \to \infty} \frac{\lambda_z^{(0)}}{\lambda_z} \sum_{k=0}^{4} H_k^{(x)} \left(x_d, \lambda_z\right).$$

In Fig. 4.8 the factor $\lim_{\nu \to \infty} \frac{\lambda_z^{(0)}}{\lambda_z}$ was already presented. This leaves the function $H_k^{(x)}\left(x_d, \lambda_z\right)$, where the limit reads

$$\lim_{\nu \to \infty} H_0^{(x)}\left(x_d, \lambda_z\right) = \lim_{\lambda_z \to \infty} H_0^{(x)}\left(\lambda_z, x_d\right) = \frac{8}{105} \frac{1}{x_d^4}, \tag{4.45}$$

and

$$\lim_{\lambda_z \to \infty} H_k^{(x)}\left(x_d, \lambda_z\right) = 0, \quad \text{for} \quad k \in \{1, 2, 3, 4\}. \tag{4.46}$$

It is interesting to note that $\gamma_{\max}^{(x)}$ is equal to $\gamma_{\max}^{(y)}$.

4.3.3 Arbitrary polarization

Say the polarizing magnetic field is applied in an arbitrary direction so that the magnetic dipoles are given by

$$\boldsymbol{\mu}_{\mathrm{d}} = \mu_{\mathrm{d}} \left(\mu_x \hat{\mathbf{e}}_x + \mu_y \hat{\mathbf{e}}_y + \mu_z \hat{\mathbf{e}}_z\right), \tag{4.47}$$

with $\mu_x^2+\mu_y^2+\mu_z^2=1$. A possible parametrization is given by the standard spherical coordinates

$$\begin{aligned}\mu_x &= \sin\vartheta_B\cos\varphi_B,\\ \mu_y &= \sin\vartheta_B\sin\varphi_B,\\ \mu_z &= \cos\vartheta_B.\end{aligned}$$

Next, the interaction potential between an atom in the BEC and an atom in the mirror BEC is needed. If the dipole $\boldsymbol{\mu}_{\rm d}$ is given by (4.47), the mirror dipole reads

$$\boldsymbol{\mu}'_{\rm d}=\mu_{\rm d}\left(-\mu_x\hat{\mathbf{e}}_x+\mu_y\hat{\mathbf{e}}_y+\mu_z\hat{\mathbf{e}}_z\right). \tag{4.48}$$

With $y=y'=0$ and $x'=0$, the interaction potential between those two dipoles is given by

$$\begin{aligned}U_{\rm md}\left(\mathbf{r}-\mathbf{r}'\right) &= -\frac{g_D}{4\pi}\left\{\frac{3\left[\mu_x x+\mu_z\left(z-z'\right)\right]\left[-\mu_x x+\mu_z\left(z-z'\right)\right]}{\left|\mathbf{r}-\mathbf{r}'\right|^5}-\frac{\left(-\mu_x^2+\mu_y^2+\mu_z^2\right)}{\left|\mathbf{r}-\mathbf{r}'\right|^3}\right\}\\ &= -\frac{g_D}{4\pi}\left\{\frac{3\left[-\mu_x^2x^2+\mu_z^2\left(z-z'\right)^2\right]}{\left|\mathbf{r}-\mathbf{r}'\right|^5}-\frac{\left(-\mu_x^2+\mu_y^2+\mu_z^2\right)}{\left|\mathbf{r}-\mathbf{r}'\right|^3}\right\}\\ &= \mu_x^2\frac{g_D}{4\pi}\left\{\frac{3x^2}{\left|\mathbf{r}-\mathbf{r}'\right|^5}-\frac{1}{\left|\mathbf{r}-\mathbf{r}'\right|^3}\right\}\\ &\quad+\mu_y^2\frac{g_D}{4\pi}\frac{1}{\left|\mathbf{r}-\mathbf{r}'\right|^3}\\ &\quad-\mu_z^2\frac{g_D}{4\pi}\left\{\frac{3\left(z-z'\right)^2}{\left|\mathbf{r}-\mathbf{r}'\right|^5}-\frac{1}{\left|\mathbf{r}-\mathbf{r}'\right|^3}\right\}.\end{aligned}$$

This shows that the potential is simply a superposition of the three special cases that were already discussed. The resulting frequency shift is immediately written down as

$$\begin{aligned}\gamma &= \mu_x^2\gamma^{(x)}+\mu_y^2\gamma^{(y)}+\mu_z^2\gamma^{(z)}\\ &= \gamma^{(x)}\sin^2\vartheta_B\cos^2\varphi_B+\gamma^{(y)}\sin^2\vartheta_B\sin^2\varphi_B+\gamma^{(z)}\cos^2\vartheta_B.\end{aligned} \tag{4.49}$$

The angles φ_B and ϑ_B define the orientation of the external polarizing magnetic field relative to the axes of the harmonic trap. Expression (4.49) holds only for the case $\varepsilon_D=0$. For $\varepsilon_D=\varepsilon_D^{(m)}$ the situation becomes more complicated. The modification of the BEC shape needs to be considered, which was done for the special cases and shown that the influence on the

frequency shift is moderate. For a more general orientation of the dipoles there is another effect that also needs to be considered. The orientation of the TF ellipsoid itself is modified. It is no longer true that the directions defined by the harmonic trap coincide with directions of the semi axes of the TF ellipsoid [57]. This tilt of the BEC has also an influence on the frequency shift and needs to be discussed.

In the following, the dipole orientation is not completely arbitrary as in (4.49). First an arbitrary dipole orientation parallel to the surface is presented. Afterward the cases where the dipoles are oriented in the x-y- and x-z-plane is presented.

Polarization in the y-z-plane (parallel to the surface)

The case $\varepsilon_D = 0$: If the dipoles are oriented parallel to the surface, the orientation angle φ_B is fixed by $\varphi_B = \pi/2$. Expression (4.49) for the frequency shift reduces to

$$\gamma^{(yz)} = \gamma^{(y)} \sin^2 \vartheta_B + \gamma^{(z)} \cos^2 \vartheta_B. \tag{4.50}$$

In Fig. 4.10 the frequency shift is presented for various orientation angles ϑ_B as function of the trap ratio ν and in Fig. 4.11 the frequency shift is given as a function of ϑ_B for various aspect ratios of the trap. In both cases the trap is cylindrically symmetric with $\kappa = \omega_y/\omega_x = 1$. In the limit $\lambda_z^{(0)} \to \infty$ the frequency shift is given by

$$\gamma_\infty^{(yz)} = \frac{3}{14} \varepsilon_D^{(m)} \left[\frac{\lambda_x^{(0)}}{x_d} \right]^4 \sin^2 \vartheta_B. \tag{4.51}$$

This gives a characteristic dependence of the frequency shift on the orientation angle ϑ_B. This characteristic serves as another fingerprint of the eddy current effect, which can experimentally be used to distinguish it from other possible influences of the surface on the center-of-mass motion.

The case $\varepsilon_D = \varepsilon_D^{(m)}$: The modification of the frequency shift due the BEC shape is again given by the factor $\lambda_z^{(0)}/\lambda_z$. Besides the trap aspect ratios, the factor now also depends on the orientation angle ϑ_B (see Fig. 4.12). The reorientation of the TF ellipsoid is depicted in Fig. 4.13. The frame of reference defined by the harmonic trap and the frame of reference defined by the TF ellipsoid coincide for the case that $\vartheta_B = 0$ or $\vartheta_B = \pi/2$. For $0 < \vartheta_B < \pi/2$, this is no longer the case. The BEC is tilted in the y-z-plane. Say an external polarizing field is applied in a direction defined by the angle ϑ_B between the field and the z-axis of the trap. The z-axis

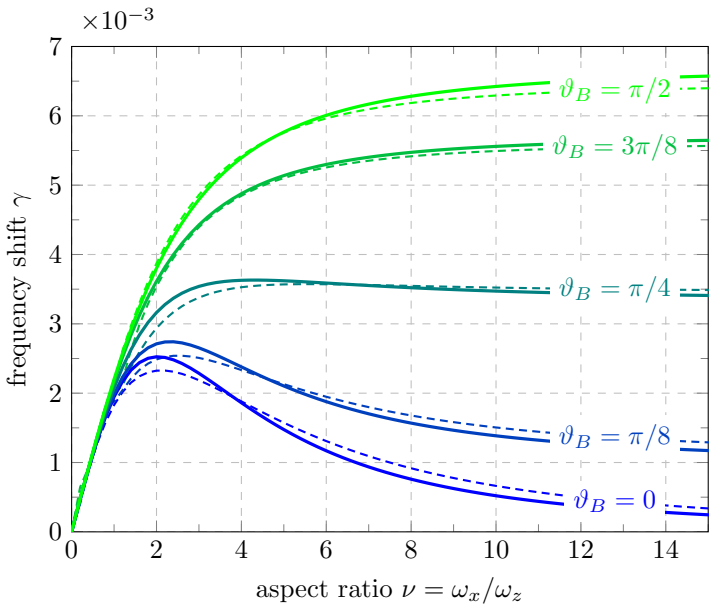

Figure 4.10: Frequency shift $\gamma^{(yz)}$ vs. trap aspect ratio $\nu = \omega_x/\omega_z$. The frequency shift is calculated using the column density model for $\varepsilon_D^{(m)} = 0.5$, for a non-dipolar BEC with $\varepsilon_D = 0$ (solid lines) and a dipolar BEC with $\varepsilon_D = \varepsilon_D^{(m)}$ (dashed lines). The BEC polarization changes from $\vartheta_B = 0$ (dipoles in z-direction) in steps of $\pi/8$ to $\vartheta_B = \pi/2$ (dipoles in y-direction). The second orientation angle is set to $\varphi_B = \pi/2$ and the distance to the surface is $x_d = 2\lambda_x^{(0)}$.

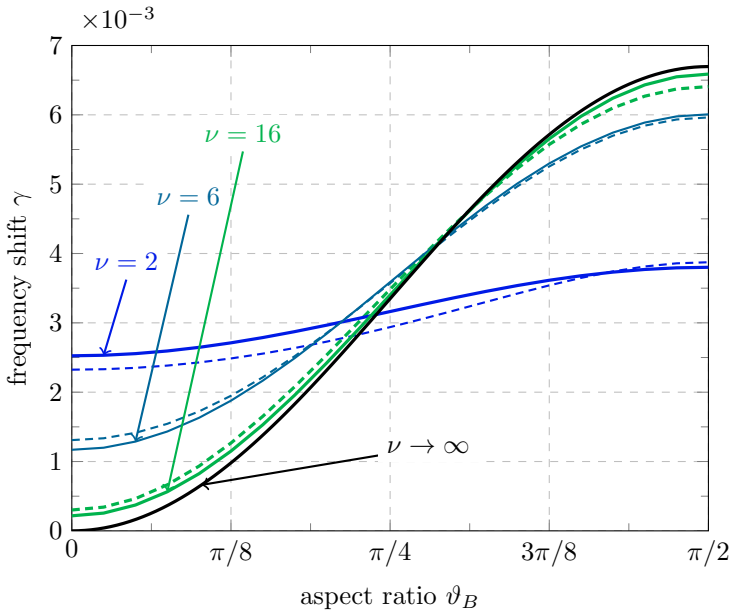

Figure 4.11: Frequency shift $\gamma^{(yz)}$ vs. orientation angle ϑ_B. The frequency shift is calculated using the column density model for $\varepsilon_D^{(m)} = 0.5$, for a non-dipolar BEC with $\varepsilon_D = 0$ (solid lines) and a dipolar BEC with $\varepsilon_D = \varepsilon_D^{(m)}$ (dashed lines). The results are shown for three different trap aspect ratios $\nu = \omega_x/\omega_z$. The black line shows approximation (4.51) for a non-dipolar BEC with $\varepsilon_D = 0$. The second orientation angle is set to $\varphi_B = \pi/2$ and the distance to the surface is $x_d = 2\lambda_x^{(0)}$.

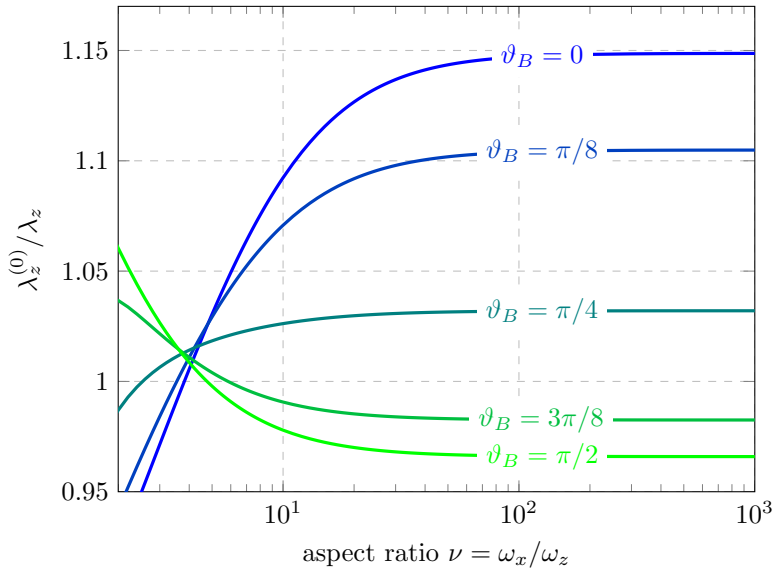

Figure 4.12: The factor $\lambda_z^{(0)}/\lambda_z$ vs. the trap aspect ratio $\nu = \omega_x/\omega_z$ in a uni-axial trap with $\kappa = \omega_y/\omega_x = 1$. The curves correspond to different orientation angles ϑ_B: from $\vartheta_B = 0$ (dipoles in z-direction) to $\vartheta_B = \pi/2$ (dipoles in x-direction for $\varphi_B = 0$ or dipoles in y-direction for $\varphi_B = \pi/2$) in steps of $\pi/8$. The dipole-dipole interaction parameter is fairly large: $\varepsilon_D = 0.5$. The dipoles are rotated form the axial into the radial direction of the BEC. The orientation angles are defined in Section 4.3.3

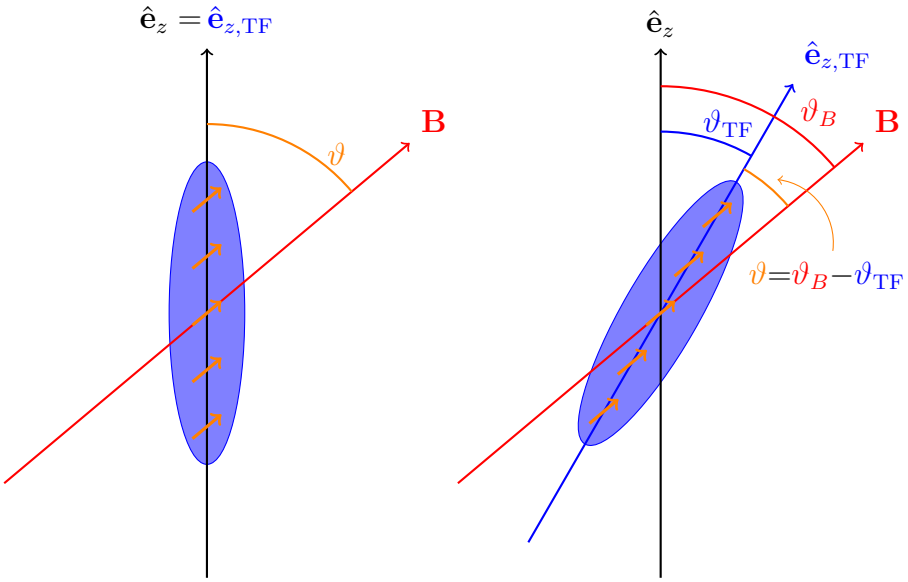

Figure 4.13: Schematic depiction of the reorientation of the TF ellipsoid in the y-z-plane. The left panel shows the situation for $\varepsilon_D = 0$. The dipoles are oriented in the direction of the applied **B**-field. The orientation of the ellipsoid is not affected. The angle ϑ between the dipoles and the ellipsoid is equal to the angle ϑ_B between the **B**-field and the ellipsoid. The right panel shows the situation for a BEC with $\varepsilon_D = \varepsilon_D^{(m)}$. The z-axis of the TF ellipsoid ($\hat{\mathbf{e}}_{z,\mathrm{TF}}$) is rotated by an angle ϑ_{TF} away from the z-axis of the trap ($\hat{\mathbf{e}}_z$). The new angle between the dipoles and the TF ellipsoid is $\vartheta = \vartheta_B - \vartheta_{\mathrm{TF}}$.

of the BEC is oriented in a direction defined by the angle ϑ_{TF} and the angle ϑ is given by $\vartheta = \vartheta_{\mathrm{TF}} - \vartheta_B$. It is clear that expression (4.49) for the frequency shift needs to be replaced by

$$\gamma^{(yz)} = \gamma^{(y)} \sin^2 \vartheta + \gamma^{(z)} \cos^2 \vartheta. \tag{4.52}$$

The angle ϑ_{TF} is determined by the set of self-consistency equations (1.31). The dashed curves in Fig. 4.10 and Fig. 4.11 show the frequency shift for $\varepsilon_D = \varepsilon_D^{(m)}$. One can see that the curves are somewhat distorted compared to the case $\varepsilon_D = 0$. However, the basic shape of the curves is mainly the same and the corrections due to $\varepsilon_D = \varepsilon_D^{(m)}$ are only minor.

Polarization in the x-y-plane

The case $\varepsilon_D = 0$: The orientation angle ϑ_B is fixed by $\vartheta_B = \pi/2$, which yields the frequency shift

$$\gamma^{(xy)} = \gamma^{(x)} \cos^2 \varphi_B + \gamma^{(y)} \sin^2 \varphi_B. \tag{4.53}$$

As usual, the starting point is the case $\varepsilon_D = 0$. The results for the frequency shift are presented in Fig. 4.14 and Fig. 4.15. The limit of an infinitely long BEC in the z-direction is given by

$$\gamma_\infty^{(xy)} = \frac{3}{14} \varepsilon_D^{(m)} \left[\frac{\lambda_x^{(0)}}{x_d} \right]^4 . \tag{4.54}$$

The case $\varepsilon_D = \varepsilon_D^{(m)}$: The effect of the dipole-dipole interaction in this case is limited to the modification of the semi axes. At least for a cylindrically symmetric trap with $\kappa = \omega_y/\omega_x = 1$. For a slightly asymmetric trap, the tilt of the BEC in the x-y-plane can be neglected. Especially within the column density model this does not affect the frequency shift. The modified semi-axes lead again to the factor of $\lim_{\nu\to\infty} \lambda_z^{(0)}/\lambda_z$, which was already discussed previously and the factor is given in Fig. 4.12. For $\kappa = 1$ and $\vartheta_B = \pi/2$, the angle φ_B does not have an influence on $\lim_{\nu\to\infty} \lambda_z^{(0)}/\lambda_z$.

Polarization in the x-z-plane

The case $\varepsilon_D = 0$: The orientation angle φ_B is fixed by $\varphi_B = 0$ and the frequency shift is given by

$$\gamma^{(xz)} = \gamma^{(x)} \sin^2 \vartheta_B + \gamma^{(z)} \cos^2 \vartheta_B. \tag{4.55}$$

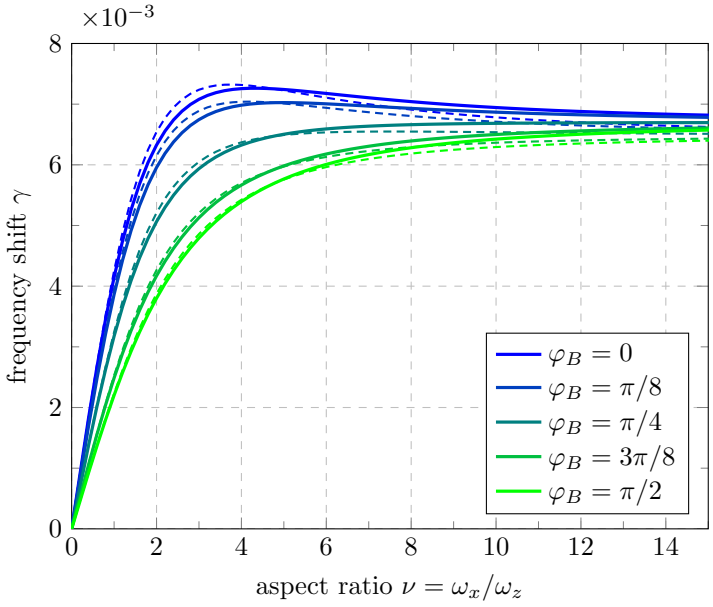

Figure 4.14: Frequency shift $\gamma^{(xy)}$ vs. trap aspect ratio $\nu = \omega_x/\omega_z$. The frequency shift is calculated using the column density model for $\varepsilon_D^{(m)} = 0.5$, for a non-dipolar BEC with $\varepsilon_D = 0$ (solid lines) and a dipolar BEC with $\varepsilon_D = \varepsilon_D^{(m)}$ (dashed lines). The BEC polarization changes from $\varphi_B = 0$ (dipoles in x-direction) in steps of $\pi/8$ to $\varphi_B = \pi/2$ (dipoles in y-direction). The second orientation angle is set to $\vartheta_B = \pi/2$ and the distance to the surface is $x_d = 2\lambda_x^{(0)}$.

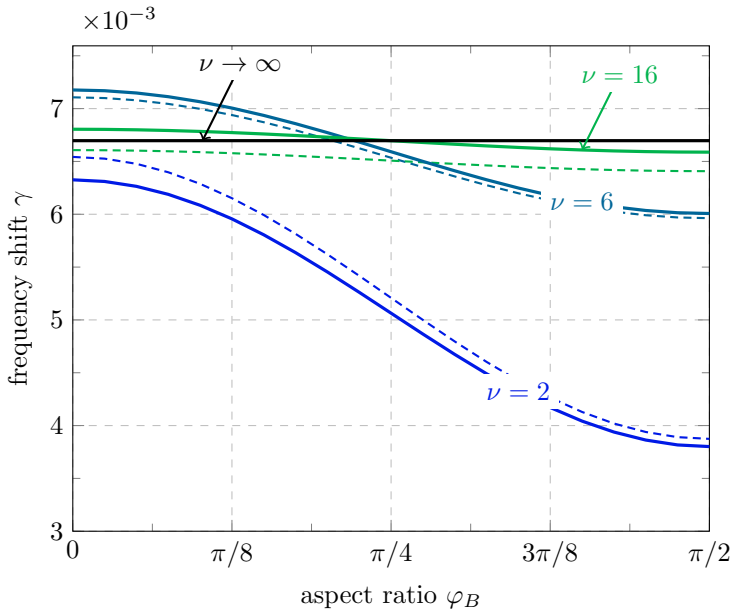

Figure 4.15: Frequency shift $\gamma^{(xy)}$ vs. orientation angle φ_B. The frequency shift is calculated using the column density model for $\varepsilon_D^{(m)} = 0.5$, for a non-dipolar BEC with $\varepsilon_D = 0$ (solid lines) and a dipolar BEC with $\varepsilon_D = \varepsilon_D^{(m)}$ (dashed lines). The results are shown for three different trap aspect ratios $\nu = \omega_x/\omega_z$. The black line shows approximation (4.54) for a non-dipolar BEC with $\varepsilon_D = 0$. The second orientation angle is set to $\vartheta_B = \pi/2$ and the distance to the surface is $x_d = 2\lambda_x^{(0)}$.

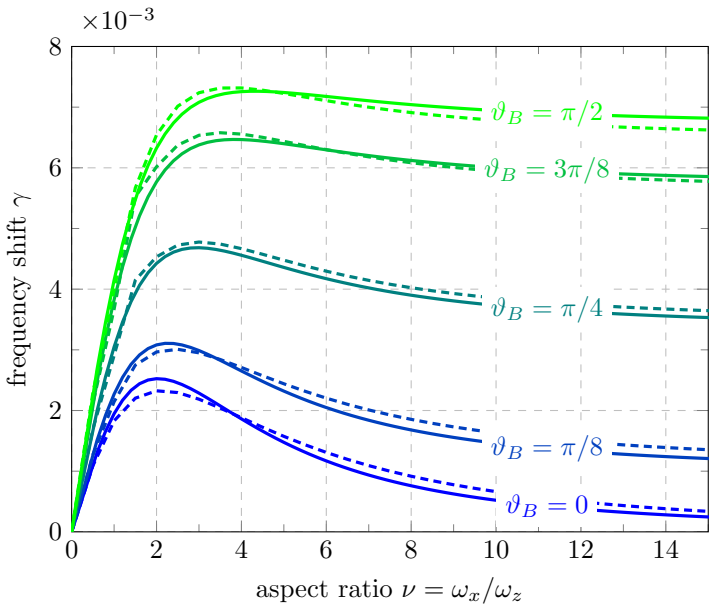

Figure 4.16: Frequency shift $\gamma^{(xz)}$ vs. trap aspect ratio $\nu = \omega_x/\omega_z$. The frequency shift is calculated using the column density model for $\varepsilon_D^{(m)} = 0.5$, for a non-dipolar BEC with $\varepsilon_D = 0$ (solid lines) and a dipolar BEC with $\varepsilon_D = \varepsilon_D^{(m)}$ (dashed lines). The BEC polarization changes from $\vartheta_B = 0$ (dipoles in z-direction) in steps of $\pi/8$ to $\vartheta_B = \pi/2$ (dipoles in x-direction). The second orientation angle is set to $\varphi_B = 0$ and the distance to the surface is $x_d = 2\lambda_x^{(0)}$.

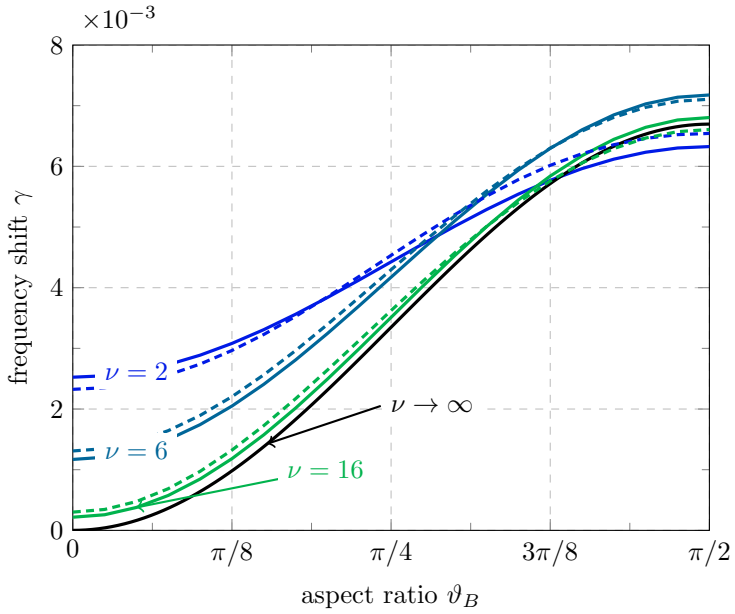

Figure 4.17: Frequency shift $\gamma^{(xz)}$ vs. orientation angle ϑ_B. The frequency shift is calculated using the column density model for $\varepsilon_D^{(m)} = 0.5$, for a non-dipolar BEC with $\varepsilon_D = 0$ (solid lines) and a dipolar BEC with $\varepsilon_D = \varepsilon_D^{(m)}$ (dashed lines). The results are shown for three different trap aspect ratios $\nu = \omega_x/\omega_z$. The black line shows approximation (4.51) for a non-dipolar BEC with $\varepsilon_D = 0$. The second orientation angle is set to $\varphi_B = \pi/2$ and the distance to the surface is $x_d = 2\lambda_x^{(0)}$.

In the limit of an infinitely elongated trap, the result reads

$$\gamma_\infty^{(xz)} = -\frac{3}{14}\varepsilon_D^{(m)}\left[\frac{\lambda_x^{(0)}}{x_d}\right]^4 \sin^2\vartheta_B. \tag{4.56}$$

In Fig. 4.16 the frequency shift is presented as function of ν and in Fig. 4.17 as function of ϑ_B.

The case $\varepsilon_D = \varepsilon_D^{(m)}$: The dipole-dipole interaction has an interesting effect in this configuration. As always, the dipole-dipole interaction modifies the semi axes and tilts the BEC. The BEC is tilted by an angle ϑ_{TF}, which is depicted in Fig. 4.18. The z-axis of the BEC is no longer parallel to the superconducting plane. One side of the BEC is shifted towards the surface, the other away from the surface. A constant distance x_d to the surface can no longer be assumed. The tip of the BEC has a distance $d = x_d - \lambda_z \sin\vartheta_{\mathrm{TF}}$

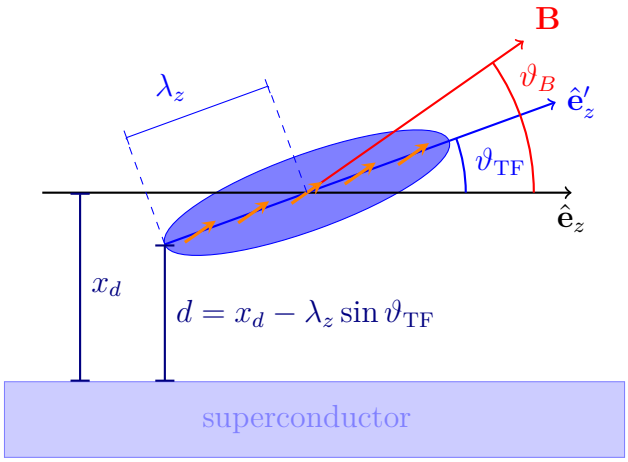

Figure 4.18: The dipoles in the BEC are oriented in the x-z-plane. This causes a tilt of the BEC within this plane. The distance between the BEC and the surface is no longer constant along the BEC axis. One tip of the BEC is tilted towards the surface, and the distance has reduced to $d = x_d - \lambda_z \sin\vartheta_{\mathrm{TF}}$.

to the surface. Obviously, if $d < x_d$, the BEC touches the surface. Fig. 4.19 shows d as a function of ϑ_B for different trap aspect ratios. Even for a large value of ε_D, the distance d is large enough so that the BEC does not touch the surface. Since the BEC is no longer parallel to the surface, expressions (4.24) and (4.42) for the frequency shift need to be modified. Say a dipole at position z in the BEC interacts with the mirror dipole at position z'. Due to the tilt of the BEC the x- and z-coordinates of both dipoles have changed. This means that also their distance has changed. In order to account for this, the function $H_k^{(x)}$ becomes

$$H_k^{(x)}\left(x_d, \lambda_z, \vartheta_{\mathrm{TF}}\right) = \int_{-\lambda_z}^{\lambda_z} \mathrm{d}z\, \Gamma_0\left(z\right) \Gamma_k\left(z\right) \left.\frac{\partial^2 \tilde{G}_k\left(x,z\right)}{\partial x^2}\right|_{x=2x_d+(2z-z')\sin\vartheta_{\mathrm{TF}}}$$

with

$$\tilde{G}_k\left(x,z\right) = \frac{1}{8\lambda_z} \int_{-\lambda_z+z}^{\lambda_z+z} \mathrm{d}z' \left(\frac{3x^2}{\left[x^2 + z'^2\cos^2\vartheta_{\mathrm{TF}}\right]^{5/2}} - \frac{1}{\left[x^2 + z'^2\cos^2\vartheta_{\mathrm{TF}}\right]^{3/2}} \right) z'^k.$$

In the same way the functions $H_k^{(z)}$ and D_k need to be modified. Using those functions, the frequency shift for the x-component $\gamma_{\vartheta_{\mathrm{TF}}}^{(x)}$ as well as

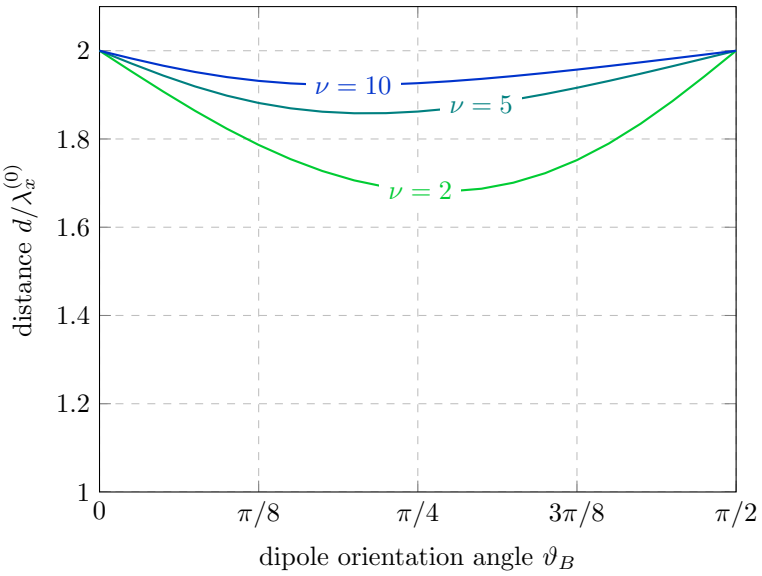

Figure 4.19: Distance d between the tip of the BEC and the surface vs. the orientation angle ϑ_B for three different aspect ratios ν. *Parameters:* $\kappa = 1$, $\varepsilon_D = 0.5$, $x_d = 2\lambda_x^{(0)}$, and $\varphi_B = 0$.

the frequency shift for the z-component $\gamma_{\vartheta_{\mathrm{TF}}}^{(z)}$ are calculated. Finally, the expression for the frequency shift reads

$$\gamma_{\vartheta_{\mathrm{TF}}}^{(xz)} = \gamma_{\vartheta_{\mathrm{TF}}}^{(x)} \sin^2\vartheta + \gamma_{\vartheta_{\mathrm{TF}}}^{(z)} \cos^2\vartheta.$$

The resulting frequency shift is plotted in Fig. 4.16 and Fig. 4.17 as dashed lines. Once again, the corrections to the case $\varepsilon_D = 0$ are not too drastic.

Chapter 5

Resonant excitation of BEC shape fluctuations

In this chapter shape fluctuations of the BEC are investigated. A particular kind of shape fluctuations is discussed, namely the monopole-quadrupole modes, which were introduced in Section 1.3. In a harmonic potential monopole-quadrupole modes and the center-of-mass motion are decoupled (see Section 1.3). In an anharmonic potential this is not the case. Anharmonic terms create a cross-mode coupling, thus the center of mass can not be excited without at the same time exciting shape fluctuation. This has been studied previously for anharmonic terms of the form x^3, x^4, etc. [107–109]. In Ref. [55] the potential generated by the superconducting surface was modeled using an effective potential of the form x^2z^2. With this term a coupling of the center-of-mass motion with the breather mode $\hat{\boldsymbol{\rho}}_s$ was observed. Here (and also presented in [56]) the full potential generated by the surface is used, which yields more features in the excitation spectrum than using the effective potential from Ref. [55].

Two different models are used to discuss the shape fluctuation: the GPE (3.28) and the hydrodynamic equations (1.36). Both models are solved numerically. In order to include the surface potential to the hydrodynamic equations, a simplification is necessary. This approximation is the reason that the results are not as precise as the results from the GPE. However, the model is still useful since it offers more insight into the mechanism of the mode excitation than the GPE does.

Throughout the whole chapter the dipoles are assumed to be oriented in the z-direction.

5.1 Numerical results for the shape fluctuations

Besides the information of the center-of-mass motion, the numerical results yield also information about the shape oscillations of the BEC. The observable that is used for this is

$$\sigma_a(t_j) = \sqrt{\left\langle (a - a_j)^2 \right\rangle},\ a \in \{x, y, z\}\,. \tag{5.1}$$

It represents a measure for the width of the BEC wave function. a_j is the center-of-mass coordinate at time t_j. For a TF ellipsoid the width σ_a is connected to the semi axes λ_a via

$$\sigma_a = \frac{\lambda_a}{\sqrt{7}},\ a \in \{x, y, z\}\,.$$

If monopole-quadrupole modes are excited, the width becomes time dependent. The frequencies that constitute the width oscillation are the monopole-quadrupole mode frequencies. A discrete Fourier transformation of the data set obtained by the numerical calculation yields the excitation spectrum. The peaks in the spectrum indicate which modes are excited and the peak height is a measure of the strength of the excitation.

5.1.1 Harmonic trap

To illustrate how monopole-quadrupole modes can get excited, a few examples are presented. For simplicity a non-dipolar BEC with $\varepsilon_D = 0$ in a harmonic trap is used. For BECs with $\varepsilon_D \neq 0$ the principle is the same, only the mode frequencies are different. In all examples the center of mass remains at rest at all times. The presented two examples are intended to illustrate how shape fluctuations can be excited. The peaks in the spectra of σ_a correspond to certain modes of the BEC. The simplest way to identify the correct mode, is to compare the frequency at which the peak appears in the spectrum to the mode frequencies determined by the linearized hydrodynamic equations presented in Section 1.2.3.

In a purely harmonic trap, a sudden change of the harmonic trap frequencies leads to the excitation of monopole-quadrupole modes. In Fig. 5.1 the time curves of σ_x, σ_y and σ_z are presented, along with the associated frequency spectra. For this example the GPE was solved for a non-dipolar BEC ($\varepsilon_D = 0$) in a spherical trap with $\omega_x = \omega_y = \omega_z = \omega$. For the time evolution the trap frequencies were reduced by a factor of 0.9, compared to

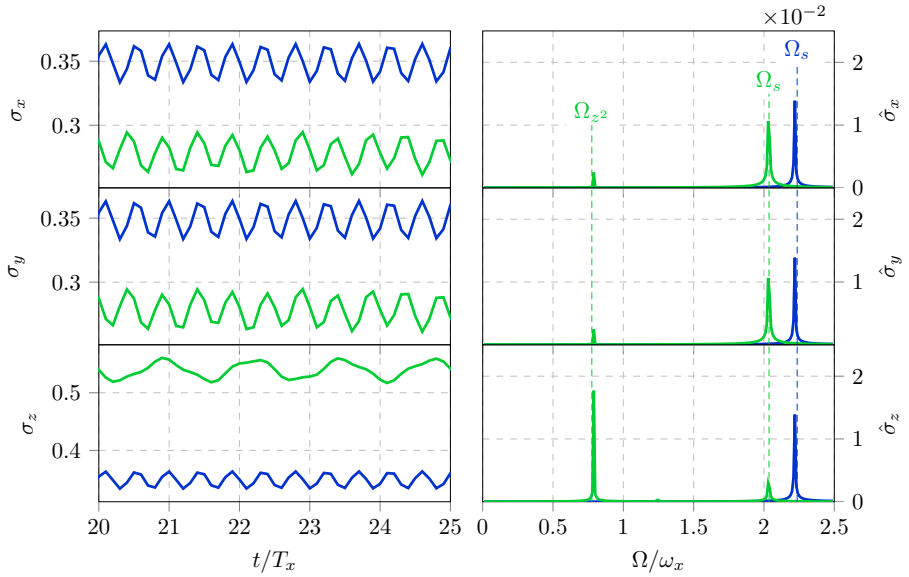

Figure 5.1: Left panel: width σ_a vs. time t. Right panel: Fourier transform $\hat{\sigma}$ vs. frequency Ω. The blue curves correspond to a non-dipolar BEC in a spherical trap with $\nu = 1$ and $\kappa = 1 \Rightarrow \omega_x = \omega_y = \omega_z = \omega$. The ground state was calculated in a trap with frequency $\bar{\omega} = 10/9\,\omega$. In the frequency spectrum a peak at about $\Omega \approx 2.23\,\omega$ appears. This corresponds to the breather mode frequency $\Omega_s = \sqrt{5}\,\omega$. The green curves correspond to a non-dipolar BEC in a uni-axial trap with $\nu = 2$ and $\kappa = 1$. The ground state was calculated in a trap with frequency $\bar{\omega}_x = 10/9\,\omega_x$, $\bar{\omega}_y = 10/9\,\omega_y$, and $\bar{\omega}_z = 10/9\,\omega_z$. Two peaks appear in the spectra. Since the trap is uni-axial, the spectra for σ_x and σ_y are identical. They show strong peaks at the position of the breather mode, with the TF frequency $\Omega_s \approx 2.036\,\omega_x$ and the d_{z^2}-mode with the TF frequency $\Omega_{z^2} \approx 0.776\,\omega_x$. The positions of the TF frequencies are indicated by vertical dashed lines. *Parameters:* length of the time evolution for the GPE: $t = 100\,T_x$, $\Delta t = 10^{-3}T_x$, with $T_x = 2\pi/\omega_x$, size of numerical lattice: $64 \times 64 \times 64$, expansion of the lattice: $6\lambda_x \times 6\lambda_y \times 6\lambda_z$, central density: $n_0^{(0)} = 2.5 \times 10^{13}\,\mathrm{cm}^{-3}$.

the trap frequencies used for the determination of the ground state. This corresponds to a sudden change of the trap frequencies at a time $t_0 = 0$. The time curves of σ_x, σ_y, and σ_z show harmonic oscillation and in the spectrum appears a strong peak at $\Omega \approx \sqrt{5}\omega$, where ω is the frequency during the time evolution. Only one peak appears in the spectrum. The reason is that in a spherical trap with an isotropic change of the trap frequencies an exact eigenmode (the breather mode) of the BEC is excited. In a uni-axial trap two modes are excited, which is also shown in Fig. 5.1. For an non-isotropic trap frequency change, more peaks would appear in the spectrum.

Another possibility to excite shape fluctuations is to use time dependent trap frequencies. For the presented examples, the trap frequency in x-direction is set to be of the form $\omega_x(t) = \omega_{x,0} + a_x \sin(\Omega_D t)$. The other two frequencies ω_y and ω_z remain constant. The trap is uni-axial with $\nu = 2$ and $\kappa = 1$. The drive frequency Ω_D is chosen such that it is close to one of the mode frequencies. The resulting spectra are presented in Fig. 5.2. One can see that three modes are excited. This means that not an exact eigenmode is excited but rather a combination of them. The mode which has the frequency closest to the driving frequency Ω_D is most strongly excited.

5.1.2 Shape fluctuations due to the eddy current effect

Close to the superconducting surface, the trapping potential is no longer purely harmonic. The potential generated by the mirror BEC superposes the external trapping potential. The mirror potential is only a small perturbation, thus the potential remains mainly harmonic. However, the anharmonic perturbation creates a coupling between the center-of-mass motion and the monopole-quadrupole modes.

In the following, uni-axial trap geometries with $\kappa = 1$ or almost uni-axial trap geometries with $\kappa \approx 1$ are considered. The reason why slightly asymmetric traps with $\kappa \approx 1$ are in some cases advantageous becomes apparent below. In an uni-axial (or almost uni-axial) trap the time dependence of σ_x is similar to the time dependence of σ_y. Therefore it is sufficient to analyze only one of the two. Instead of analyzing σ_x and σ_z separately, it is convenient to use the aspect ratio of the BEC

$$\zeta(t) = \frac{\sigma_z(t)}{\sigma_x(t)}.$$

This quantity contains the information necessary to study the excitation

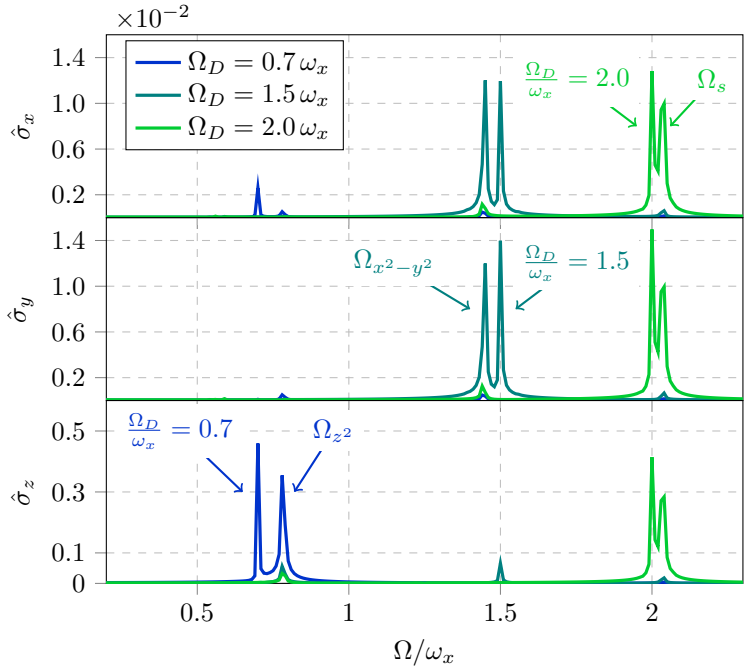

Figure 5.2: $\hat{\sigma}_a$ vs. frequency Ω. The curves correspond to a non-dipolar BEC in an uni-axial trap with $\nu = 2$ and $\kappa = 1$. The frequency in the x-direction has a time-dependent component $\omega_x(t) = \omega_{x,0} + a_x \sin(\Omega_D t)$. Three different driving frequencies Ω_D were used. Using the driving frequency $\Omega_D = 2\,\omega_x$, a strong excitation of the breather mode is observed in all three spectra. Whereas for $\Omega_D = 1.5\,\omega_x$, the $d_{x^2-y^2}$-mode is strongly excited, which results in strong peaks in the σ_x and σ_y spectra. In the σ_z spectrum only the peak of the driving frequency appears. For $\Omega_D = 0.7\,\omega_x$ a strong peak of the d_{z^2}-mode appears in the spectrum of σ_z. TF mode frequencies: $\Omega_s \approx 2.036\,\omega_x$, $\Omega_{x^2-y^2} \approx 1.414\,\omega_x$, and $\Omega_{z^2} \approx 0.776\,\omega_x$. *Parameters:* length of the time evolution for the GPE: $t = 100\,T_x$, $\Delta t = 10^{-3} T_x$, with $T_x = 2\pi/\omega_x$, size of numerical lattice: $64 \times 64 \times 64$, expansion of the lattice: $6\lambda_x \times 6\lambda_y \times 6\lambda_z$, central density: $n_0^{(0)} = 5 \times 10^{13}\,\mathrm{cm}^{-3}$.

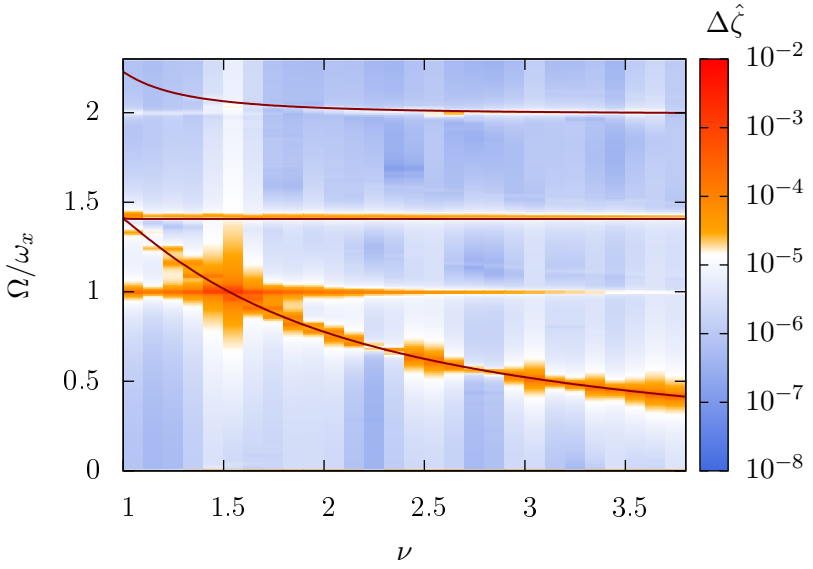

Figure 5.3: Excitation spectrum $\Delta\hat{\zeta}(\Omega)$ for various trap aspect ratios ν. The trap ratio ranges from $\nu = 1$ to $\nu = 4$ in steps of $\Delta\nu = 0.1$. The red lines show the monopole-quadrupole mode frequencies. *Parameters:* $\varepsilon_D = 0$, $\varepsilon_D^{(m)} = 0.15$, $\kappa = \omega_y/\omega_x = 0.99$, distance to surface $x_d = 2\lambda_x^{(0)}$, oscillation amplitude $x_s = 0.1\,\lambda_x^{(0)}$ length of the time evolution for the GPE: $t = 100\,T_x$, $\Delta t = 10^{-3}T_x$, with $T_x = 2\pi/\omega_x$, size of numerical lattice: $64 \times 64 \times 64$, expansion of the lattice: $6\lambda_x \times 6\lambda_y \times 6\lambda_z$, central density: $n_0^{(0)} = 5 \times 10^{13}\,\mathrm{cm}^{-3}$.

of the monopole-quadrupole modes. A discrete Fourier transformation of the data set $\zeta(t_j)$, yields the frequency data set $\hat{\zeta}(\Omega_k)$. The quantity $\hat{\zeta}(\Omega_k)$ represents the amplitude of the frequency component Ω_k.

As a first example, a non-dipolar BEC with $\varepsilon_D = 0$ and $\varepsilon_D^{(m)} = 0.15$ (^{52}Cr) is presented. The aspect ratio κ is fixed to $\kappa = 0.99$ and the aspect ratio ν is varied from $\nu = 1$ to $\nu = 4$.

In Fig. 5.3 the resulting frequency spectra of the relative fluctuations $\Delta\zeta = \frac{\zeta(0)-\zeta(t)}{\zeta(0)}$ are presented as a color map. The color map is plotted on a logarithmic scale in order to better highlight the regions of strong excitation. The blue regions correspond to no excitation and the red regions to strong excitation. For comparison, the monopole-quadrupole mode frequencies are plotted as dark-red lines. One can see that the regions close to the monopole quadrupole-modes show a strong excitation. Furthermore,

excitation appears at $\Omega \approx \omega_x$ and also a little at $\Omega \approx 2\omega_x$. Those peaks stem from the center-of-mass motion of the BEC. A very strong excitation is observed at the crossing point of the single center-of-mass frequency ω_x with the d_{z^2}-mode. A strong excitation is also observed in the region where the double center-of-mass frequency and the breather mode come close.

Those crossings correspond to resonant excitations of the monopole-quadrupole modes. This is due to the mode coupling generated by the anharmonic perturbation of the potential. If the center-of-mass frequency or a multiple integer of it coincide with one of the mode frequencies, a resonance significantly increases the mode excitation. The mechanism for this is discussed in the next section. Those two resonance peaks are in the following referred to as single and double center-of-mass peak, respectively.

It now becomes clear why the aspect ratio $\kappa = 0.99$ (Fig. 5.3) is preferable over the aspect ratio $\kappa = 1$. As is presented in Fig. 5.4, for $\kappa = 1$ the double center-of-mass frequency and the breather mode do not cross. Whereas for $\kappa = 0.9$ they do cross. For $\kappa < 1$, the breather mode frequency approaches a value below $2\omega_x$ as $\nu \to \infty$. For larger dipole-dipole interaction strengths, like for example $\varepsilon_D = 0.6$, the mode frequency forms a minimum below its limit value and then approaches the value from below rather than from above. In this case there is a crossing point even for $\kappa = 1$. The position of the crossing point is very sensitive to the aspect ratio κ and also the dipole-dipole interaction strength. For $\kappa = 0.9$ the position of the crossing point with the double oscillation frequency does not vary so much for different ε_D as it does for $\kappa = 1$. The single oscillation frequency has a crossing point with the d_{z^2}-mode. Here the crossing point is not very sensitive to neither ε_D nor κ, as is presented in Fig. 5.4.

The strength of the resonance peak depends mainly on two parameters: the dipole-dipole interaction parameter $\varepsilon_D^{(m)}$ and the oscillation amplitude x_s. Since the mirror potential is linear in $\varepsilon_D^{(m)}$, it is natural to assume that the peak height also scales linearly with $\varepsilon_D^{(m)}$. That this is actually the case is shown in Fig. 5.5. Two spectra are presented, one for $\varepsilon_D^{(m)} = 0.15$ and one for $\varepsilon_D^{(m)} = 0.3$. In both calculations the dipole-dipole interaction parameter in the GPE was set to $\varepsilon_D = 0$. This is done in order to avoid the influence of ε_D on the excitation amplitude. The closer the calculation is performed to the actual crossing point, the larger the amplitude of the excitation gets. Changing the value of ε_D would shift the position of the crossing point relative to position where the numerical calculation is preformed, thus the amplitude of the excitation would be different. Of course, $\varepsilon_D^{(m)}$ has an influence on the center-of-mass frequency, as was discussed in the previous chapter. However, the shift of the crossing point due to that is

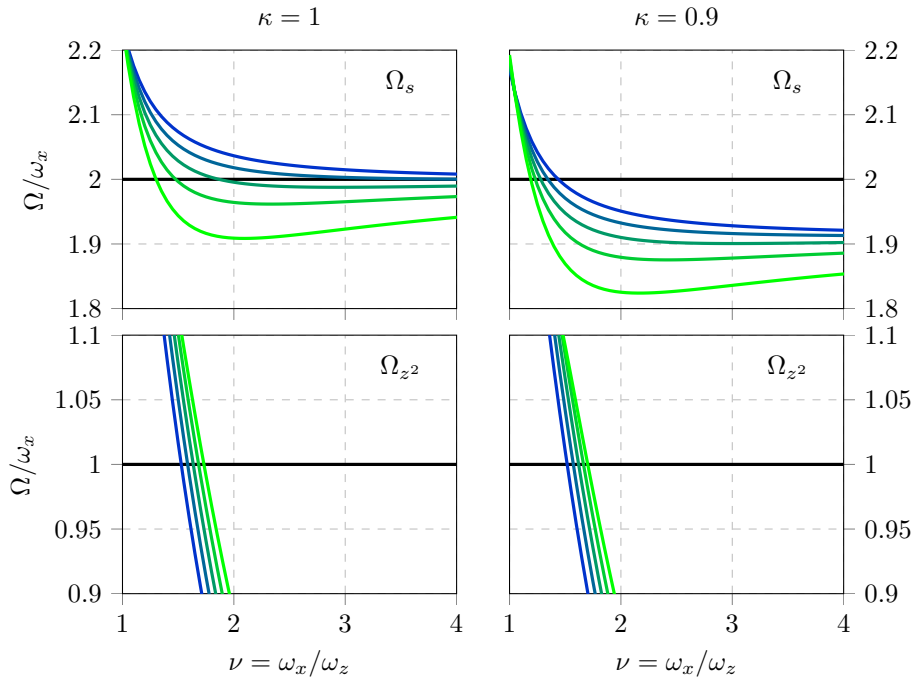

Figure 5.4: Monopole-quadrupole mode frequencies vs. trap aspect ratio $\nu = \omega_x/\omega_z$. The mode frequencies were calculated with the linearized hydrodynamic equations (1.37). The upper two plots show the breather mode frequency Ω_s the bottom plots show the d_{z^2}-mode frequency Ω_{z^2}. The left two plots are for $\kappa = 1$ and the right two for $\kappa = 0.9$. The different lines correspond to different values of ε_D, ranging from $\varepsilon_D = 0$ (blue) to $\varepsilon_D = 0.8$ (green) in steps of $\Delta\varepsilon_D = 0.2$.

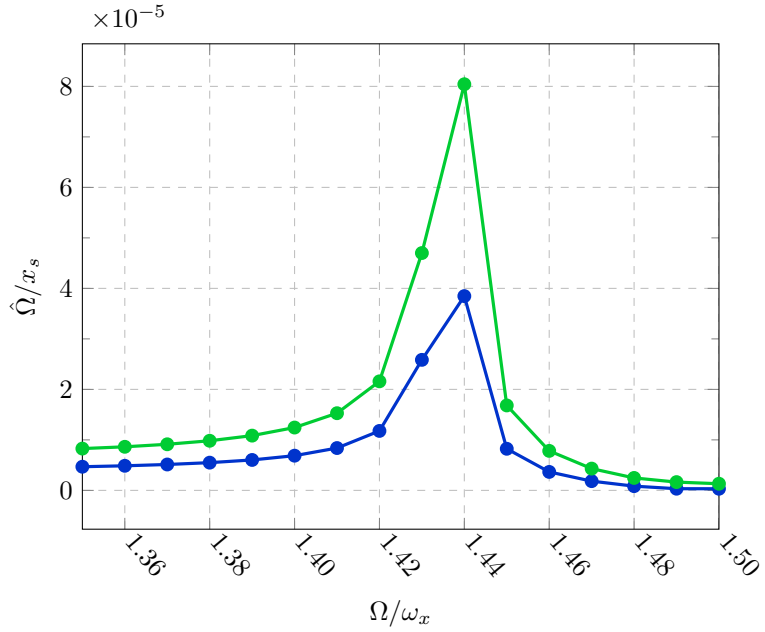

Figure 5.5: Frequency spectra for two different values of $\varepsilon_D^{(m)}$. Both curves correspond to a non-dipolar BEC with $\varepsilon_D = 0$. Presented is the $d_{x^2-y^2}$-mode peak for a trap with ratios $\nu = 3$ and $\kappa = 0.99$. The blue line shows the spectrum for $\varepsilon_D^{(m)} = 0.15$ and the green line for $\varepsilon_D^{(m)} = 0.3$. *Parameters*: length of time evolution for $t = 500\,T_x$, with $T_x = 2\pi/\omega_x$, size of numerical lattice: $64 \times 64 \times 64$, expansion of the lattice: $6\lambda_x \times 6\lambda_y \times 6\lambda_z$, central density: $n_0^{(0)} = 5 \times 10^{13}\,\mathrm{cm}^{-3}$.

so small that it does not play an important role here. In order to avoid the effect of a possible shift of the resonance position completely, the mode present in Fig. 5.5 is the $d_{x^2-y^2}$-mode, where no crossing resonance occurs.

In order to investigate the above mentioned resonance peaks more closely, the spectra in Fig. 5.6 are presented. They correspond to a dipolar BEC with $\varepsilon_D = \varepsilon_D^{(m)} = 0.2$. Only the sections of the spectrum are shown where the cross-mode resonances occur. Again, the color map is plotted on a logarithmic scale. Additionally, the individual spectra for each ν are shown on a linear scale as black lines.

To study the scaling of the resonance peaks with the oscillation amplitude, the spectra are shown for two different oscillation amplitudes: $x_s = 0.01\lambda_x^{(0)}$ and $x_s = 0.1\lambda_x^{(0)}$. The single and the double center-of-mass peaks exhibit clearly different scaling behaviors. The increase of the oscillation amplitude by one order of magnitude also increases the height of the single center-of-mass peak by one order of magnitude. Whereas the height of the double center-of-mass peak increases by two orders of magnitude. This infers that the single center-of-mass peak scales linearly with the oscillation amplitude and the double center-of-mass peak scales quadratically with the oscillation amplitude. The reason for this scaling behavior is discussed is the next section.

For an experiment the dependence of the peak height on the oscillation amplitude is more interesting than the dependence on $\varepsilon_D^{(m)}$. The value of $\varepsilon_D^{(m)}$ is fixed by the kind of atoms used in the experiment (excluding the possibility of tuning a_s with Feshbach resonances, see for example [59]). Whereas the oscillation amplitude can be easily manipulated.

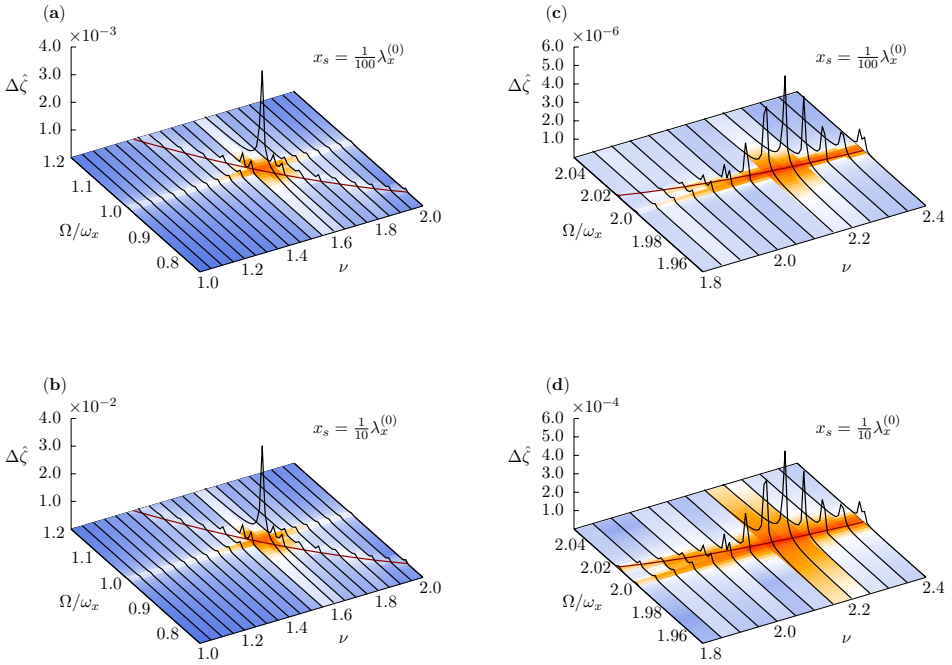

Figure 5.6: Frequency spectrum of $\Delta\hat{\zeta}(\omega)$ vs. trap ratio ν for two different oscillation amplitudes x_s. The trap ratio ranges from $\nu = 1$ to $\nu = 2.4$ in steps of $\Delta\nu = 0.05$. **(a)** and **(b)** show the section of the spectrum around ω_x', **(c)** and **(d)** show the section around $2\omega_x'$. The dark-red lines indicate the mode frequencies Ω_s and Ω_{z^2}. From **(a)** and **(c)** to **(b)** and **(d)**, the oscillation amplitude increases from $x_s = 0.01\lambda_x^{(0)}$ to $x_s = 0.1\lambda_x^{(0)}$. *Parameters*: $\varepsilon_D = \varepsilon_D^{(m)} = 0.2$; $\kappa = \omega_y/\omega_x = 0.99$; length of time evolution for **(a)** and **(b)** $t = 100\,T_x$ and for **(c)** and **(d)** $t = 500\,T_x$, with $T_x = 2\pi/\omega_x$, size of numerical lattice: $64\times64\times64$, expansion of the lattice: $6\lambda_x\times6\lambda_y\times6\lambda_z$, central density: $n_0^{(0)} = 5\times10^{13}\,\mathrm{cm}^{-3}$.

5.2 Shape fluctuations based on the hydrodynamic equations

In this section a simplified model of the BEC as well as the mirror potential is presented. The goal is to get a better understanding of the results obtained by numerically solving the GPE. In Chapter 1 the hydrodynamic equations were presented as way to calculate the time evolution of a BEC within the Thomas-Fermi regime by dropping the quantum pressure term. In the previous chapter the parameters of the simulations were chosen such that the BEC was well within the Thomas-Fermi regime. Therefore, the results from the hydrodynamic equations should not be significantly different from the GPE results. For the case that the BEC is trapped in a harmonic potential, the coupled equations of motion for the three semi axes of the TF ellipsoid have already been presented in Section 1.2.3 and are given in Eq. (1.36). In Ref. [107] Ott et al. discuss a method how the oscillation of a BEC in an anharmonic potential can be viewed within the center-of-mass frame as a stationary BEC in a harmonic potential with time dependent trap frequencies. They accomplish this by a local harmonic approximation of the potential. In the following the same kind of idea is used.

As demonstrated before, the column density model represents a tool which allows to find analytic expressions for the mirror potential. The column density potential is expanded in a Taylor series about the minimum of the harmonic trap. This gives the explicit anharmonic terms of the potential. Next, the anharmonic potential is transformed into the center-of-mass frame, which is co-moving with the BEC. The BEC oscillates with an amplitude x_s and frequency ω_x' around the potential minimum. The transformation between the stationary and the co-moving frame of reference is given by $x = x' + x_s \sin(\omega_x' t)$. Since the BEC only moves in the x-direction the other two coordinates transform as $y = y'$ and $z = z'$. Exemplary, the transformation of one term of the expansion is presented here in order to demonstrate the main idea. The remaining terms are discussed in Appendix D. The anharmonic term of the form xz^2 transforms as follows:

$$xz^2 = x'z'^2 + z'^2 x_s \sin(\omega_x' t) .$$

The goal is to collect all terms that are harmonic within the center-of-mass frame. In the above example it is the term $z'^2 x_s \sin(\omega_x' t)$. The anharmonic term $x'z'^2$ is dropped. Simply dropping this anharmonic term is not an approximation in a strict sense, since there is no reason to assume that it is small compared to the other term. Using this approach, some quantitative differences to the results of the numerical calculations using the full poten-

tial are to be expected. Nevertheless, the assumption is that this model is still capable of reproducing the qualitative behavior. The term proportional to z'^2 modifies the trap frequency in the z-direction. In the above example this term has a time dependent factor $x_s \sin(\omega'_x t)$. This means that it will generate a time dependent variation of the trap frequency. The evaluation of the full expression generated by the Taylor series expansion yields the time dependent harmonic potential

$$V(\mathbf{r}', t) = \frac{m}{2}\left\{\Omega_x^2(t)\, x'^2 + \Omega_y^2(t)\, y'^2 + \Omega_z^2(t)\, z'^2\right\},$$

where the trap frequencies are given by

$$\Omega_a^2(t) = \omega_a^2 + \frac{\varepsilon_D^{(m)}}{m} V_{x,aa} x_s \sin(\omega'_x t) + \frac{\varepsilon_D^{(m)}}{2m} V_{xx,aa} x_s^2 \sin^2(\omega'_x t), \tag{5.2}$$

with $a \in \{x, y, z\}$. The derivation of this expression and the definitions of the coefficients $V_{x,aa}$ and $V_{xx,aa}$ are presented in Appendix D. Previously, it was shown that time dependent trap frequencies lead to the excitation of collective modes. The above given expression has two terms that are time dependent. The first term is proportional to $\sin(\omega'_x t)$, which generates a modulation of the trap with the single oscillation frequency, the other term is proportional to $\sin^2(\omega'_x t)$ and therefore leads to a modulation with the double oscillation frequency.

The excitation mechanism in the anharmonic potential can be interpreted in such a way that the relative motion between the BEC and its mirror is driving time dependent changes of the trap frequencies. The terms with $\sin(\omega'_x t)$ drive the system with the single center-of-mass oscillation frequency ω'_x and the terms proportional to $\sin^2(\omega'_x t)$ drive the system with the double oscillation frequency $2\omega'_x$. If the eigenfrequencies of the BEC come close to the driving frequencies, a resonance occurs. The excitation spectra obtained by this method are presented in Fig. 5.7. All expected resonance peaks are visible in the spectrum. Since the chosen values of ν did not quite hit the crossing point of the single center-of-mass frequency with the d_{z^2}-mode, an additional spectrum for $\nu = 1.575$ was inserted. The strength of the peaks show the same scaling with the oscillation amplitude x_s, as was observed in the results from the time dependent GPE. The reason for this behavior can now be understood in terms of the time dependent oscillation frequencies (5.2). The terms that generate the driving force with the double oscillation frequency are quadratic in x_s and the terms generating the single oscillation frequency driving force are linear in x_s. The linear scaling of the peak height with $\varepsilon_D^{(m)}$ (see Fig. 5.5) is also consistent with this model, since the time dependent terms in (5.2) are all linear in $\varepsilon_D^{(m)}$.

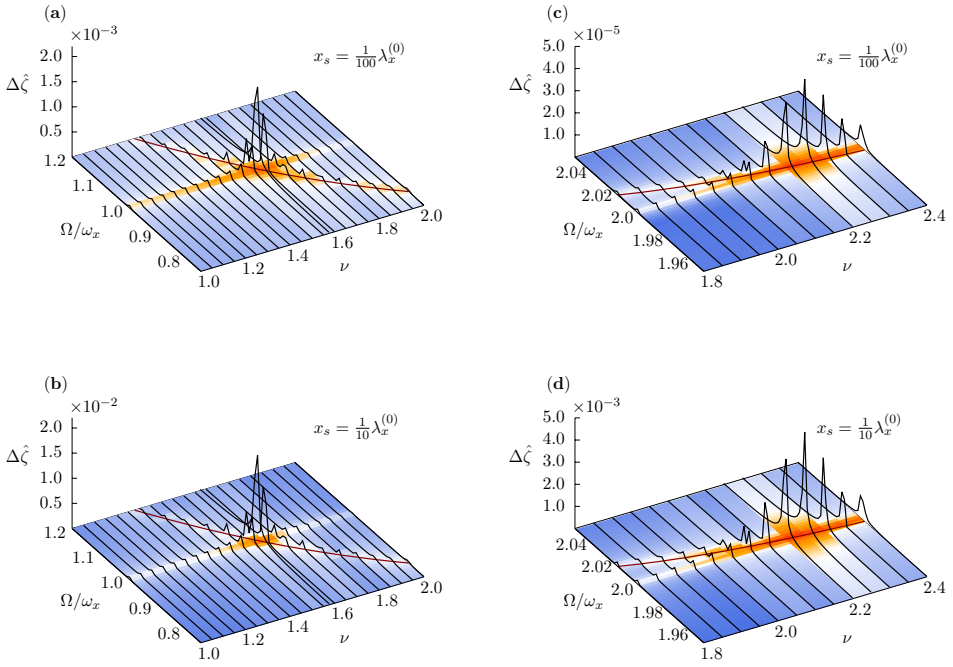

Figure 5.7: Frequency spectrum of $\Delta\hat{\zeta}(\omega)$ vs. trap ratio ν based on the solution of the hydrodynamic equations of motion for the semi axes (1.36) with time dependent trap frequencies (5.2). The parameters are the same as in Fig. 5.6.

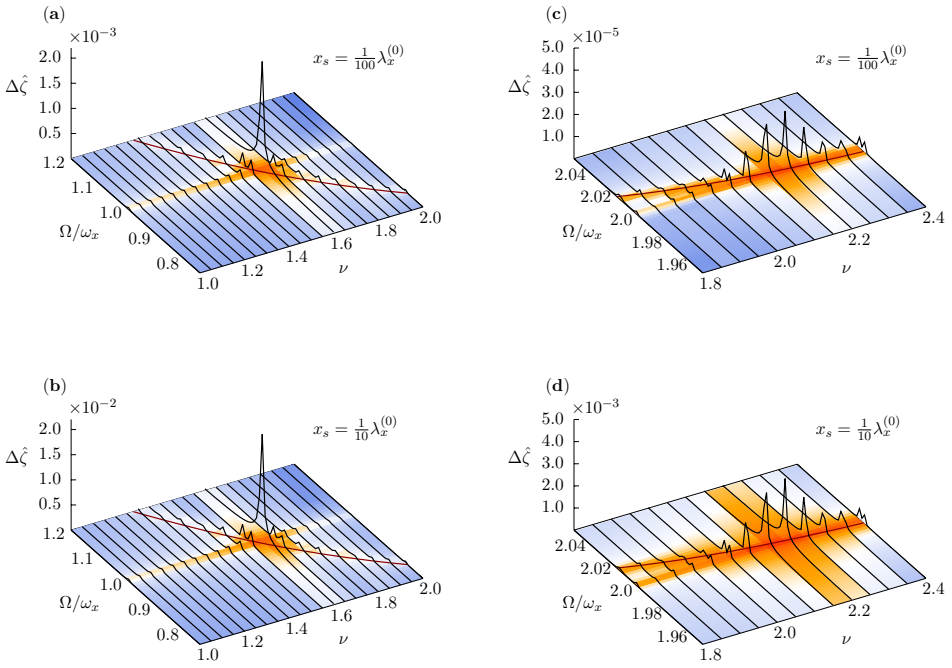

Figure 5.8: Frequency spectrum of $\Delta\hat{\zeta}(\omega)$ vs. trap ratio ν based on the solution of the GPE with time dependent trap frequencies (5.2). The parameters are the same as in Fig. 5.6.

This model shows a qualitative agreement with the numerical results from the previous section. However, the absolute height of the peaks is not the same. The reason for this is probably the way the mirror potential was approximated. In order to reduce the result from the Taylor series to this time dependent harmonic potential, the terms which did not fit into the desired scheme had to be dropped (see Appendix D). But dropping these terms is not a controlled approximation, since they are not necessarily small compared to the terms that we keep. This is probably the main reason for the observed deviations. Another reason might be that for large amplitudes the series expansion about the harmonic trap minimum becomes inaccurate. Furthermore, the one dimensional column density was used to calculate the mirror potential. But, as can be seen from the results for the frequency shift, the column density model yields quite accurate results. Thus, the observed deviation in the spectra should not stem from that. Neglecting the quantum pressure term in the equations of motion for the semi axes might also play a role. That this is not the case is presented in Fig. 5.8. It shows the

excitation spectra obtained by solving the GPE in a harmonic trap with the time dependent trap frequencies 5.2. No center-of-mass oscillation was excited for these calculations. The results show a fair agreement with the results from the hydrodynamic equations.

Summary & Conclusion

The subject of this thesis was the study of the magnetic interaction between a dipolar BEC and a superconductor. In order to study the interaction, the GPE for a dipolar BEC close to a superconducting surface was derived and then solved numerically. The computation time necessary to solve the GPE was reduced by using CUDA to parallelize the computations and perform them partially on the GPU. These numerically obtained results were compared to results based on analytical and semi-analytical approximations.

It was shown that the interaction is strong enough, in order to generate a frequency shift that can be measured in an experiment. Furthermore, different fingerprints of the effect were presented. In particular the frequency shift as a function of the number of atoms in the BEC presents a unique signature of the effect. Also the dependence of the frequency shift on the orientation of the magnetic dipoles can be used as an identifying criterion.

Different magnetic dipole orientations can also be used to enhance the effect. It was shown that the orientation of the dipoles perpendicular to the surface results in the strongest effect. In case that the dipoles are oriented parallel to the surface, an orientation perpendicular to the long axis of the BEC yields a roughly two times larger frequency shift than an orientation parallel to the long axis.

Besides the center-of-mass motion of the BEC, the interaction with the surface has also an effect on the internal dynamics of the BEC. It was shown hat the anharmonic terms, introduced by the surface potential, cause excitations of collective shape oscillations. The coupling between the center-of-mass motion and the collective modes can be used to resonantly enhance this effect. Adjusting the mode frequencies to match the single or double center-of-mass oscillation frequency, generates resonance peaks in the excitation spectrum. The scaling of those resonance peaks with the center-of-mass oscillation amplitude can also be used as a signature for this particular type of anharmonic potential.

In an experiment, the superconductor is of course not a half-space, but

typically a rectangular superconducting strip. The size of this strip needs to be large enough, in order for the half-space approximation to be applicable. For practical purposes this means that the length and width of the strip need to be at least of the size of the BEC expansion. They also need to be larger than the distance between BEC and surface. If this is not the case, the interaction gets modified, which changes the resulting frequency shift. Since the magnetic field penetrates the surface of the superconductor, the thickness of the strip should be at least twice the penetration depth. The London penetration depth for elementary superconductors ranges typically from a few 10 nm to about 100 nm. This means a thickness of $\sim 200\,\mathrm{nm}$ is sufficient to meet that requirement. The assumed distance of $14\,\mu\mathrm{m}$ between harmonic trap minimum and surface is based on experimental results and is therefore a realistic value. The polarization of the BEC requires the application of an external magnetic field in the wanted direction. Polarization parallel to the surface does not pose a problem. However, polarizing the BEC perpendicular to the superconducting surface might be difficult to achieve. The reason is that the normal component of the polarizing **B**-field must vanish at the surface of the superconductor. This distorts the magnetic field close to the surface and can thereby modify the polarization of the BEC.

So far, experiments with superconducting microtraps have only been implemented with ^{87}Rb BECs. However, due to their very small dipole moments, ^{87}Rb BECs are rather unsuited for the type of experiment described in this thesis. The results presented here show that it is worthwhile to pursue the combination of dipolar BECs with superconducting components. In fact, any type of experiment, based on the magnetic interaction between a BEC and a superconductor, benefits form a larger magnetic dipole moment.

The investigations presented in this thesis can be regarded as a precursor for further studies of this type of setup. Another interesting setup consists of a superconducting loop and a BEC. The magnetic flux through a superconducting loop is quantized in so-called flux quanta $\phi_0 = h/(2e)$. The field generated by the loop influences the statical and dynamical properties of the BEC, like for example the transition temperature or the oscillation frequency. Since the loop is not just a passive component, as was the case for the superconducting surface discussed in this work, the effect on the BEC is a lot larger. The situation becomes even more interesting, especially in regard to quantum computing, if the loop is replaced by a superconducting quantum interference device (SQUID). The SQUID can be put in a superposition of two different flux states and it would be interesting to study the effects on a BEC, trapped nearby such a SQUID.

Appendix A

Dipolar BEC

Here a summary of the central results of Ref. [57], that are relevant for the present work, is given. In the first section the self-consistency equations are given for the TF ellipsoid for the case that the dipoles are not aligned with one of the harmonic trap axes. In the second section the monopole-quadrupole modes are discussed. In particular the parametrization of the shape fluctuation is presented and the set of coupled equations determining the eigenmodes and eigenfrequencies. For a derivation of these results and a detailed discussion see Ref. [57].

A.1 TF self-consistency equations for a BEC

Consider a fully spin-polarized BEC. The dipoles are oriented in a plane spanned by two of the three axes defined by the harmonic trap. Without loss of generality the two axes are set to be $\hat{\mathbf{e}}_x$ and $\hat{\mathbf{e}}_z$. The TF ellipsoid is oriented in a direction which neither coincides with the direction of the dipoles nor with the direction of the trap. The TF ellipsoid is defined by the following set of coupled self-consistency equations:

$$1-\varepsilon_D+\frac{3}{2}\varepsilon_D\lambda_x\lambda_y\lambda_z\left[\sin^2(\vartheta_0)\,I_x+\cos^2(\vartheta_0)\,I_z\right]=\frac{\mu}{n_0 g_s}, \tag{A.1}$$

$$\frac{\frac{1-\varepsilon_D}{\lambda_x^2}+\frac{3\varepsilon_D}{2}\lambda_x\lambda_y\lambda_z\left[\cos^2(\vartheta_0)\,I_{xz}+3\sin^2(\vartheta_0)\,I_{xx}\right]}{\omega_x^2\cos^2(\vartheta_T-\vartheta_0)+\omega_z^2\sin^2(\vartheta_T-\vartheta_0)}=\frac{m}{2g_s n_0}, \tag{A.2}$$

$$\frac{\frac{1-\varepsilon_D}{\lambda_y^2}+\frac{3\varepsilon_D}{2}\lambda_x\lambda_y\lambda_z\left[\cos^2(\vartheta_0)\,I_{yz}+\sin^2(\vartheta_0)\,I_{xy}\right]}{\omega_y^2}=\frac{m}{2g_s n_0}, \tag{A.3}$$

$$\frac{\frac{1-\varepsilon_D}{\lambda_z^2}+\frac{3\varepsilon_D}{2}\lambda_x\lambda_y\lambda_z\left[3\cos^2(\vartheta_0)\,I_{zz}+\sin^2(\vartheta_0)\,I_{xz}\right]}{\omega_x^2\sin^2(\vartheta_T-\vartheta_0)+\omega_z^2\cos^2(\vartheta_T-\vartheta_0)}=\frac{m}{2g_s n_0}, \tag{A.4}$$

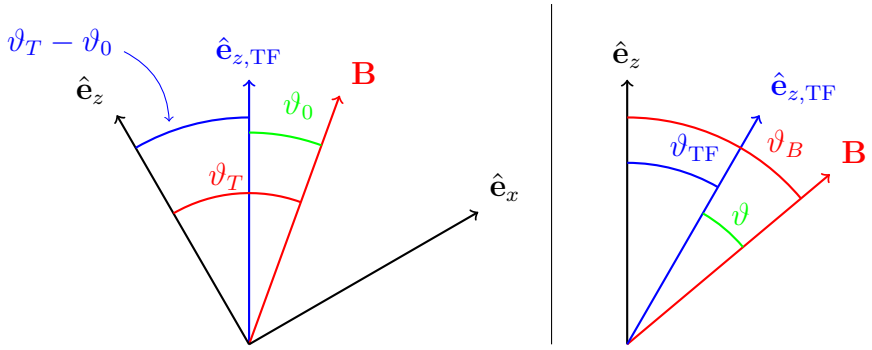

Figure A.1: Left panel: The trap (black axes) is rotated away form the **B**-field (red) by an angle ϑ_T. The z-axis of the resulting TF ellipsoid is oriented in the direction of $\hat{\mathbf{e}}_{z,\mathrm{TF}}$ (blue). Right panel: Same setup as in the left panel, only the angles defined in Section 4.3.3 are used.

$$\frac{3\varepsilon_D}{2}\lambda_x\lambda_y\lambda_z \sin(2\vartheta_0)\, I_{xz} = \frac{m}{2g_s n_0}\frac{\omega_x^2-\omega_z^2}{2}\sin(2\vartheta_T - 2\vartheta_0)\,. \tag{A.5}$$

There are six unknown quantities λ_x, λ_y, λ_z, n_0, μ and ϑ_0 and equations (A.1)-(A.5) give a set of five equations in order to determine the unknowns. The sixth equation is again given by the normalization condition $n_0 = \frac{15}{8\pi}\frac{N}{\lambda_x\lambda_y\lambda_z}$. The index integrals used in the above given equations are defined in (1.28) and (1.29). The angle ϑ_T is the angle between z-direction of the harmonic trap and the orientation of the dipoles. The angle ϑ_0 is the angle between the z-axis of the TF ellipsoid and the dipole orientation. In Fig. A.1 the relative orientation of the three involved axes is depicted. It suffices to consider the range $0 \leq \vartheta_T \leq \pi/2$. For the case that $\vartheta_T = 0$ or $\vartheta_T = \pi/2$ two angles are equal: $\vartheta_T = \vartheta_0$. The equations reduce to the case presented in Section 4.3.3. The connection to the angles used in Section 4.3.3 is illustrated in Fig. A.1, it is given by:

$$\vartheta_{\mathrm{TF}} = \vartheta_T - \vartheta_0$$

and

$$\vartheta_B = \vartheta_T.$$

In order to calculate dipole orientations in a different plane than the one spanned by $\hat{\mathbf{e}}_x$ and $\hat{\mathbf{e}}_z$, one simply needs to swap the according directions. For example in order to calculate the polarization in the y-z-plane, the x- and y-direction in the self-consistency equations need to be swapped.

A.2 Monopole-quadrupole modes

In Ref. [57] the time dependent density distribution of the BEC is written as

$$n(\mathbf{r},t) = n_{\mathrm{TF}}(\mathbf{r}) + \delta n(\mathbf{r},t), \tag{A.6}$$

where $n_{\mathrm{TF}}(\mathbf{r})$ is the TF ground state of the BEC. The fluctuation $\delta n(\mathbf{r},t)$ around the equilibrium must be such that particle conservation is guaranteed at all times. Furthermore, only density fluctuations are considered where the BEC remains an ellipsoid. The parametrization of the ellipsoidal density fluctuation is achieved by

$$\delta n(\mathbf{r},t) = n_{\mathrm{TF}}(\mathbf{r} + \boldsymbol{\eta}(\mathbf{r},t), \boldsymbol{\lambda} + \boldsymbol{\zeta}(t)) - n_{\mathrm{TF}}(\mathbf{r},\boldsymbol{\lambda}), \tag{A.7}$$

where $\boldsymbol{\zeta}(t)$ describes the time depended dilatation of the semi axes and $\boldsymbol{\eta}(\mathbf{r},t)$ is a displacement vector field. In order for the BEC to remain an ellipsoid the displacement vector field must be of the form

$$\eta_a(\mathbf{r},t) = \eta_a^{(0)}(t) + \sum_{b\in\{x,y,z\}} \eta_{ab}^{(1)}(t)\, a, \quad a \in \{x,y,z\}. \tag{A.8}$$

The 0th order term $\eta_a^{(0)}(t)$ describes the center-of-mass motion of the BEC. In a harmonic trap the center-of-mass motion is decoupled from the other modes and $\eta_a^{(0)}(t)$ can therefore be disregarded here. It turns out that particle conservation requires that $\boldsymbol{\nabla}\cdot\boldsymbol{\eta} = 0$. In Ref. [57] the parametrization of the density fluctuation is given by

$$\begin{aligned}\delta n(\mathbf{r},t) &= 2n_0\Bigg[\frac{1}{\lambda_x^2}\rho_{xx}(t)\,x^2 + \frac{1}{\lambda_y^2}\rho_{yy}(t)\,y^2 + \frac{1}{\lambda_z^2}\rho_{zz}(t)\,z^2 \\ &\quad -\frac{1}{2}\left(1 - \frac{x^2}{\lambda_x^2} - \frac{y^2}{\lambda_y^2} - \frac{z^2}{\lambda_z^2}\right)\rho_{00}(t) \\ &\quad + \sum_{a<b}\frac{1}{\lambda_a\lambda_b}\rho_{ab}(t)\,a\cdot b\Bigg],\end{aligned} \tag{A.9}$$

with $a,b \in \{x,y,z\}$. The coefficients ρ_{ab} are connected to the displacement vector field $\boldsymbol{\eta}(\mathbf{r},t)$ and the dilatation $\boldsymbol{\zeta}(t)$ of the semi-axes via

$$\begin{aligned}\rho_{ab}(t) &= \delta_{ab}\left[\frac{\zeta_a(t)}{\lambda_a} - \eta_{aa}^{(1)}(t)\right] \\ &\quad -(1-\delta_{ab})\,\lambda_a\lambda_b\left[\frac{1}{\lambda_a^2}\eta_{ab}^{(1)}(t) + \frac{1}{\lambda_b^2}\eta_{ba}^{(1)}(t)\right],\end{aligned} \tag{A.10}$$

where δ_{ab} is the Kronecker delta and

$$\rho_{00}(t) = \sum_a \rho_{aa}(t).$$

The linearized hydrodynamic equation yield a set of six coupled differential equations for $\rho_{ab}(t)$. Using the ansatz

$$\rho_{ab}(t) = \widehat{\rho}_{ab}(\Omega)\cos(\Omega t), \tag{A.11}$$

yields to the following set of equations

$$\frac{2n_0 g_s}{m}\begin{pmatrix} C_{xx,xx} & C_{xx,yy} & C_{xx,zz} & 0 & 0 & 0 \\ C_{yy,xx} & C_{yy,yy} & C_{yy,zz} & 0 & 0 & 0 \\ C_{zz,xx} & C_{zz,yy} & C_{zz,zz} & 0 & 0 & 0 \\ 0 & 0 & 0 & C_{xz,xz} & 0 & 0 \\ 0 & 0 & 0 & 0 & C_{yz,yz} & 0 \\ 0 & 0 & 0 & 0 & 0 & C_{xy,xy} \end{pmatrix}\begin{pmatrix} \widehat{\rho}_{xx} \\ \widehat{\rho}_{yy} \\ \widehat{\rho}_{zz} \\ \widehat{\rho}_{xz} \\ \widehat{\rho}_{yz} \\ \widehat{\rho}_{xy} \end{pmatrix} = \Omega^2 \begin{pmatrix} \widehat{\rho}_{xx} \\ \widehat{\rho}_{yy} \\ \widehat{\rho}_{zz} \\ \widehat{\rho}_{xz} \\ \widehat{\rho}_{yz} \\ \widehat{\rho}_{xy} \end{pmatrix}.$$

The eigenvectors of this set of equations describe the shape fluctuation of the BEC to the corresponding eigenmodes via Eq. (A.11) and Eq. (A.9). The upper 3×3 block corresponds to the monopole-quadrupole modes discussed in Section 1.2.3. The lower 3×3 block corresponds to the scissor modes, which in the symmetric case are decoupled from the other monopole-quadrupole modes and also from each other. In the case that the dipole orientation and the harmonic trap are not aligned, these modes are not decoupled (see Ref. [57]). Ω is the eigenfrequency of the respective mode and $\widehat{\rho}_{ab}(\Omega)$ is the component of the eigenvector. The coefficients $C_{ab,cd}$ are defined by:

$$\begin{aligned}
\frac{2n_0 g_s}{m} C_{xx,xx} &= \omega_y^2 \frac{\lambda_y^2}{\lambda_x^2} \frac{3(1-\varepsilon_D) + \frac{9}{2}\varepsilon_D \frac{\lambda_x^4}{\lambda_z^4} \overline{I}_{xxz}}{1 - \varepsilon_D + \frac{3\varepsilon_D}{2} \frac{\lambda_y^2}{\lambda_z^2} \overline{I}_{zy}}, \\
\frac{2n_0 g_s}{m} C_{xx,yy} &= \omega_y^2 \frac{\lambda_y^2}{\lambda_x^2} \frac{(1-\varepsilon_D) + \frac{3}{2}\varepsilon_D \frac{\lambda_x^2}{\lambda_z^2} \frac{\lambda_y^2}{\lambda_z^2} \overline{I}_{xyz}}{1 - \varepsilon_D + \frac{3\varepsilon_D}{2} \frac{\lambda_y^2}{\lambda_z^2} \overline{I}_{zy}}, \\
\frac{2n_0 g_s}{m} C_{xx,zz} &= \omega_y^2 \frac{\lambda_y^2}{\lambda_x^2} \frac{(1-\varepsilon_D) + \frac{9}{2}\varepsilon_D \frac{\lambda_x^2}{\lambda_z^2} \overline{I}_{xzz}}{1 - \varepsilon_D + \frac{3\varepsilon_D}{2} \frac{\lambda_y^2}{\lambda_z^2} \overline{I}_{zy}},
\end{aligned}$$

$$\begin{aligned}
\frac{2n_0g_s}{m}C_{yy,xx} &= \omega_y^2\frac{(1-\varepsilon_D)+\frac{3}{2}\varepsilon_D\frac{\lambda_x^2}{\lambda_z^2}\frac{\lambda_y^2}{\lambda_z^2}\overline{I}_{xyz}}{1-\varepsilon_D+\frac{3\varepsilon_D}{2}\frac{\lambda_y^2}{\lambda_z^2}\overline{I}_{zy}},\\
\frac{2n_0g_s}{m}C_{yy,yy} &= \omega_y^2\frac{3\,(1-\varepsilon_D)+\frac{9}{2}\varepsilon_D\frac{\lambda_y^4}{\lambda_z^4}\overline{I}_{yyz}}{1-\varepsilon_D+\frac{3\varepsilon_D}{2}\frac{\lambda_y^2}{\lambda_z^2}\overline{I}_{zy}},\\
\frac{2n_0g_s}{m}C_{yy,zz} &= \omega_y^2\frac{(1-\varepsilon_D)+\frac{3}{2}\varepsilon_D\frac{\lambda_y^2}{\lambda_z^2}\overline{I}_{yzz}}{1-\varepsilon_D+\frac{3\varepsilon_D}{2}\frac{\lambda_y^2}{\lambda_z^2}\overline{I}_{zy}},\\
\frac{2n_0g_s}{m}C_{zz,xx} &= \omega_y^2\frac{\lambda_y^2}{\lambda_z^2}\frac{(1-\varepsilon_D)+\frac{9}{2}\varepsilon_D\frac{\lambda_x^2}{\lambda_z^2}\overline{I}_{xzz}}{1-\varepsilon_D+\frac{3\varepsilon_D}{2}\frac{\lambda_y^2}{\lambda_z^2}\overline{I}_{zy}},\\
\frac{2n_0g_s}{m}C_{zz,yy} &= \omega_y^2\frac{\lambda_y^2}{\lambda_z^2}\frac{(1-\varepsilon_D)+\frac{3}{2}\varepsilon_D\frac{\lambda_y^2}{\lambda_z^2}\overline{I}_{yzz}}{1-\varepsilon_D+\frac{3\varepsilon_D}{2}\frac{\lambda_y^2}{\lambda_z^2}\overline{I}_{zy}},\\
\frac{2n_0g_s}{m}C_{zz,zz} &= \omega_y^2\frac{\lambda_y^2}{\lambda_z^2}\frac{3\,(1-\varepsilon_D)+\frac{45}{2}\varepsilon_D\overline{I}_{zzz}}{1-\varepsilon_D+\frac{3\varepsilon_D}{2}\frac{\lambda_y^2}{\lambda_z^2}\overline{I}_{zy}},
\end{aligned}$$

$$\frac{2n_0g_s}{m}C_{xz,xz} = \omega_y^2\left(\frac{\lambda_y^2}{\lambda_x^2}+\frac{\lambda_y^2}{\lambda_z^2}\right)\frac{(1-\varepsilon_D)+\frac{9}{2}\varepsilon_D\frac{\lambda_x^2}{\lambda_z^2}\overline{I}_{xzz}}{1-\varepsilon_D+\frac{3\varepsilon_D}{2}\frac{\lambda_y^2}{\lambda_z^2}\overline{I}_{zy}},$$

$$\begin{aligned}
\frac{2n_0g_s}{m}C_{yz,yz} &= \omega_y^2\left(1+\frac{\lambda_y^2}{\lambda_z^2}\right)\frac{(1-\varepsilon_D)+\frac{9}{2}\varepsilon_D\frac{\lambda_y^2}{\lambda_z^2}\overline{I}_{yzz}}{1-\varepsilon_D+\frac{3\varepsilon_D}{2}\frac{\lambda_y^2}{\lambda_z^2}\overline{I}_{zy}},\\
\frac{2n_0g_s}{m}C_{xy,xy} &= \omega_y^2\left(1+\frac{\lambda_y^2}{\lambda_x^2}\right)\frac{(1-\varepsilon_D)+\frac{3}{2}\varepsilon_D\frac{\lambda_x^2}{\lambda_z^2}\frac{\lambda_y^2}{\lambda_z^2}\overline{I}_{xyz}}{1-\varepsilon_D+\frac{3\varepsilon_D}{2}\frac{\lambda_y^2}{\lambda_z^2}\overline{I}_{zy}}.
\end{aligned}$$

Note, the index integrals used in the above expression for $C_{ab,cd}$ are defined slightly different than the index integrals defined in this thesis. The index integrals $\bar{I}$ are defined as

$$\bar{I}_{ab} = \frac{\lambda_x\lambda_y}{\lambda_z^2}\int_0^\infty \frac{\mathrm{d}u}{\sqrt{\left(\frac{\lambda_x^2}{\lambda_z^2}+u\right)\left(\frac{\lambda_y^2}{\lambda_z^2}+u\right)(1+u)}}\frac{1}{\left(\frac{\lambda_a^2}{\lambda_z^2}+u\right)}\frac{1}{\left(\frac{\lambda_b^2}{\lambda_z^2}+u\right)}$$

and

$$\bar{I}_{abc} = \frac{\lambda_x\lambda_y}{\lambda_z^2}\int_0^\infty \frac{\mathrm{d}u}{\sqrt{\left(\frac{\lambda_x^2}{\lambda_z^2}+u\right)\left(\frac{\lambda_y^2}{\lambda_z^2}+u\right)(1+u)}}\frac{1}{\left(\frac{\lambda_a^2}{\lambda_z^2}+u\right)}\frac{1}{\left(\frac{\lambda_b^2}{\lambda_z^2}+u\right)}\frac{1}{\left(\frac{\lambda_c^2}{\lambda_z^2}+u\right)}.$$

Appendix B

The index integrals

Throughout this whole work, the index integrals I as well as J need to be calculated. In Ref. [110] Carlson presents a method to numerically solve this type of elliptic integrals. In Ref. [94] an algorithm is presented to solve integrals of the form

$$F(x,y,z) = \int_0^\infty \mathrm{d}u \, \frac{1}{(x+u)^{1/2}} \frac{1}{(y+u)^{1/2}} \frac{1}{(z+u)^{3/2}}.$$

Obviously, the integral F is connected to the single index integrals I_a, which were defined in (1.28) and (1.29). Permutation of the three arguments of F gives the three different index integrals:

$$\begin{aligned} I_x\left(\lambda_x^2,\lambda_y^2,\lambda_z^2\right) &= F\left(\lambda_y^2,\lambda_z^2,\lambda_x^2\right), \\ I_y\left(\lambda_x^2,\lambda_y^2,\lambda_z^2\right) &= F\left(\lambda_z^2,\lambda_x^2,\lambda_y^2\right), \\ I_z\left(\lambda_x^2,\lambda_y^2,\lambda_z^2\right) &= F\left(\lambda_x^2,\lambda_y^2,\lambda_z^2\right). \end{aligned}$$

Furthermore, there are algebraic relations between the index integrals, that make it unnecessary to calculate all of them separately. The properties that follow here, have been previously discussed in Refs. [56, 57, 87]. For the single index integrals holds the relation

$$I_x + I_y + I_z = \frac{2}{\lambda_x\lambda_y\lambda_z},$$

and for the double index integrals it reads

$$2I_{aa} + I_{ax} + I_{ay} + I_{az} = \frac{2}{\lambda_x\lambda_y\lambda_z}\frac{1}{\lambda_a^2}.$$

These sum rules immediately yield the result for the case that $\lambda_x = \lambda_y = \lambda_z$:

$$I_x = I_y = I_z = \frac{2}{3\lambda_x^3},$$

and

$$I_{xx} = I_{yy} = I_{zz} = \frac{2}{5\lambda_x^5}.$$

Considering an uni-axial BEC with $\lambda_x = \lambda_y \neq \lambda_z$, the index integrals can still be solved analytically. The solutions are given by

$$I_x = I_y = -\frac{\frac{\lambda_z}{\lambda_x}\sqrt{1-\frac{\lambda_z^2}{\lambda_x^2}} + \arcsin\left(\frac{\lambda_z}{\lambda_x}\right) - \frac{\pi}{2}}{\left(\lambda_x^2 - \lambda_z^2\right)^{3/2}},$$

and

$$I_z = 2\frac{\sqrt{\frac{\lambda_x^2}{\lambda_z^2}-1} + \arcsin\left(\frac{\lambda_z}{\lambda_x}\right) - \frac{\pi}{2}}{\left(\lambda_x^2 - \lambda_z^2\right)^{3/2}}.$$

Consider next the index integrals J, defined in (3.21) and (3.22), which are needed to calculate the mirror potential. Actually, I is merely a special case of J, namely for $W = 0$. The integral F defined above can also be used to calculate J_a. One simply needs to use the arguments $\lambda_a^2 + W$ instead of λ_a^2:

$$J_a\left(\lambda_x^2, \lambda_y^2, \lambda_z^2\right) = I_a\left(\lambda_x^2 + W, \lambda_y^2 + W, \lambda_z^2 + W\right).$$

The sum rule for the single index integrals needs to be modified and reads

$$J_x + J_y + J_z = \frac{2}{\sqrt{\left(\lambda_x^2 + W\right)\left(\lambda_y^2 + W\right)\left(\lambda_z^2 + W\right)}}.$$

The double index integrals J_{ab}, needed for the calculation of the mirror potential, are constructed from single index integrals J_a. The connection is given by

$$J_{ab} = -\frac{J_a - J_b}{\lambda_a^2 - \lambda_b^2}.$$

This relation can of course only be used if $\lambda_a \neq \lambda_b$. For the case $\lambda_a = \lambda_b \neq \lambda_c$, an analytical solution is given by

$$J_{ab} = \frac{-\sqrt{\lambda_c^2 + W}\left(5\lambda_a^2 - 2\lambda_c^2 + 3W\right)}{4\left(\lambda_a^2 + W\right)^2\left(\lambda_a^2 - \lambda_c^2\right)^2} + \frac{3}{8}\frac{\pi - 2\arcsin\sqrt{\frac{\lambda_c^2+W}{\lambda_a^2+W}}}{\left(\lambda_a^2 - \lambda_c^2\right)^{5/2}}. \qquad \text{(B.1)}$$

There exists also a sum rule for the double index integrals J_{ab}, it reads

$$\frac{2}{\sqrt{\left(\lambda_x^2+W\right)\left(\lambda_y^2+W\right)\left(\lambda_z^2+W\right)}}\frac{1}{\left(\lambda_a^2+W\right)}$$

$$= 2J_{aa} + J_{ax} + J_{ay} + J_{az},, \quad a \in \{x, y, z\},$$

which yields for example

$$J_{zz} = \frac{2}{3\sqrt{\left(\lambda_x^2+W\right)\left(\lambda_y^2+W\right)\left(\lambda_z^2+W\right)\left(\lambda_z^2+W\right)}} - \frac{J_{xz}+J_{yz}}{3}.$$

Again, the sum rule is used to calculate J_{aa} for the case $\lambda_x = \lambda_y = \lambda_z$. The result is given by

$$J_{xx} = J_{yy} = J_{zz} = \frac{2}{5\left(\lambda_x^2+W\right)^{5/2}}.$$

For $W = 0$ the result for I is reproduced.

The here listed properties together with Carson's method [110] are used in the numerical solution of the GPE (3.28), in order to effectively calculate the mirror potential.

Appendix C

Frequency shift generated by a three dimensional TF ellipsoid

In order to determine the center-of-mass frequency shift of the BEC, caused by the interaction with the superconducting surface via the potential $V_{\rm mir}$, the second derivative of $V_{\rm mir}$ needs to be calculated. Furthermore, the fourth derivative is also required if large amplitude corrections need to be calculated. To simplify the matter, assume that the BEC is cylindrically symmetric about the z-axis, meaning the semi axes in the x- and y-direction are equal: $\lambda_x = \lambda_y$. As was shown in Chapter 3, the interaction potential $V_{\rm mir}$ is proportional to $\varphi_{\rm mir}(\mathbf{r})$, which is given by

$$\begin{aligned}\varphi_{\rm mir}(\mathbf{r}) &= \frac{\partial^2 \phi_{\rm mir}(\mathbf{r})}{\partial z^2} = -\frac{1}{2}\left(J_z - J_{xz}x^2 - J_{yz}y^2 - 3J_{zz}z^2\right) \\ &= \frac{\lambda_x\lambda_y\lambda_z}{8}\int\limits_{W(\mathbf{r})}^{\infty} \mathrm{d}u\, \frac{\partial^2 \alpha(\mathbf{r},\, u)}{\partial z^2}.\end{aligned}$$

It is convenient to define

$$\beta(\mathbf{r},\, u) = \frac{\partial^2 \alpha(\mathbf{r},\, u)}{\partial z^2} = -4\frac{\left(1 - \frac{x^2}{\lambda_x^2+u} - \frac{y^2}{\lambda_y^2+u} - 3\frac{z^2}{\lambda_z^2+u}\right)}{(\lambda_z^2+u)\sqrt{(\lambda_x^2+u)\left(\lambda_y^2+u\right)(\lambda_z^2+u)}}, \quad \text{(C.1)}$$

which gives

$$\varphi_{\rm mir}(\mathbf{r}) = \frac{\lambda_x\lambda_y\lambda_z}{8}\int\limits_{W(\mathbf{r})}^{\infty} \mathrm{d}u\, \beta(\mathbf{r},\, u)\,. \quad \text{(C.2)}$$

Omitting the factor before the integral, the Leibniz rule yields for the first derivative

$$\frac{\partial}{\partial x}\int\limits_{W(\mathbf{r})}^{\infty}\mathrm{d}u\,\beta\left(\mathbf{r},\,u\right)=-\beta\left(\mathbf{r},\,W\left(\mathbf{r}\right)\right)\frac{\partial W\left(\mathbf{r}\right)}{\partial x}+\int\limits_{W(\mathbf{r})}^{\infty}\mathrm{d}u\,\frac{\partial\beta\left(\mathbf{r},\,u\right)}{\partial x}. \tag{C.3}$$

To evaluate $\beta\left(\mathbf{r},\,W\left(\mathbf{r}\right)\right)$, definition (3.15) of $W\left(\mathbf{r}\right)$ is used:

$$\begin{aligned}\beta\left(\mathbf{r},\,W\left(\mathbf{r}\right)\right) &= 4\frac{\frac{2z^2}{\left(\lambda_z^2+W(\mathbf{r})\right)}-\left(1-\frac{x^2}{\left(\lambda_x^2+W(\mathbf{r})\right)}-\frac{y^2}{\left(\lambda_y^2+W(\mathbf{r})\right)}-\frac{z^2}{\left(\lambda_z^2+W(\mathbf{r})\right)}\right)}{\left(\lambda_z^2+W\left(\mathbf{r}\right)\right)\sqrt{\left(\lambda_x^2+W\left(\mathbf{r}\right)\right)\left(\lambda_y^2+W\left(\mathbf{r}\right)\right)\left(\lambda_z^2+W\left(\mathbf{r}\right)\right)}}\\ &= \frac{8z^2}{\left(\lambda_z^2+W\left(\mathbf{r}\right)\right)^{5/2}\left(\lambda_x^2+W\left(\mathbf{r}\right)\right)}\\ &= 8z^2\eta\left(W\left(\mathbf{r}\right)\right).\end{aligned}$$

The expression simplifies considerably, however, it does not vanish entirely as it was the case for the function $\alpha\left(\mathbf{r},u\right)$ in Section 4.1.1. In the second line the symmetry $\lambda_x=\lambda_y$ was used to further simplify the expression. And finally, in the last line the function

$$\eta\left(u\right)=\frac{1}{\left(\lambda_x^2+u\right)\left(\lambda_z^2+u\right)^{5/2}} \tag{C.4}$$

was introduced. For the second derivative the expression reads

$$\begin{aligned}\frac{\partial^2}{\partial x^2}\int\limits_{W(\mathbf{r})}^{\infty}\mathrm{d}u\,\beta\left(\mathbf{r},\,u\right) &= -\frac{\partial}{\partial x}\left(8z^2\eta\left(W\left(\mathbf{r}\right)\right)\frac{\partial W\left(\mathbf{r}\right)}{\partial x}\right)+\frac{\partial}{\partial x}\int\limits_{W(\mathbf{r})}^{\infty}\mathrm{d}u\,\frac{\partial\beta\left(\mathbf{r},\,u\right)}{\partial x}\\ &= -8z^2\frac{\partial\eta\left(W\left(\mathbf{r}\right)\right)}{\partial W\left(\mathbf{r}\right)}\left(\frac{\partial W\left(\mathbf{r}\right)}{\partial x}\right)^2\\ &\quad -8z^2\eta\left(W\left(\mathbf{r}\right)\right)\frac{\partial^2 W\left(\mathbf{r}\right)}{\partial x^2}\\ &\quad -\frac{\partial}{\partial x}\beta\left(\mathbf{r},\,u\right)\Big|_{u=W(\mathbf{r})}\frac{\partial W\left(\mathbf{r}\right)}{\partial x}\\ &\quad +\int\limits_{W(\mathbf{r})}^{\infty}\mathrm{d}u\,\frac{\partial^2}{\partial x^2}\beta\left(\mathbf{r},\,u\right).\end{aligned} \tag{C.5}$$

In this expression appears a number of terms which need to be evaluated. The derivatives of $\beta(\mathbf{r},\, u)$ are expressed as

$$\begin{aligned}\frac{\partial\beta(\mathbf{r},\, u)}{\partial x} &= -4\frac{\partial}{\partial x}\frac{\left(1-\frac{x^2}{\lambda_x^2+u}-\frac{y^2}{\lambda_y^2+u}-3\frac{z^2}{\lambda_z^2+u}\right)}{(\lambda_z^2+u)\sqrt{(\lambda_x^2+u)\left(\lambda_y^2+u\right)(\lambda_z^2+u)}} \\ &= \frac{8x}{(\lambda_x^2+u)^2(\lambda_z^2+u)^{3/2}} \\ &= 8x\cdot\xi(u) \end{aligned} \tag{C.6}$$

and

$$\frac{\partial^2\beta(\mathbf{r},\, u)}{\partial x^2} = 8\cdot\xi(u)\,. \tag{C.7}$$

Again the symmetry $\lambda_x = \lambda_y$ was used to simplify the expression. Furthermore the function

$$\xi(u) = \frac{1}{(\lambda_x^2+u)^2(\lambda_z^2+u)^{3/2}} \tag{C.8}$$

was introduced. Inserting everything back in expression (C.5) yields

$$\frac{\partial^2}{\partial x^2}\int\limits_{W(\mathbf{r})}^{\infty}\mathrm{d}u\,\beta(\mathbf{r},\, u) = 8\cdot F(\mathbf{r})\,,$$

with

$$\begin{aligned}F(\mathbf{r}) &= -z^2\eta(W(\mathbf{r}))\left[\frac{\partial\eta(W(\mathbf{r}))}{\partial W(\mathbf{r})}\left(\frac{\partial W(\mathbf{r})}{\partial x}\right)^2+\frac{\partial^2 W(\mathbf{r})}{\partial x^2}\right] \\ &\quad -x\cdot\xi(W(\mathbf{r}))\frac{\partial W(\mathbf{r})}{\partial x}+\int\limits_{W(\mathbf{r})}^{\infty}\mathrm{d}u\,\xi(u)\,. \end{aligned} \tag{C.9}$$

The second derivative of $\varphi_{\mathrm{mir}}(\mathbf{r})$ is mainly given by the function $F(\mathbf{r})$. Although F is a very complicated function of the position $\mathbf{r}$, it is still useful to have it. In the case of an uni-axial ellipsoid, it is possible to calculate F completely analytical. it is even possible to give a closed expression for the elliptic coordinate

$$\begin{aligned}W(\mathbf{r}) &= \frac{1}{2}\Bigg(x^2+y^2+z^2-\lambda_x^2-\lambda_z^2 \\ &\quad +\sqrt{(x^2+y^2+z^2-\lambda_x^2-\lambda_z^2)^2+4\left(z^2\lambda_x^2+x^2\lambda_z^2+y^2\lambda_z^2-\lambda_x^2\lambda_z^2\right)}\Bigg). \end{aligned}$$

It is very convenient to have an analytical expression for F, since in order to determine the frequency shift it is necessary to integrate F over the BEC density distribution. This integral can no longer be solved analytically and also the reduction to one dimensional index integrals is not possible.

The large amplitude corrections in expression (4.10) require also the derivatives of F. The first derivative of F reads

$$\begin{aligned}\frac{\partial F(\mathbf{r})}{\partial x} &= \Bigg[-z^2 \frac{\partial^2 \eta(W)}{\partial W^2} \left(\frac{\partial W}{\partial x}\right)^3 - 3z^2 \frac{\partial \eta(W)}{\partial W} \frac{\partial W}{\partial x} \frac{\partial^2 W}{\partial x^2} \\ &\quad -z^2 \eta(W) \frac{\partial^3 W}{\partial x^3} - \xi(W) \frac{\partial W}{\partial x} - x \frac{\partial \xi(W)}{\partial W(\mathbf{r})} \left(\frac{\partial W}{\partial x}\right)^2 \\ &\quad -x\xi(W) \frac{\partial^2 W}{\partial x^2} - \xi(W) \frac{\partial W}{\partial x} \Bigg], \end{aligned} \tag{C.10}$$

and the second derivative reads

$$\begin{aligned}\frac{\partial^2 F(\mathbf{r})}{\partial x^2} &= \Bigg[-z^2 \frac{\partial^3 \eta(W)}{\partial W^3} \left(\frac{\partial W}{\partial x}\right)^4 - 6z^2 \frac{\partial^2 \eta(W)}{\partial W^2} \left(\frac{\partial W}{\partial x}\right)^2 \frac{\partial^2 W}{\partial x^2} \\ &\quad -3z^2 \frac{\partial \eta(W)}{\partial W} \left(\frac{\partial^2 W}{\partial x^2}\right)^2 - 4z^2 \frac{\partial \eta(W)}{\partial W} \frac{\partial W}{\partial x} \frac{\partial^3 W}{\partial x^3} \\ &\quad -z^2 \eta(W) \frac{\partial^4 W}{\partial x^4} - x\xi(W) \frac{\partial^3 W}{\partial x^3} \\ &\quad -3x \frac{\partial \xi(W)}{\partial W} \frac{\partial W}{\partial x} \frac{\partial^2 W}{\partial x^2} - x \frac{\partial^2 \xi(W)}{\partial W^2} \left(\frac{\partial W}{\partial x}\right)^3 \\ &\quad -3\xi(W) \frac{\partial^2 W}{\partial x^2} - 3 \frac{\partial \xi(W)}{\partial W} \left(\frac{\partial W}{\partial x}\right)^2 \Bigg] \end{aligned} \tag{C.11}$$

In evaluating this expression one can make use of the fact that the deriva-

tives of the functions η and ξ can be written as

$$\begin{aligned}
\frac{\partial \eta(u)}{\partial u} &= \left\{ -\frac{5}{2}\frac{1}{(\lambda_z^2+u)} - \frac{1}{(\lambda_x^2+u)} \right\} \eta(u), \\
\frac{\partial^2 \eta(u)}{\partial u^2} &= \left\{ \frac{35}{4}\frac{1}{(\lambda_z^2+u)^2} + 5\frac{1}{(\lambda_z^2+u)}\frac{1}{(\lambda_x^2+u)} + 2\frac{1}{(\lambda_x^2+u)^2} \right\} \eta(u), \\
\frac{\partial^3 \eta(u)}{\partial u^3} &= \left\{ \begin{array}{c} -\frac{315}{8}\frac{1}{(\lambda_z^2+u)^3} - \frac{105}{4}\frac{1}{(\lambda_z^2+u)^2}\frac{1}{(\lambda_x^2+u)} \\ -15\frac{1}{(\lambda_z^2+u)}\frac{1}{(\lambda_x^2+u)^2} - 6\frac{1}{(\lambda_x^2+u)^3} \end{array} \right\} \eta(u), \\
\frac{\partial \xi(u)}{\partial u} &= \left\{ -2\frac{1}{(\lambda_x^2+u)} - \frac{3}{2}\frac{1}{(\lambda_z^2+u)} \right\} \xi(u), \\
\frac{\partial^2 \xi(u)}{\partial u^2} &= \left\{ 6\frac{1}{(\lambda_x^2+u)^2} + 6\frac{1}{(\lambda_x^2+u)}\frac{1}{(\lambda_z^2+u)} + \frac{15}{4}\frac{1}{(\lambda_z^2+u)^2} \right\} \xi(u).
\end{aligned}$$

With all that has been said, expression (4.10) for the frequency shift is written as

$$\begin{aligned}
\gamma &= \frac{1}{2\omega_x^2 mN} \int d\mathbf{r}\, n_{\mathrm{TF}}(\mathbf{r}) \left\{ 4\frac{\partial^2 V_{\mathrm{mir}}(\mathbf{r})}{\partial x^2} + 16\frac{x_s^2}{8}\frac{\partial^4 V_{\mathrm{mir}}(\mathbf{r})}{\partial x^4} \right\} \\
&= -\frac{3\varepsilon_D^{(m)} g_s n_0}{2\omega_x^2 mN} \int d\mathbf{r}\, n_{\mathrm{TF}}(\mathbf{r}) \left\{ 4\frac{\partial^2 \varphi_{\mathrm{mir}}(\mathbf{r})}{\partial x^2} + 2x_s^2\frac{\partial^4 \varphi_{\mathrm{mir}}(\mathbf{r})}{\partial x^4} \right\} \\
&= -\frac{3\varepsilon_D^{(m)} g_s n_0}{2\omega_x^2 mN}\frac{\lambda_x^2\lambda_z}{8} \int d\mathbf{r}\, n_{\mathrm{TF}}(\mathbf{r}) \left\{ 4\frac{\partial^2}{\partial x^2} \int\limits_{W(\mathbf{r})}^{\infty} \mathrm{d}u\, \beta(\mathbf{r},\, u) + 2x_s^2\frac{\partial^4}{\partial x^4} \int\limits_{W(\mathbf{r})}^{\infty} \mathrm{d}u\, \beta(\mathbf{r},\, u) \right\} \\
&= -4\frac{3\varepsilon_D^{(m)} g_s n_0}{2\omega_x^2 mN}\lambda_x^2\lambda_z \int d\mathbf{r}\, n_{\mathrm{TF}}(\mathbf{r}) \left\{ F(\mathbf{r}) + \frac{x_s^2}{2}\frac{\partial^2 F(\mathbf{r})}{\partial x^2} \right\}. \qquad \text{(C.12)}
\end{aligned}$$

The factor before the integral is rewritten, so that it only contains the semi axes, the parameter $\varepsilon_D^{(m)}$ and the the number of atoms N:

$$6\varepsilon_D^{(m)}\frac{g_s}{m\omega_x^2} n_0 \frac{\lambda_x^2\lambda_z}{N} = 3\varepsilon_D^{(m)} \underbrace{\frac{2g_s n_0^{(0)}}{m\omega_x^2}}_{=\left[\lambda_x^{(0)}\right]^2} \frac{n_0}{n_0^{(0)}}\frac{\lambda_x^2\lambda_z}{N} = 3\varepsilon_D^{(m)} \left[\lambda_x^{(0)}\right]^4 \lambda_z^{(0)}\frac{1}{N}.$$

This gives the final result for the frequency shift

$$\begin{aligned}\gamma &= -3\varepsilon_D^{(m)}\left[\lambda_x^{(0)}\right]^3\lambda_y^{(0)}\lambda_z^{(0)}\frac{1}{N}\int d\mathbf{r}\, n_{\mathrm{TF}}(\mathbf{r})\left\{F(\mathbf{r})+\frac{x_s^2}{2}\frac{\partial^2 F(\mathbf{r})}{\partial x^2}\right\}\\ &= -\frac{45}{8\pi}\varepsilon_D^{(m)}\frac{\left[\lambda_x^{(0)}\right]^3\lambda_y^{(0)}\lambda_z^{(0)}}{\lambda_x\lambda_y\lambda_z}\int d\mathbf{r}\,\rho_{\mathrm{TF}}(\mathbf{r})\left\{F(\mathbf{r})+\frac{x_s^2}{2}\frac{\partial^2 F(\mathbf{r})}{\partial x^2}\right\},\end{aligned}$$

with $\rho_{\mathrm{TF}}(\mathbf{r}) = n_{\mathrm{TF}}(\mathbf{r})/n_0$. Note, the factors 4 and 16, discussed at the end of Section 4.1, were already included in the above expression.

Appendix D

Derivation of the time-dependent trap frequencies

In the following it is shown how the time dependent harmonic trap frequencies (5.2) can be derived. First a Taylor expansion of the potential generated by the mirror BEC about the minimum of the harmonic trapping potential is calculated. This expansion is performed in the laboratory frame, where the BEC center-of-mass performs a harmonic oscillation. It is useful to first discuss the different orders of the series expansion and the terms that are important for the time dependent trap frequencies. The harmonic trap frequencies are connected to the curvature of the potential. In order to affect the frequency in a certain direction, say the z-direction, the term needs to be proportional to z^2, for example xz^2. Now this term needs to be transformed in the frame of reference where the center-of-mass is at rest. In the following, the primed coordinates a' denote the coordinates of the co-moving frame and the plain coordinates a denote the coordinates of the resting laboratory frame. From the transformation rule $x = x' + x_s \sin(\omega_x' t)$, one can see this term gets a time dependent component $x_s \sin(\omega_x' t) \cdot z^2$, which varies with the single oscillation frequency ω_x'. With that an effective, time dependent trap frequency $\Omega_z(t)$ is defined. Of course, this is not the only term that contributes to the time dependent trap frequencies. In the following, all the terms that contribute to the effective trap frequencies are transformed and discussed. The first term reads

$$xa^2 = x'a'^2 + a'^2 x_s \sin(\omega_x' t), \quad a \in \{y, z\},$$

which gives a term proportional to y'^2 and z'^2, containing a time dependent factor. This means one can define effective, time dependent trap frequencies $\Omega_y(t)$ and $\Omega_z(t)$ for the y- and z-direction. The time dependent factor creates a modulation of $\Omega_y(t)$ and $\Omega_z(t)$ with the center-of-mass oscillation frequency ω'_x. The terms $x'y'^2$ and $x'z'^2$ are dropped, since they do not fit in the scheme of time dependent trap frequencies. From the cubic term in x one finds

$$x^3 = x'^3 + 3x'^2 x_s \sin(\omega'_x t) + 3x' x_s^2 \sin^2(\omega'_x t) + x_s^3 \sin^3(\omega'_x t),$$

which yields a quadratic term in x' with a time dependent factor. This term is connected to an effective trap frequency in the x-direction $\Omega_x(t)$. All the other terms in this expression are dropped. Finally, the terms of fourth order need to be transformed. The first one reads

$$x^2 a^2 = a'^2 x'^2 + 2x' a'^2 x_s \sin(\omega'_x t) + a'^2 x_s^2 \sin^2(\omega'_x t), \qquad \text{with} \quad a \in \{y, z\}.$$

This gives a term proportional to y'^2 and z'^2, with a time dependent factor $\sin^2(\omega'_x t)$. This leads to an additional term in $\Omega_y(t)$ and $\Omega_z(t)$, which varies with the double oscillation frequency $2\omega'_x$. Again, all the other terms are dropped in this expression which do not fit in the harmonic scheme. The last term of interest is

$$\begin{aligned} x^4 &= x'^4 + 4x'^3 x_s \sin(\omega'_x t) + 6x'^2 x_s^2 \sin^2(\omega'_x t) \\ &\quad + 4x' x_s^3 \sin^3(\omega'_x t) + x_s^4 \sin^4(\omega'_x t). \end{aligned}$$

Here a quadratic term in x' is found, which generates a modulation of $\Omega_x(t)$ with $2\omega'_x$, all other terms are dropped. Now that all important term have been identified, the correct coefficients need to be determined. The terms from the Taylor series expansion yield

$$\frac{1}{2!\cdot 1!}\, 2 \frac{\partial^3 V_{\mathrm{mir}}(\mathbf{r}')}{\partial x' \partial y'^2}\bigg|_{\mathbf{r}'=2x_d\hat{\mathbf{e}}_x} xy^2 \equiv \frac{1}{2} V_{x,yy} xy^2,$$

$$\frac{1}{2!\cdot 1!}\, 2 \frac{\partial^3 V_{\mathrm{mir}}(\mathbf{r}')}{\partial x' \partial z'^2}\bigg|_{\mathbf{r}'=2x_d\hat{\mathbf{e}}_x} xz^2 \equiv \frac{1}{2} V_{x,zz} xz^2,$$

$$\frac{1}{3!}\, 8 \frac{\partial^3 V_{\mathrm{mir}}(\mathbf{r}')}{\partial x'^3}\bigg|_{\mathbf{r}'=2x_d\hat{\mathbf{e}}_x} x^3 \equiv \frac{1}{6} V_{x,xx} x^3,$$

$$\frac{1}{2!\cdot 2!}\, 4 \frac{\partial^4 V_{\mathrm{mir}}(\mathbf{r}')}{\partial x'^2 \partial y'^2}\bigg|_{\mathbf{r}'=2x_d\hat{\mathbf{e}}_x} x^2 y^2 \equiv \frac{1}{4} V_{xx,yy} x^2 y^2,$$

$$\frac{1}{2!\cdot 2!}\,4\frac{\partial^4 V_{\mathrm{mir}}\left(\mathbf{r}'\right)}{\partial x'^2\partial z'^2}\bigg|_{\mathbf{r}'=2x_d\hat{\mathbf{e}}_x} x^2z^2 \equiv \frac{1}{4}V_{xx,zz}x^2z^2,$$

and

$$\frac{1}{4!}\,16\frac{\partial^4 V_{\mathrm{mir}}\left(\mathbf{r}'\right)}{\partial x'^4}\bigg|_{\mathbf{r}'=2x_d\hat{\mathbf{e}}_x} x^4 \equiv \frac{1}{24}V_{xx,xx}x^4.$$

Again, the factors 2, 4, 8, and 16 are due to the fact that the derivative needs to be taken with respect to $x/2$ rather that to x. Those factors are included into the definitions of $V_{x,aa}$ and $V_{xx,aa}$. With that the expressions for the effective frequencies can be given. In order to define an effective frequency $\Omega_a\left(t\right)$ one needs to collect all terms (in the co-moving frame) that are proportional to a'^2:

$$\begin{aligned} U_a\left(a'\right) &= \frac{m}{2}\Bigg(\omega_a^2 + \frac{1}{m}V_{x,aa}x_s\sin\left(\omega_x' t\right) \\ &\quad + \frac{1}{2m}V_{xx,aa}x_s^2\sin^2\left(\omega_x' t\right)\Bigg)a'^2 \\ &= \frac{m}{2}\Omega_a^2\left(t\right)a'^2, \quad a' \in \left\{x', y', z'\right\}. \end{aligned}$$

The first term in this expression comes from the harmonic trap, the rest from the series expansion of the mirror potential.

Bibliography

[1] S. N. Bose. "Plancks Gesetz und Lichtquantenhypothese". *Z. Phys.*, **26**, 178 (1924).

[2] A. Einstein. "Quantentheorie des einatomigen idealen Gases". *Sitzungsber. Kgl. Preuss. Akad. Wiss.*, **261** (1924).

[3] K. B. Davis, M. O. Mewes, M. R. Andrews, N. J. van Druten, D. S. Durfee, D. M. Kurn, and W. Ketterle. "Bose-Einstein Condensation in a Gas of Sodium Atoms". *Phys. Rev. Lett.*, **75**, 3969–3973 (1995). URL `http://dx.doi.org/10.1103/PhysRevLett.75.3969`.

[4] M. H. Anderson, J. R. Ensher, M. R. Matthews, C. E. Wieman, and E. A. Cornell. "Observation of Bose-Einstein Condensation in a Dilute Atomic Vapor". *Science*, **269**, 5221, 198–201 (1995). URL `http://dx.doi.org/10.1126/science.269.5221.198`.

[5] A. Griesmaier, J. Werner, S. Hensler, J. Stuhler, and T. Pfau. "Bose-Einstein Condensation of Chromium". *Phys. Rev. Lett.*, **94**, 160401 (2005). URL `http://dx.doi.org/10.1103/PhysRevLett.94.160401`.

[6] T. Lahaye, C. Menotti, L. Santos, M. Lewenstein, and T. Pfau. "The physics of dipolar bosonic quantum gases". *Rep. Prog. Phys.*, **72**, 12, 126401 (2009). URL `http://stacks.iop.org/0034-4885/72/i=12/a=126401`.

[7] K. Aikawa, A. Frisch, M. Mark, S. Baier, A. Rietzler, R. Grimm, and F. Ferlaino. "Bose-Einstein Condensation of Erbium". *Phys. Rev. Lett.*, **108**, 210401 (2012). URL `http://dx.doi.org/10.1103/PhysRevLett.108.210401`.

[8] M. Lu, N. Q. Burdick, S. H. Youn, and B. L. Lev. "Strongly Dipolar Bose-Einstein Condensate of Dysprosium". *Phys. Rev. Lett.*, **107**,

190401 (2011). URL http://dx.doi.org/10.1103/PhysRevLett.107.190401.

[9] J. Fortágh and C. Zimmermann. "Magnetic microtraps for ultracold atoms". *Rev. Mod. Phys.*, **79**, 235–289 (2007). URL http://dx.doi.org/10.1103/RevModPhys.79.235.

[10] M. P. A. Jones, C. J. Vale, D. Sahagun, B. V. Hall, and E. A. Hinds. "Spin Coupling between Cold Atoms and the Thermal Fluctuations of a Metal Surface". *Phys. Rev. Lett.*, **91**, 080401 (2003). URL http://dx.doi.org/10.1103/PhysRevLett.91.080401.

[11] P. K. Rekdal, S. Scheel, P. L. Knight, and E. A. Hinds. "Thermal spin flips in atom chips". *Phys. Rev. A*, **70**, 013811 (2004). URL http://dx.doi.org/10.1103/PhysRevA.70.013811.

[12] K. Onnes. *Comm. Leiden*, **120b, 122b, 124c** (1911).

[13] W. Meissner and R. Ochsenfeld. *Naturwissenschaften*, **21**, 787 (1933).

[14] J. Bardeen, L. N. Cooper, and J. R. Schrieffer. "Theory of Superconductivity". *Phys. Rev.*, **108**, 1175–1204 (1957). URL http://dx.doi.org/10.1103/PhysRev.108.1175.

[15] J. F. Annett. *Superconductivity, superfluids, and condensates*. Oxford Univ. Press, Oxford, reprint. edition (2007).

[16] C. W. Chu, L. Gao, F. Chen, Z. J. Huang, R. L. Meng, and Y. Y. Xue. "Superconductivity above 150 K in $HgBa_2Ca_2Cu_3O_{8+\delta}$ at high pressures". *Nature*, **365**, 6444, 323–325 (1993). URL http://dx.doi.org/10.1038/365323a0.

[17] J. Bednorz and K. Müller. "Possible high T_c superconductivity in the Ba–La–Cu–O system". *Z. Phys. B Con. Mat.*, **64**, 2, 189–193 (1986). URL http://dx.doi.org/10.1007/BF01303701.

[18] M. K. Wu, J. R. Ashburn, C. J. Torng, P. H. Hor, R. L. Meng, L. Gao, Z. J. Huang, Y. Q. Wang, and C. W. Chu. "Superconductivity at 93 K in a new mixed-phase Y–Ba–Cu–O compound system at ambient pressure". *Phys. Rev. Lett.*, **58**, 908–910 (1987). URL http://dx.doi.org/10.1103/PhysRevLett.58.908.

[19] Z. Z. Sheng and A. M. Hermann. "Superconductivity in the rare-earth-free Tl–Ba–Cu–O system above liquid-nitrogen temperature".

Nature, **332**, 6159, 55–58 (1988). URL http://dx.doi.org/10.1038/332055a0.

[20] Z. Z. Sheng and A. M. Hermann. "Bulk superconductivity at 120 K in the Tl–Ca/Ba–Cu–O system". *Nature*, **332**, 6160, 138–139 (1988). URL http://dx.doi.org/10.1038/332138a0.

[21] H. Maeda, Y. Tanaka, M. Fukutomi, and T. Asano. "A New High-T_c Oxide Superconductor without a Rare Earth Element". *Jpn. J. Appl. Phys.*, **27**, 2A, L209 (1988). URL http://stacks.iop.org/1347-4065/27/i=2A/a=L209.

[22] L. Gao, Z. J. Huang, R. L. Meng, P. H. Hor, J. Bechtold, Y. Y. Sun, C. W. Chu, Z. Z. Sheng, and A. M. Hermann. "Bulk superconductivity in $Tl_2CaBa_2Cu_2O_{8+\delta}$ up to 120 K". *Nature*, **332**, 6165, 623–624 (1988). URL http://dx.doi.org/10.1038/332623a0.

[23] S. Hikami, T. Hirai, and S. Kagoshima. "High Transition Temperature Superconductor: Y–Ba–Cu Oxide". *Jpn. J. Appl. Phys.*, **26**, 4A, L314 (1987). URL http://stacks.iop.org/1347-4065/26/i=4A/a=L314.

[24] P. Phillips, T.-P. Choy, and R. G. Leigh. "Mottness in high-temperature copper-oxide superconductors". *Rep. Prog. Phys.*, **72**, 3, 036501 (2009). URL http://stacks.iop.org/0034-4885/72/i=3/a=036501.

[25] T. Nirrengarten, A. Qarry, C. Roux, A. Emmert, G. Nogues, M. Brune, J.-M. Raimond, and S. Haroche. "Realization of a Superconducting Atom Chip". *Phys. Rev. Lett.*, **97**, 200405 (2006). URL http://dx.doi.org/10.1103/PhysRevLett.97.200405.

[26] T. Mukai, C. Hufnagel, A. Kasper, T. Meno, A. Tsukada, K. Semba, and F. Shimizu. "Persistent Supercurrent Atom Chip". *Phys. Rev. Lett.*, **98**, 260407 (2007). URL http://dx.doi.org/10.1103/PhysRevLett.98.260407.

[27] D. Cano, B. Kasch, H. Hattermann, R. Kleiner, C. Zimmermann, D. Koelle, and J. Fortágh. "Meissner Effect in Superconducting Microtraps". *Phys. Rev. Lett.*, **101**, 183006 (2008). URL http://dx.doi.org/10.1103/PhysRevLett.101.183006.

[28] M. Siercke, K. S. Chan, B. Zhang, M. Beian, M. J. Lim, and R. Dumke. "Reconfigurable self-sufficient traps for ultracold atoms based on a

superconducting square". *Phys. Rev. A*, **85**, 041403 (2012). URL http://dx.doi.org/10.1103/PhysRevA.85.041403.

[29] B. Zhang, M. Siercke, K. S. Chan, M. Beian, M. J. Lim, and R. Dumke. "Magnetic confinement of neutral atoms based on patterned vortex distributions in superconducting disks and rings". *Phys. Rev. A*, **85**, 013404 (2012). URL http://dx.doi.org/10.1103/PhysRevA.85.013404.

[30] H. Imai, K. Inaba, H. Tanji-Suzuki, M. Yamashita, and T. Mukai. "Bose-Einstein condensate on a persistent-supercurrent atom chip". *Appl. Phys. B-Lasers O.*, **116**, 4, 821–829 (2014). URL http://dx.doi.org/10.1007/s00340-014-5768-3.

[31] R. Hanson and D. D. Awschalom. "Coherent manipulation of single spins in semiconductors". *Nature*, **453**, 7198, 1043–1049 (2008). URL http://dx.doi.org/10.1038/nature07129.

[32] J. Clarke and F. K. Wilhelm. "Superconducting quantum bits". *Nature*, **453**, 7198, 1031–1042 (2008). URL http://dx.doi.org/10.1038/nature07128.

[33] I. Bloch. "Quantum coherence and entanglement with ultracold atoms in optical lattices". *Nature*, **453**, 7198, 1016–1022 (2008). URL http://dx.doi.org/10.1038/nature07126.

[34] R. Blatt and D. Wineland. "Entangled states of trapped atomic ions". *Nature*, **453**, 7198, 1008–1015 (2008). URL http://dx.doi.org/10.1038/nature07125.

[35] H. Häffner, C. Roos, and R. Blatt. "Quantum computing with trapped ions". *Phys. Rep.*, **469**, 4, 155 – 203 (2008). URL http://dx.doi.org/10.1016/j.physrep.2008.09.003.

[36] Z.-L. Xiang, S. Ashhab, J. Q. You, and F. Nori. "Hybrid quantum circuits: Superconducting circuits interacting with other quantum systems". *Rev. Mod. Phys.*, **85**, 623–653 (2013). URL http://dx.doi.org/10.1103/RevModPhys.85.623.

[37] X. Zhu, S. Saito, A. Kemp, K. Kakuyanagi, S.-i. Karimoto, H. Nakano, W. J. Munro, Y. Tokura, M. S. Everitt, K. Nemoto, M. Kasu, N. Mizuochi, and K. Semba. "Coherent coupling of a superconducting flux qubit to an electron spin ensemble in diamond". *Nature*, **478**, 7368, 221–224 (2011). URL http://dx.doi.org/10.1038/nature10462.

[38] Y. Kubo, C. Grezes, A. Dewes, T. Umeda, J. Isoya, H. Sumiya, N. Morishita, H. Abe, S. Onoda, T. Ohshima, V. Jacques, A. Dréau, J.-F. Roch, I. Diniz, A. Auffeves, D. Vion, D. Esteve, and P. Bertet. "Hybrid Quantum Circuit with a Superconducting Qubit Coupled to a Spin Ensemble". *Phys. Rev. Lett.*, **107**, 220501 (2011). URL http://dx.doi.org/10.1103/PhysRevLett.107.220501.

[39] R. Amsüss, C. Koller, T. Nöbauer, S. Putz, S. Rotter, K. Sandner, S. Schneider, M. Schramböck, G. Steinhauser, H. Ritsch, J. Schmiedmayer, and J. Majer. "Cavity QED with Magnetically Coupled Collective Spin States". *Phys. Rev. Lett.*, **107**, 060502 (2011). URL http://dx.doi.org/10.1103/PhysRevLett.107.060502.

[40] A. D. O'Connell, M. Hofheinz, M. Ansmann, R. C. Bialczak, M. Lenander, E. Lucero, M. Neeley, D. Sank, H. Wang, M. Weides, J. Wenner, J. M. Martinis, and A. N. Cleland. "Quantum ground state and single-phonon control of a mechanical resonator". *Nature*, **464**, 7289, 697–703 (2010). URL http://dx.doi.org/10.1038/nature08967.

[41] H. Wu, R. E. George, J. H. Wesenberg, K. Mølmer, D. I. Schuster, R. J. Schoelkopf, K. M. Itoh, A. Ardavan, J. J. L. Morton, and G. A. D. Briggs. "Storage of Multiple Coherent Microwave Excitations in an Electron Spin Ensemble". *Phys. Rev. Lett.*, **105**, 140503 (2010). URL http://dx.doi.org/10.1103/PhysRevLett.105.140503.

[42] K. Henschel, J. Majer, J. Schmiedmayer, and H. Ritsch. "Cavity QED with an ultracold ensemble on a chip: Prospects for strong magnetic coupling at finite temperatures". *Phys. Rev. A*, **82**, 033810 (2010). URL http://dx.doi.org/10.1103/PhysRevA.82.033810.

[43] A. Andre, D. DeMille, J. M. Doyle, M. D. Lukin, S. E. Maxwell, P. Rabl, R. J. Schoelkopf, and P. Zoller. "A coherent all-electrical interface between polar molecules and mesoscopic superconducting resonators". *Nat. Phys.*, **2**, 9, 636–642 (2006). URL http://dx.doi.org/10.1038/nphys386.

[44] P. Rabl, D. DeMille, J. M. Doyle, M. D. Lukin, R. J. Schoelkopf, and P. Zoller. "Hybrid Quantum Processors: Molecular Ensembles as Quantum Memory for Solid State Circuits". *Phys. Rev. Lett.*, **97**, 033003 (2006). URL http://dx.doi.org/10.1103/PhysRevLett.97.033003.

[45] A. Wallraff, D. I. Schuster, A. Blais, L. Frunzio, R.-S. Huang, J. Majer, S. Kumar, S. M. Girvin, and R. J. Schoelkopf. "Strong coupling of a single photon to a superconducting qubit using circuit quantum electrodynamics". *Nature*, **431**, 7005, 162–167 (2004). URL http://dx.doi.org/10.1038/nature02851.

[46] G. Bensky, R. Amsüss, J. Majer, D. Petrosyan, J. Schmiedmayer, and G. Kurizki. "Controlling quantum information processing in hybrid systems on chips". *Quantum Inf. Process.*, **10**, 6, 1037–1060 (2011). URL http://dx.doi.org/10.1007/s11128-011-0302-6.

[47] R. Salem, Y. Japha, J. Chabé, B. Hadad, M. Keil, K. A. Milton, and R. Folman. "Nanowire atomchip traps for sub-micron atom-surface distances". *New J. Phys.*, **12**, 2, 023039 (2010). URL http://stacks.iop.org/1367-2630/12/i=2/a=023039.

[48] D. Cano, H. Hattermann, B. Kasch, C. Zimmermann, R. Kleiner, D. Koelle, and J. Fortágh. "Experimental system for research on ultracold atomic gases near superconducting microstructures". *Eur. Phys. J. D*, **63**, 1, 17–23 (2011). URL http://dx.doi.org/10.1140/epjd/e2011-10680-8.

[49] S. Bernon, H. Hattermann, D. Bothner, M. Knufinke, P. Weiss, F. Jessen, D. Cano, M. Kemmler, R. Kleiner, D. Koelle, and J. Fortágh. "Manipulation and coherence of ultra-cold atoms on a superconducting atom chip". *Nat. Commun.*, **4**, 2380 (2013). URL http://dx.doi.org/10.1038/ncomms3380.

[50] O. Romero-Isart, C. Navau, A. Sanchez, P. Zoller, and J. I. Cirac. "Superconducting Vortex Lattices for Ultracold Atoms". *Phys. Rev. Lett.*, **111**, 145304 (2013). URL http://dx.doi.org/10.1103/PhysRevLett.111.145304.

[51] D. Bothner, M. Knufinke, H. Hattermann, R. Wölbing, B. Ferdinand, P. Weiss, S. Bernon, J. Fortágh, D. Koelle, and R. Kleiner. "Inductively coupled superconducting half wavelength resonators as persistent current traps for ultracold atoms". *New J. Phys.*, **15**, 9, 093024 (2013). URL http://stacks.iop.org/1367-2630/15/i=9/a=093024.

[52] M. Antezza, L. P. Pitaevskii, and S. Stringari. "Effect of the Casimir-Polder force on the collective oscillations of a trapped Bose-Einstein

condensate". *Phys. Rev. A*, **70**, 053619 (2004). URL http://dx.doi.org/10.1103/PhysRevA.70.053619.

[53] D. M. Harber, J. M. Obrecht, J. M. McGuirk, and E. A. Cornell. "Measurement of the Casimir-Polder force through center-of-mass oscillations of a Bose-Einstein condensate". *Phys. Rev. A*, **72**, 033610 (2005). URL http://dx.doi.org/10.1103/PhysRevA.72.033610.

[54] I. Sapina. *The Effect of Eddy Currents in Superconducting Microtraps*. Diplomarbeit, Eberhard Karls Universität Tübingen (2010).

[55] I. Sapina and T. Dahm. "Interaction of a Bose-Einstein condensate and a superconductor via eddy currents". *New J. Phys.*, **15**, 7, 073035 (2013). URL http://stacks.iop.org/1367-2630/15/i=7/a=073035.

[56] I. Sapina and T. Dahm. "Dynamics of a dipolar Bose-Einstein condensate in the vicinity of a superconductor". *Phys. Rev. A*, **90**, 052709 (2014). URL http://dx.doi.org/10.1103/PhysRevA.90.052709.

[57] I. Sapina, T. Dahm, and N. Schopohl. "Ground-state and collective modes of a spin-polarized dipolar Bose-Einstein condensate in a harmonic trap". *Phys. Rev. A*, **82**, 053620 (2010). URL http://dx.doi.org/10.1103/PhysRevA.82.053620.

[58] R. Grimm, M. Weidemüller, and Y. B. Ovchinnikov. "Optical Dipole Traps for Neutral Atoms". *Adv. Atom. Mol. Opt. Phy.*, **42**, 95 – 170 (2000). URL http://dx.doi.org/10.1016/S1049-250X(08)60186-X.

[59] C. Pethick and H. Smith. *Bose-Einstein condensation in dilute gases*. Cambridge Univ. Press, New York, 2nd edition (2008).

[60] W. H. Wing. "On neutral particle trapping in quasistatic electromagnetic fields". *Prog. Quant. Electron.*, **8**, 3–4, 181 – 199 (1984). URL http://dx.doi.org/10.1016/0079-6727(84)90012-0.

[61] W. Ketterle and D. Pritchard. "Trapping and focusing ground state atoms with static fields". *Appl. Phys. B-Lasers O.*, **54**, 5, 403–406 (1992). URL http://dx.doi.org/10.1007/BF00325386.

[62] A. Günther. *Materiewellenoptik mit Bose-Einstein-Kondensaten auf Mikrochips*. Ph.D. thesis, Universität Tübingen (2008).

[63] J. Reichel. "Microchip traps and Bose–Einstein condensation". *Appl. Phys. B-Lasers O.*, **74**, 6, 469–487 (2002). URL http://dx.doi.org/10.1007/s003400200861.

[64] E. A. Hinds and I. G. Hughes. "Magnetic atom optics: mirrors, guides, traps, and chips for atoms". *J. Phys. D Appl. Phys.*, **32**, 18, R119 (1999). URL http://stacks.iop.org/0022-3727/32/i=18/a=201.

[65] C. Henkel, J. Schmiedmayer, and C. Westbrook. "Preface". *Eur. Phys. J. D*, **35**, 1, 1–2 (2005). URL http://dx.doi.org/10.1140/epjd/e2005-00183-8.

[66] D. Harber, J. McGuirk, J. Obrecht, and E. Cornell. "Thermally Induced Losses in Ultra-Cold Atoms Magnetically Trapped Near Room-Temperature Surfaces". *J. Low Temp. Phys.*, **133**, 3-4, 229–238 (2003). URL http://dx.doi.org/10.1023/A:1026084606385.

[67] Y.-j. Lin, I. Teper, C. Chin, and V. Vuletić. "Impact of the Casimir-Polder Potential and Johnson Noise on Bose-Einstein Condensate Stability Near Surfaces". *Phys. Rev. Lett.*, **92**, 050404 (2004). URL http://dx.doi.org/10.1103/PhysRevLett.92.050404.

[68] A. Emmert, A. Lupaşcu, G. Nogues, M. Brune, J.-M. Raimond, and S. Haroche. "Measurement of the trapping lifetime close to a cold metallic surface on a cryogenic atom-chip". *Eur. Phys. J. D*, **51**, 2, 173–177 (2009). URL http://dx.doi.org/10.1140/epjd/e2009-00001-5.

[69] B.-S. K. Skagerstam, U. Hohenester, A. Eiguren, and P. K. Rekdal. "Spin Decoherence in Superconducting Atom Chips". *Phys. Rev. Lett.*, **97**, 070401 (2006). URL http://dx.doi.org/10.1103/PhysRevLett.97.070401.

[70] U. Hohenester, A. Eiguren, S. Scheel, and E. A. Hinds. "Spin-flip lifetimes in superconducting atom chips: Bardeen-Cooper-Schrieffer versus Eliashberg theory". *Phys. Rev. A*, **76**, 033618 (2007). URL http://dx.doi.org/10.1103/PhysRevA.76.033618.

[71] R. Fermani, T. Müller, B. Zhang, M. J. Lim, and R. Dumke. "Heating rate and spin flip lifetime due to near-field noise in layered superconducting atom chips". *J. Phys. B-At. Mol. Opt.*, **43**, 9, 095002 (2010). URL http://stacks.iop.org/0953-4075/43/i=9/a=095002.

[72] B. Kasch, H. Hattermann, D. Cano, T. E. Judd, S. Scheel, C. Zimmermann, R. Kleiner, D. Koelle, and J. Fortágh. "Cold atoms near superconductors: atomic spin coherence beyond the Johnson noise limit". *New J. Phys.*, **12**, 6, 065024 (2010). URL http://stacks.iop.org/1367-2630/12/i=6/a=065024.

[73] A. Emmert, A. Lupaşcu, M. Brune, J.-M. Raimond, S. Haroche, and G. Nogues. "Microtraps for neutral atoms using superconducting structures in the critical state". *Phys. Rev. A*, **80**, 061604 (2009). URL http://dx.doi.org/10.1103/PhysRevA.80.061604.

[74] M. Tinkham. *Introduction to superconductivity*. Dover Publ., Mineola, NY, 2nd edition (2004).

[75] A. Markowsky, A. Zare, V. Graber, and T. Dahm. "Optimal thickness of rectangular superconducting microtraps for cold atomic gases". *Phys. Rev. A*, **86**, 023412 (2012). URL http://dx.doi.org/10.1103/PhysRevA.86.023412.

[76] V. Dikovsky, V. Sokolovsky, B. Zhang, C. Henkel, and R. Folman. "Superconducting atom chips: advantages and challenges". *Eur. Phys. J. D*, **51**, 2, 247–259 (2009). URL http://dx.doi.org/10.1140/epjd/e2008-00261-5.

[77] F. Schwabl. *Statistische Mechanik*. Springer, Berlin, 3rd edition (2006).

[78] L. P. Pitaevskij and S. Stringari. *Bose Einstein condensation*. Clarendon Press, Oxford, reprint edition (2004).

[79] J. D. Jackson. *Klassische Elektrodynamik*. de Gruyter, Berlin, 4th edition (2006).

[80] C. Eberlein, S. Giovanazzi, and D. H. J. O'Dell. "Exact solution of the Thomas-Fermi equation for a trapped Bose-Einstein condensate with dipole-dipole interactions". *Phys. Rev. A*, **71**, 033618 (2005). URL http://dx.doi.org/10.1103/PhysRevA.71.033618.

[81] A. Griesmaier, J. Stuhler, T. Koch, M. Fattori, T. Pfau, and S. Giovanazzi. "Comparing Contact and Dipolar Interactions in a Bose-Einstein Condensate". *Phys. Rev. Lett.*, **97**, 250402 (2006). URL http://dx.doi.org/10.1103/PhysRevLett.97.250402.

[82] A. Frisch, M. Mark, K. Aikawa, F. Ferlaino, J. L. Bohn, C. Makrides, A. Petrov, and S. Kotochigova. "Quantum chaos in ultracold collisions of gas-phase erbium atoms". *Nature*, **507**, 7493, 475–479 (2014). URL http://dx.doi.org/10.1038/nature13137.

[83] K. Baumann, N. Q. Burdick, M. Lu, and B. L. Lev. "Observation of low-field Fano-Feshbach resonances in ultracold gases of dysprosium". *Phys. Rev. A*, **89**, 020701 (2014). URL http://dx.doi.org/10.1103/PhysRevA.89.020701.

[84] N. Schopohl. "Private communications".

[85] J. J. Sakurai. *Modern quantum mechanics*. Prentice Hall, rev. edition (1994).

[86] F. Schwabl. *Quantenmechanik (QM I) : eine Einführung*. Springer, Berlin, 7th edition (2007).

[87] S. Chandrasekhar. *Ellipsoidal figures of equilibrium*. Yale Univ. Press, New Haven (1969).

[88] F. Dalfovo, C. Minniti, and L. Pitaevskii. "Frequency shift and mode coupling in the nonlinear dynamics of a Bose-condensed gas". *Phys. Rev. A*, **56**, 4855–4863 (1997). URL http://dx.doi.org/10.1103/PhysRevA.56.4855.

[89] R. van Bijnen, N. Parker, S. Kokkelmans, A. Martin, and D. O'Dell. "Collective excitation frequencies and stationary states of trapped dipolar Bose-Einstein condensates in the Thomas-Fermi regime". *Phys. Rev. A*, **82**, 033612 (2010). URL http://dx.doi.org/10.1103/PhysRevA.82.033612.

[90] D. Guéry-Odelin and S. Stringari. "Scissors Mode and Superfluidity of a Trapped Bose-Einstein Condensed Gas". *Phys. Rev. Lett.*, **83**, 4452–4455 (1999). URL http://dx.doi.org/10.1103/PhysRevLett.83.4452.

[91] O. M. Maragò, S. A. Hopkins, J. Arlt, E. Hodby, G. Hechenblaikner, and C. J. Foot. "Observation of the Scissors Mode and Evidence for Superfluidity of a Trapped Bose-Einstein Condensed Gas". *Phys. Rev. Lett.*, **84**, 2056–2059 (2000). URL http://dx.doi.org/10.1103/PhysRevLett.84.2056.

[92] M. Cozzini, S. Stringari, V. Bretin, P. Rosenbusch, and J. Dalibard. "Scissors mode of a rotating Bose-Einstein condensate". *Phys. Rev. A*, **67**, 021602 (2003). URL http://dx.doi.org/10.1103/PhysRevA.67.021602.

[93] J. Sanders and E. Kandrot. *CUDA by example : an introduction to general-purpose GPU programming*. Addison-Wesley, Upper Saddle River, NJ, 2nd edition (2010).

[94] W. H. Press, S. A. Teukolsky, W. T. Vetterling, and B. P. Flannery. *Numerical recipes in C++ : the art of scientific computing*. Cambridge Univ. Press., 2nd edition (2002).

[95] J. W. Cooley and J. W. Tukey. "An algorithm for the machine calculation of complex Fourier series". *Math. Comput.*, **19**, 90, 297–301 (1965). URL http://dx.doi.org/10.1090/S0025-5718-1965-0178586-1.

[96] M. L. Chiofalo, S. Succi, and M. P. Tosi. "Ground state of trapped interacting Bose-Einstein condensates by an explicit imaginary-time algorithm". *Phys. Rev. E*, **62**, 7438–7444 (2000). URL http://dx.doi.org/10.1103/PhysRevE.62.7438.

[97] Y. Qing-Xin and D. Guo-Hui. "Computing Ground State Solution of Bose–Einstein Condensates Trapped in One-Dimensional Harmonic Potential". *Commun. Theor. Phys.*, **46**, 5, 873 (2006). URL http://stacks.iop.org/0253-6102/46/i=5/a=021.

[98] W. Bao and Q. Du. "Computing the Ground State Solution of Bose-Einstein Condensates by a Normalized Gradient Flow". *SIAM J. Sci. Comput.*, **25**, 5, 1674–1697 (2004). URL http://dx.doi.org/10.1137/S1064827503422956.

[99] W. Bao, I.-L. Chern, and F. Y. Lim. "Efficient and spectrally accurate numerical methods for computing ground and first excited states in Bose-Einstein condensates". *J. Comput. Phys.*, **219**, 2, 836–854 (2006). URL http://www.sciencedirect.com/science/article/pii/S002199910600218X.

[100] W. Bao, Y. Cai, and H. Wang. "Efficient numerical methods for computing ground states and dynamics of dipolar Bose-Einstein condensates". *J. Comput. Phys.*, **229**, 20, 7874–7892 (2010). URL http://www.sciencedirect.com/science/article/pii/S0021999110003670.

[101] W. Bao and Y. Cai. "Mathematical theory and numerical methods for Bose-Einstein condensation". *KRM*, **6**, 1, 1–135 (2013). URL http://dx.doi.org/10.3934/krm.2013.6.1.

[102] G. Strang. "On the Construction and Comparison of Difference Schemes". *SIAM J. Numer. Anal.*, **5**, 3, 506–517 (1968). URL http://dx.doi.org/10.1137/0705041.

[103] T. E. Judd, R. G. Scott, and T. M. Fromhold. "Atom-chip diffraction of Bose-Einstein condensates: The role of interatomic interactions". *Phys. Rev. A*, **78**, 053623 (2008). URL http://dx.doi.org/10.1103/PhysRevA.78.053623.

[104] B. Jetter, J. Märkle, P. Schneeweiss, M. Gierling, S. Scheel, A. Günther, J. Fortágh, and T. Judd. "Scattering and absorption of ultracold atoms by nanotubes". *New J. Phys.*, **15**, 7, 073009 (2013). URL http://stacks.iop.org/1367-2630/15/i=7/a=073009.

[105] X. Antoine, W. Bao, and C. Besse. "Computational methods for the dynamics of the nonlinear Schrödinger/Gross–Pitaevskii equations". *Comput. Phys. Commun.*, **184**, 12, 2621 – 2633 (2013). URL http://dx.doi.org/10.1016/j.cpc.2013.07.012.

[106] J. Söding, D. Guéry-Odelin, P. Desbiolles, F. Chevy, H. Inamori, and J. Dalibard. "Three-body decay of a rubidium Bose–Einstein condensate". *Appl. Phys. B-Lasers O.*, **69**, 4, 257–261 (1999). URL http://dx.doi.org/10.1007/s003400050805.

[107] H. Ott, J. Fortágh, S. Kraft, A. Günther, D. Komma, and C. Zimmermann. "Nonlinear Dynamics of a Bose-Einstein Condensate in a Magnetic Waveguide". *Phys. Rev. Lett.*, **91**, 040402 (2003). URL http://dx.doi.org/10.1103/PhysRevLett.91.040402.

[108] H. Ott, J. Fortágh, and C. Zimmermann. "Dynamics of a Bose–Einstein condensate in an anharmonic trap". *J. Phys. B-At. Mol. Opt.*, **36**, 13, 2817 (2003). URL http://stacks.iop.org/0953-4075/36/i=13/a=311.

[109] Y. Wen-Mei, W. Xiu-Fang, Z. Xiao-Yan, and X. Ju-Kui. "Stability and Collective Excitation of Two-Dimensional BECs with Two- and Three-Body Interactions in an Anharmonic Trap". *Commun. Theor. Phys.*, **51**, 3, 433 (2009). URL http://stacks.iop.org/0253-6102/51/i=3/a=10.

[110] B. Carlson. "Computing elliptic integrals by duplication". *Numer. Math.*, **33**, 1, 1–16 (1979). URL http://dx.doi.org/10.1007/BF01396491.

Danksagung

An dieser Stelle möchte ich mich bei allen bedanken, die mich bei der Fertigstellung dieser Doktorarbeit unterstützt haben.

Ich möchte mich ganz herzlich bei Prof. Dr. Thomas Dahm für die ausgezeichnete Betreuung bedanken. Er hat mich auf dieses interessante Thema aufmerksam gemacht und somit das Erstellen dieser Arbeit überhaupt erst ermöglicht. Bei zahlreichen Gelegenheiten hat er sich Zeit genommen mit mir zu diskutieren und mir so immer wieder beim Lösen von Problemen geholfen. Zudem hat er mir immer die nötige Freiheit gelassen eigene Ideen zu verfolgen und auszuprobieren. Ganz besonders danke ich ihm auch dafür, dass er es mir ermöglicht hat ein halbes Jahr im Ausland zu verbringen.

Außerdem danke ich Prof. Dr. Nils Schopohl für die vielen interessanten und anregenden Diskussionen die ich während meiner Zeit in Tübingen mit ihm geführt habe. Vieles was ich von ihm gelernt habe hat auch zur erfolgreichen Fertigstellung meiner Arbeit beigetragen. Insbesondere danke ich ihm dafür, dass er mich auf die Möglichkeit der Verwendung der eindimensional Indexintegrale aufmerksam gemacht hat.

Bei Prof. Dr. Jürgen Schnack bedanke ich mich dafür, dass er sich dazu bereit erklärt hat meine Arbeit zu begutachten.

Ich möchte mich auch bei Prof. Dr. József Fortágh und seiner Arbeitsgruppe aus Tübingen, insbesondere bei Simon Bernon und Helge Hattermann, für die interessanten Diskussionen bedanken.

Bei meinen Zimmerkollegen Alexander Markowsky, Aida Mayer und Matthias Götte möchte ich mich für das angenehme Klima im Büro bedanken. Außerdem haben zahlreiche Diskussionen immer wieder bei der Lösung von kleineren und größeren Problemen geholfen.

Ich danke allen Mitgliedern des Department of Physics der University of Hull für die freundliche Aufnahme und für eine schöne Zeit während meines Aufenthaltes dort.

Zudem danke ich allen Mitgliedern der Arbeitsgruppen auf E5 für das angenehme Arbeitsklima und das stets freundliche miteinander.

Außerdem danke ich Hanne Litschewsky für ihre große Hilfsbereitschaft und ihr hohes Engagement.

Ich möchte mich bei all meinen Freunden bedanken, die mich während der Anfertigung meiner Arbeit moralisch unterstützt haben und abseits der Uni für die nötige Unterhaltung und Abwechslung gesorgt haben.

Besonders herzlich möchte ich mich bei Benjamin Jetter für das Korrekturlesen meiner Arbeit bedanken.

Schließlich danke ich noch meiner gesamten Familie: Meinem Bruder Zdravko, meiner Schwester Mari, meiner Schwägerin Petronela, meinem Schwager Johan, meiner Nichte Natalie und meinen Neffen Patrik, Tommy, Aron und Jonah. Insbesondere gilt meinen Eltern Janja und Ivo ein ganz herzliches Dankeschön. Durch ihre immerwährende Unterstützung habe sie diese Arbeit überhaupt erst möglich gemacht. Viele Dank!

Erklärung

Hiermit erkläre ich, dass ich die vorliegende Arbeit selbstständig und unter ausschließlicher Verwendung der angegebenen Quellen angefertigt habe.

Bielefeld, den 28. Januar 2015

Igor Sapina